universität wien

DISSERTATION | DOCTORAL THESIS

Titel | Title

Edge-barrier and film thickness effects on fast vortex dynamics in superconductors

verfasst von | submitted by

Dipl.-Ing. Barbora Budinská BSc

angestrebter akademischer Grad | in partial fulfilment of the requirements for the degree of

Doktorin der Naturwissenschaften (Dr.rer.nat.)

Wien | Vienna, 2024

Studienkennzahl lt. Studienblatt | Degree programme code as it appears on the student record sheet:	UA 796 605 411
Dissertationsgebiet lt. Studienblatt | Field of study as it appears on the student record sheet:	Physik
Betreut von | Supervisor:	Oleksandr Dobrovolskiy Privatdoz. PhD

Mamine a Tatinovi

Acknowledgements

This work would not have been possible without the support and help of many individuals. Here I would like to thank some of them.

I would like to express my gratitude to my supervisor Oleksandr Dobrovolskiy. I thank him for his support during my doctoral studies and for giving me a chance to work with him on many interesting projects. Especially I thank him for his countless helpful advice, tips, and tricks in how to navigate the, to me back then unknown, wonderful scientific world. I thank my big boss Andrii Chumak for welcoming me into his group, for his advice, and for creating the friendly environment in the workplace that I enjoyed so much. I would like to thank the long list of collaborators, D. Yu. Vodolazov, M. Yu. Mikhailov, F. Porratti, M. Huth, A. I. Bezuglyj, V. A. Shklovskij, and V. M. Bevz, experts in topics from fabrication, theory, simulation to measurements. I would like to thank Wolfgang Lang for his kind words during our mentoring meetings, for his prompt help when something did not seem right in the labs, and for helping me out with the organizational side of my work. As for all of my nanomag-nificient colleagues, I thank them all for not only their assistance, and sharing their knowledge with me but most of all for their friendship, and that I very much needed. Thank you for all the numerous hangouts, trips, parties, board game evenings, Glühwein stand visits, and many more. I know that I made lifelong friends. Thank you (and now I go alphabetically) Andrey, Andreas, Clemens, David, Fabian, Dr. Kris, Kris, Markus, Noura, Pedro, Rostyslav, Dr. Seb, Sebbro, Simon and Qi. A big special thanks goes to Bernd for his kindness, friendship, readiness to help and always finding a solution to my struggles in the lab, and answers to my questions.

Thank you Ajka. My rock. Thank you for listening to all my complaints and struggles, always being there for me, and always making sure I am happy.

I thank my entire family because only with their love and support I was able to stay strong and finish this for our dad. Ľubim vás veľmi, mamina, Kubko, Zuzka, Alesia, Jb.

And lastly I thank my love, Sabri because to him I owe the most. Thank you for helping me out in the labs when I needed it, many times in crazy hours, thank you for cheering me on in my work and supporting my decisions, thank you for the numerous times you dropped everything to take me out and take a needed break, but also thank you for the times you set me behind the computer when I was avoiding it. Thank you for your unconditional love and for taking care of me.

Abstract

The ability to manipulate the movement of individual vortices and to achieve ultrahigh vortex velocities is a subject of extensive investigations, triggered by the longing to use vortices in novel fluxonic devices where vortices would replace the role of electrons used in traditional nano- and microelectronics and by the longing to enhance superconducting single-photon detectors. In this regard, we employ a highly accessible method to study the vortex dynamics using current-voltage (I-V) curves measurements. Particularly the shape of the curves and the presence of an abrupt current-biased jump into a highly resistive state, the flux flow instability, serve as a method to extract information about the vortex dynamics, the maximal vortex velocity v^*, and the relaxation of quasiparticles (unpaired electrons) in a superconductor. Here, we investigated how the thickness of an amorphous MoSi film and a polycrystalline Nb film influences its superconducting parameters and compare the results with known models. We have observed that whilst most superconducting parameters worsen with decreasing thickness, v^* and the speed of relaxation improves. Therefore, films should be chosen to have middle range thicknesses depending on the intended use and material. The study has also shown that the currently employed models to derive the relaxation time τ_ϵ only poorly describe real experimental data in thin films. We ascribe this to the neglect of local flux-flow instability and edge barrier effects in these models. To justify this, in the second part of this thesis, we investigate 15-nm thick MoSi films with rough and smooth edges produced by laser etching and milling by a focused ion beam. The dependency of the relaxation time on the edge is an indicator that the relaxation time derived using the currently employed models is not an intrinsic property as would be desired. The films with smooth edges lead to between 10 to 20 times larger v^*, a factor of 3 larger critical currents, and a factor of couple tenths shorter relaxation times. In addition, we observed an improvement in the fits of the models for the films with smooth edges for which edge barrier effects should be less prominent. In the very last section of this thesis, artificially created slits in the edges of 15-nm thick MoSi films were studied. Firstly, the unique vortex dynamics of such structures are described by studying transverse voltage both analytically and experimentally. Secondly, kinks in I-V curves are used to determine the number of fluxons crossing the slitted structures in order to precisely determine v^* at low magnetic fields. Our findings in the scope of this thesis are essential to improve how superconducting material parameters are derived from I-V measurements in thin films.

Zusammenfassung

Die Fähigkeit, die Bewegung einzelner supraleitender Wirbel zu manipulieren und ultrahoch Wirbelgeschwindigkeiten zu erreichen, ist Gegenstand umfangreicher Untersuchungen, um solch supraleitende Wirbel in neuartigen fluxonischen Bauelementen zu verwenden, in denen Wirbel die Rolle von Elektronen in der herkömmlichen Nano- und Mikroelektronik ersetzen und um supraleitende Einzelphotonendetektoren zu verbessern. In diesem Zusammenhang setzen wir eine leicht zugängliche Methode zur Untersuchung der Wirbeldynamik ein, indem wir Stromspannungskurven (I-V) messen. Insbesondere die Form der Kurven und das Vorhandensein eines abrupten stromabhängigen Sprungs in einen hochohmigen Zustand, die Flussstrominstabilität, dienen als Methode, um Informationen über die Wirbeldynamik, die maximale Wirbelgeschwindigkeit v^* und die Relaxation von Quasiteilchen (ungepaarte Elektronen) in einem Supraleiter zu gewinnen. In dieser Arbeit haben wir untersucht, wie die Dicke eines amorphen MoSi-Films und eines polykristallinen Nb-Films die supraleitenden Parameter beeinflusst und die Ergebnisse mit bekannten Modellen verglichen. Wir haben festgestellt, dass sich die meisten supraleitenden Parameter mit abnehmender Dicke verschlechtern, während sich v^* und die Relaxationsgeschwindigkeit verbessern. Daher sollten je nach Verwendungszweck und Material Schichtdicken im mittleren Bereich gewählt werden. Die Studie hat auch gezeigt, dass die derzeit verwendeten Modelle zur Ableitung der Relaxationszeit τ_ϵ reale experimentelle Daten in dünnen Filmen nur unzureichend beschreiben. Wir führen dies auf die Vernachlässigung lokaler Flussstrominstabilitäten und Randbarriereeffekte in diesen Modellen zurück. Um dies zu rechtfertigen, untersuchen wir im zweiten Teil dieser Arbeit 15-nm dicke MoSi-Schichten mit rauen und glatten Kanten, die durch Laserätzen und Fräsen mit einem fokussierten Ionenstrahl hergestellt wurden. Die Abhängigkeit der Relaxationszeit von der Beschaffenheit der Kante ist ein Indikator dafür, dass die mit den derzeit verwendeten Modellen abgeleitete Relaxationszeit keine intrinsische Eigenschaft ist, wie es wünschenswert wäre. Die Filme mit glatten Kanten führen zu 10 bis 20 Mal größeren v^*, um den Faktor 3 größeren kritischen Strömen und um den Faktor von einigen Zehnteln kürzeren Relaxationszeiten. Außerdem beobachteten wir eine Verbesserung der Anpassungen der Modelle für die Filme mit glatten Kanten, für die Kantenbarriereeffekte weniger ausgeprägt sein sollten. Im allerletzten Abschnitt dieser Arbeit wurden künstlich erzeugte Schlitze an den Kanten von 15 nm dicken MoSi-Filmen untersucht. Zum einen wird dabei die besondere Wirbeldynamik solcher Strukturen beschrieben, indem die Transversalspannung sowohl analytisch als auch experimentell untersucht wird. Zum anderen werden die Knick-

stellen in den I-V-Kurven zur Bestimmung der Anzahl der Fluxonen, welche die geschlitzten Strukturen durchqueren, verwendet, um v^* bei niedrigen Magnetfeldern genau zu bestimmen. Unsere Erkenntnisse im Rahmen dieser Arbeit sind wichtig, um die Ableitung von Parametern supraleitender Materialien aus I-V- Messungen in dünnen Schichten zu verbessern.

Contents

List of Tables

List of Figures

Chapter 1

Introduction

Since the year 1911, when Kamerlingh Onnes discovered the unexpected behavior of close to zero electrical resistivity whilst performing measurements on mercury [1], which is now known to be one of the signature characteristics of superconductors, superconductors can be seen used in a broad range of applications in various fields. The ability of superconductors to transfer current with virtually no losses makes them a great material for coil assembly to be used in very effective electromagnets [2, 3], while the ability of superconductors to expel magnetic field from their interior is essential, for example, for the working principle of levitating trains [4]. The quantum condition between an applied electromagnetic wave frequency and an electric voltage through a Josephson junction [5] (a thin, electrically insulating barrier between two superconducting electrodes) provides the perfect tool for the preparation of accurate and stable voltage standards [6, 7]. Furthermore, the superconducting magnetic flux quantization [8, 9] along with the Josephson effect are utilized for the fabrication of very precise magnetometers, SQUIDs (abbreviated from Superconducting Quantum Interference Device) [10], and the sharp transition from low to high voltage when moving from the superconducting state to a higher conducting state is the underlying principle utilized in superconducting single-photon detectors (SSPDs) [11].

In this work, we will be exploring yet another important characteristic of a specific group of superconductors, namely the Shubnikov state present in the so-called type II superconductors [12]. The indicator of the Shubnikov phase is the appearance of spatially confined magnetic flux quanta surrounded by superconducting circular currents in the presence of a magnetic field, Abrikosov vortices [13]. In the 1960s, experiments supported by theory introduced the concepts of the "flux flow" [14, 15], the movement of Abrikosov vortices through the superconductor under the action of the current-driven Lorentz force. Contrary to the efforts of many to pin vortices in order to preserve the nondissipative state in higher transport currents, in recent years, as well as in this work, the study of guided movement of vortices and of achieving high vortex velocities is of interest. Although moving vortices are responsible for energy dissipation, and at high velocities they are the activators of the flux-flow instability (FFI) [16], an abrupt jump into the normal conducting state, their movement also unleashes

new interesting applications and phenomena. The ability to manipulate the movement of individual vortices similar to electrons in nano- and microelectronics can be utilized to design fluxonic devices [17–20]. In order to develop these new fluxonic devices one must first learn a lot about the properties and dynamics of these objects.

A considerable part of this work is devoted to the study of the vortex dynamics via current-voltage (I-V) curve measurements accompanied by time-dependent Ginzburg-Landau (TDGL) simulations. Many techniques, like the scanning tunneling microscopy (STM) [21], the magnetic force microscopy (MFM) [22] or the magneto-optical imaging [23], to name a few, make it possible to directly visualize static or slowly moving superconducting vortices, yet these techniques are deficient when trying to observe high-speed vortices. Despite recent striking advances in the development of a technique that allows one to directly observe the properties of fast-moving vortices, nanoscale SQUID-on-tip (nanoSOT) microscopy [24], its availability to the majority of researchers is limited. However, a technique broadly available is the technique of measuring I-V curves. In these curves, simply explained, a voltage increase is directly linked to the movement of a vortex through the superconductor. A more detailed description of an I-V curve and its meaning is given in the theory part of this thesis in Section 2.2.3. In addition, the presence of an FFI in the I-V curve presents a way to calculate the highest achievable vortex velocity v^* and the quasiparticle energy relaxation time τ_ϵ, both of which are of great interest.

Vortices moving with v^* higher than a certain threshold velocity v^{th} of possible excitations in a given system can trigger Cherenkov-like responses. Previously explored were the generation of sound [25, 26], and in superconductor/ferromagnet heterostructures generation of spin waves [27, 28] by fast moving vortices. It is therefore necessary to search for materials and ways to achieve high enough vortex velocities, on the order of a few km/s.

The second referred to derivable parameter, τ_ϵ, plays an essential role in the field of superconducting detectors. The relaxation processes, of which electron-phonon scattering and phonon escape are the most relevant, described by τ_ϵ are directly related to the performance of these detectors. The reset time, the time the detector needs to detect another signal, for SSPDs [29, 30], as well as hot-electron bolometers (HEB) [31, 32] is strongly dependent on τ_ϵ. A good candidate for a superconducting detector has therefore a very short τ_ϵ.

The key finding of this work is the experimental observation and discussion of the effects of sample thickness and sample edge quality on vortex dynamics. Samples of amorphous molybdenum silicon (MoSi) and polycrystalline niobium (Nb) were prepared in different thicknesses. As a result of experiments on the listed samples, we were able to put together tables summarizing their superconducting parameters, which are influenced by their preparation method, crystallization, and geometry. From the study performed on this data, we observed that the currently often utilized FFI models cannot replicate what is seen in the experiments on thin films. We theorize what might be the reason for this by referring to the edge-controlled FFI model [33] developed by Vodolazov. In this model, the author theoretically describes the local current density maxima near the edge of a superconducting strip. This region allows

for vortex entry due to local suppression of superconductivity and lowering of the entrance barrier. It is this local suppression of superconductivity that leads to a local FFI. In previous models, FFI was always considered as a global phenomenon. We assume that in thin films the local FFI plays a crucial role. Hence, we cannot fit the experimental data of thin films with non-local global models. To put this to the test, we fabricated an environment, where we suppose the local FFI to be suppressed, which should result in better fits of non-local models. For this purpose, two MoSi samples with two different edge qualities were fabricated. One sample was laser cut, creating a rather rough edge, while the edges of the second sample were smooth because of preparation with focused ion beam (FIB) milling. A difference in the onset of the FFI proved that the sample with the rough edge had a local domain with high density and high temperature that locally triggered the FFI. We also observed an improvement in fitting the non-local models to the data of the sample with the smooth edge.

In the very last part of the thesis two additional phenomena are discussed that followed from the carried out work on vortex dynamics. First is the analytical and experimental work on transverse voltages in slitted superconductors, and second is a method to count vortices at zero magnetic fields. At higher magnetic fields, one can estimate the number of vortices simply by comparing the intervortex distance a as defined by Abrikosov [13] and the sample geometry. It is important to mention that the intervortex distance, if calculated from the external magnetic field, omits the fact that vortices are also being created through the self-field generated by the transport current. At higher magnetic fields these estimates are sufficient, but at low and zero magnetic fields, where the number of vortices that are created by the self-field is in the same order of magnitude as the number of vortices created by the external field, one needs to look for additional methods to calculate the number of vortices. The experiments on slitted superconductors were inspired by the theoretical work of Aslamazov and Larkin [34] on kinks in I-V curves of superconducting bridges. Here, they explained how these steps appear everytime the number of vortices in the sample is increased by one. We observed such kinks in slitted superconductors. This allows one to count the vortices present in the sample in low magnetic fields during the FFI event and improve the way one calculates the maximal vortex velocity v^*.

The thesis is concluded with a summary of the obtained results and statements, and with an outlook to the future of vortex dynamics.

Chapter 2

Theoretical background

Despite superconductivity being first observed by Onnes in 1911 [35], it took nearly 50 years to develop the first microscopic theory. Proposed by Bardeen, Cooper and Schrieffer, today the theory is known after its founders as the BCS theory [36]. The BCS theory extends the calculation of the Cooper problem. The Cooper problem solves the Schrödinger equation for two electrons just outside the Fermi level in the presence of an attractive pairing potential between these two electrons. As a result, the calculation shows that the attractive potential is responsible for creating a bound state, the superconducting state, with an energy below the energy $2E_F$, which is the energy of the original ground state of two unpaired electrons. This makes the pairing energetically favorable. The two paired electrons are collectively called a Cooper pair, and the unexpected attractive force between two electrons is understood to be mediated via phonon interactions. Only electrons near the Fermi surface and with opposite spin create Cooper pairs. The total spin of the pair is therefore zero, and the pair behaves boson-like. Many pairs occupy the same quantum state, which is then described by a single macroscopic wave function $\psi = |\psi|e^{i\phi}$, with amplitude $|\psi|$ and phase ϕ. The superconducting state is thus protected against a collapse into the normal state by the existence of a couple meV wide gap around the Fermi level, where there are no states that can be occupied by electrons. It is also this gap and the macroscopic coherence between a large number of electrons that prevents low-energy excitations and scattering, which otherwise lead to energy dissipation and non-zero electrical resistivity. For that reason, superconductors are ideal conductors. The gap is greatest at temperature $T = 0$ and with increasing temperature decreases because the binding energy weakens with temperature, until a critical temperature T_C is reached, where the gap vanishes completely and superconductivity disappears. The energy gap at $T = 0$ can be approximated using the following:

$$\Delta(0) \approx 1.76 k_B T_C, \tag{2.1}$$

where k_B is the Boltzmann constant.

The existence of a superconducting state is further limited by the magnetic field strength. The way a superconductor behaves in a certain magnetic field categorizes it into the group of type I or type II superconductors.

2.1 Type I and II superconductors

A type I superconductor is characterized and limited by a critical magnetic field $H_C(T)$. While the values of an external magnetic field are lower than $H_C(T)$, the external magnetic field H_{out} is being fully expelled from the interior of this type of superconductor. This effect was discovered in 1933 and received the name Meissner-Ochsenfeld (MO) effect [37]. The MO effect uniquely characterizes the superconducting state. Uniquely, because solely the property of superconductors being ideal conductors does not explain the expulsion of the field. In fact, ideal conductors actually trap magnetic flux inside. The presence of the Meissner state has also the consequence that the superconducting state is a thermodynamic equilibrium state. In a H-T diagram, the resulting state is the same as the state for the same set of H-T parameters independent of the path along which this point was reached.

The field expulsion is mediated via the occurrence of circulating shielding currents that flow on the surface. These shielding currents generate a magnetic field, similar to that in an electric coil, that is directed opposite to the external magnetic field. Considering that the internal field $H_{int} = 0 = H_{out} + M$, the magnetization is equal to the negative of the applied field, which means that superconductors behave as perfect diamagnets with magnetic susceptibility $\chi = -1$.

The shielding currents flow only within a specific depth, the London penetration depth λ_L, from the surface. It was the London brothers in 1935 that took this depth of shielding currents into account in their phenomenological model, and they were the first to explain the MO effect [38]. Their calculations, based on the Drude model for electrical conductivity of which the scattering term for superconducting electrons was omitted, led to the establishment of two London equations. The London equations explain the shielding of time-varying as well as static magnetic fields. The magnetic field has an exponential decrease from the surface of the superconductor given by: $H(x) = H(0)e^{(-x/\lambda_L)}$, with x being the depth coordinate ($x = 0$ corresponds to the surface). In conclusion, the London brothers explained the existence of the MO effect, but also showed that the magnetic field penetrates a small distance into the superconductor in spite of the MO effect.

Once the external magnetic field is equal to $H_C(T)$ a phase transition, from the superconducting state to a normal conducting state, takes place. At $H_C(T)$ the energy advantage of the superconducting state given by the condensation energy G_C, is lost due to the need for high energy to build up shielding currents, the magnetization energy G_M. $H_C(T)$ is well approximated by a parabolic law, $H_C(T) \approx H_C(0)(1 - (T/T_C)^2)$. Figure 2.1 (a) depicts the phase diagram of a type I superconductor.

In contrast, type II superconductors are described by two such critical fields, a lower critical field $H_{C1}(T)$ and an upper critical field $H_{C2}(T)$. Bellow $H_{C1}(T)$ the type II superconductor experiences a full expulsion of the magnetic field and is in the Meissner state. However, cross-over of the $H_{C1}(T)$ causes magnetic flux quanta to penetrate into the interior of the superconductor. This phase between the two critical fields is called the Shubnikov

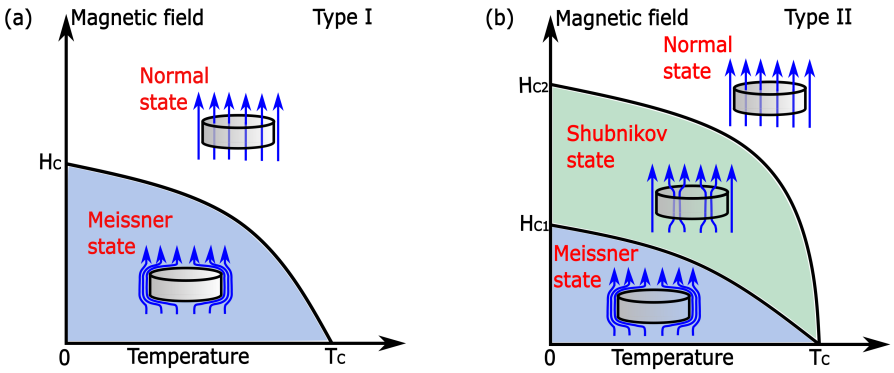

Figure 2.1: Magnetic phase diagrams of type I (a) and type II (b) superconductors portraying the Meissner, Shubnikov and normal phase. Inside each phase an insert of a superconductor in this phase is depicted. Blue arrows represent the magnetic field lines.

phase [12]. The magnetic flux quanta, further referred to as vortices, carry a quantized flux:

$$\Phi_0 = h/(2e) = 2.07 \times 10^{-15}\ \mathrm{Tm}^2, \tag{2.2}$$

and are surrounded by supercurrent shells, keeping the rest of the material superconducting. They are arranged in a triangular-shaped lattice with lattice spacing $a \simeq 1.07\sqrt{\frac{\Phi_0}{B}}$. This lattice is widely known as the Abrikosov lattice [13], named after Aleksei Abrikosov, who described how these vortices can penetrate type II superconductors. Only once the external magnetic field increases above $H_{C2}(T)$ a transition to a normal conducting state takes place. Figure 2.1 (b) shows the phase diagram of a type II superconductor.

If it is energetically favorable for a material to let in vortices, and hence be a type II superconductor, is given by the characteristic value of the Ginzburg-Landau parameter κ. Owing to the fact that the Rutgers formula for phase transitions of the second order describes the discontinuity in the specific heat of superconductors at $T = T_C$, in the year 1950 Ginzburg and Landau (GL) developed a theoretical model based on the Landau theory for phase transitions of the second order [39]. In this theory, the free energy is written as a series expansion of functions of even power of an order parameter. The chosen order parameter must be non-zero under the critical temperature and zero above the critical temperature. Ginzburg and Landau therefore chose the absolute value of the superconducting wave function, $|\psi|$, to be the order parameter in their new theory. The absolute value of the superconducting wave function squared is equal to n_s, the density of the superconducting particles. This parameter originates from the two-fluid model where with $n_s = 1$ one describes a state where all particles are superconducting, whilst the density of normal conducting particles is given as $n_n = 1 - n_s$. Minimizing the free energy in the GL-theory at zero external field gives rise to the proportionality expression $\psi \propto e^{\pm i\frac{x}{\xi_0}}$, where ξ_0 is the GL-coherence length. Therefore, the GL-coherence length describes the decrease of n_s approaching the surface. Both of the mentioned characteristic superconducting parameters λ_L and ξ_0 are depicted in figure 2.2 (a,b) at a vacuum/superconductor boundary. We compare ξ_0 with the mean electron free

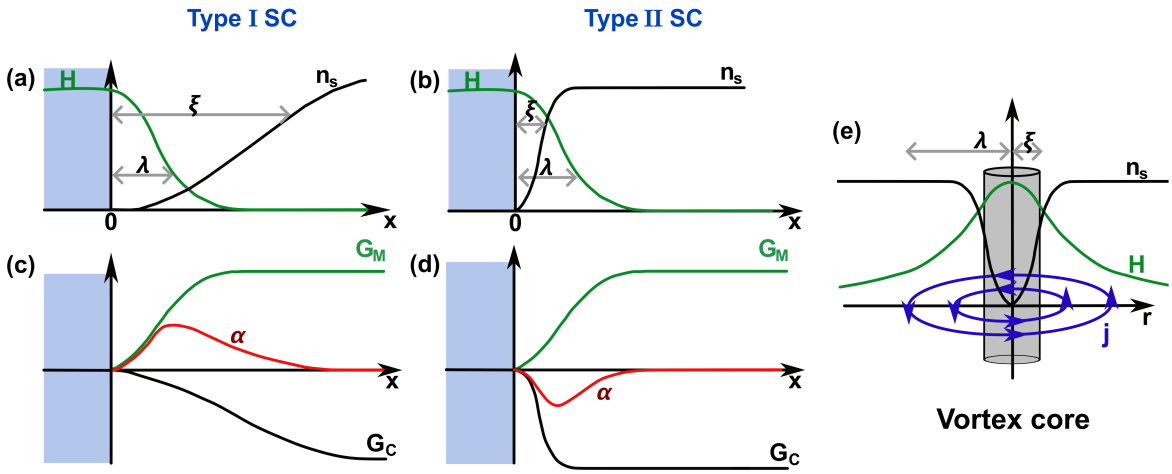

Figure 2.2: Characteristic superconducting parameters λ_L and ξ_0 for a type I (a) and type II (b) superconductor on the barrier between vacuum (light blue) and the superconductor (x>0). Further depicted is the wall energy α for type I (c) and type II (d) as the sum of the positive magnetization energy G_M and the negative condensation energy G_C. In (e) are the characteristic parameters shown for a vortex. The gray area corresponds to the vortex core and the blue arrows are the circulating currents.

path l to differentiate between dirty and clean superconductors. If $\xi_0 < l$ the superconductor is in the clean limit, if $\xi_0 > l$ it is in the dirty limit.

The GL-theory further introduces the domain-wall energy α needed to create an interface that separates the normal and superconducting regions. A positive domain-wall energy describes a stable equilibrium of volumes of two phases and describes type I superconductors. It was only Abrikosov that first suggested the possibility of a negative domain-wall energy to explain type II superconductors [13]. In this case, it is energetically favorable for the superconductor to increase the number of interfaces by letting vortices in. This domain wall energy is determined as the sum of the positive magnetization energy G_M and the negative condensation energy G_C. The magnetization energy for $H_{int}(x) = 0$ is $\frac{\mu_0 H_C^2}{2}$ and falls to zero with a raising field toward the surface. The condensation energy for $n_s(x) = 1$ is given as $-\frac{\mu_0 H_C^2}{2}$ and approaches zero with a decrease in n_s. This gives the condensation energy a dependence on ξ_0 and the magnetization energy a dependence on λ_L. As can be observed from the example in figure 2.2 (c,d), careful calculation is required to calculate the crossover point from negative to positive domain-wall energy. This crossover was found to occur at $\kappa = \lambda_L/\xi_0 = 1/\sqrt{2}$. With κ smaller than $1/\sqrt{2}$ we recognize type I superconductors and with larger than $1/\sqrt{2}$ type II superconductors.

The characteristic superconducting parameters λ_L and ξ_0 also play a role in the description of a single vortex as seen in figure 2.2 (e). The GL order parameter is zero on the vortex axis and is suppressed around the axis with the radius r of the order of ξ_0. This means that at the core of the vortex there are normal conducting electrons. The magnetic field of a vortex

core has a logarithmic decrease $ln(\lambda/r)$ when the distance r from its axis is between ξ_0 and λ_L, and an exponential decrease $e^{(-r/\lambda)}$ in large distances from the cores' center.

ξ_0 and λ_L can be calculated using:

$$\xi_0 \approx \sqrt{\frac{\hbar D}{\Delta(0)}} \tag{2.3}$$

and

$$\lambda_L\,[m] \approx 1.05\,10^{-3}\sqrt{\frac{\rho\,[\Omega m]}{T_C\,[K]}}, \tag{2.4}$$

where D is the diffusion constant and ρ is the normal resistivity. The diffusion coefficient can be calculated from [40]:

$$D = -\frac{1.097}{dB_{C2}/dT}. \tag{2.5}$$

One shall not forget that the validity of the GL-theory is limited to close to T_C temperatures.

2.2 Vortex dynamics

In this, as well as all the following chapters, we will be dealing with type II superconductors. Type II superconductors make up the majority technically relevant superconductors. Previously we have already mentioned two critical parameters that limit superconductivity, the critical temperature T_C and the critical field $H_C(T)$. Since superconductors major attractiveness for industry comes from the never ending flow of current due to the zero resistivity, it is important to look at the superconductivity limit caused by current flowing through a superconducting sample. The Silsbee hypothesis explains how the flowing current produces a magnetic field that in addition to the external magnetic field, can exceed the critical field $H_C(T)$ and break the superconducting state. The current density at which it comes to this breakage is called the depairing current density $J_{dep}(T, B)$. However, in type II superconductors we recognize a raise in resistivity at current densities well before $J_{dep}(T, B)$ is reached. This was recognized by Anderson to be a consequence of the vortices moving around in the sample and dissipating energy [41]. Scientists therefore invest a lot of energy into new ways how to pin vortices down and limit their movement, hence pushing the zero resistivity state into higher and higher current densities. In this thesis, on the other hand, we are interested in enabling the movement of vortices and study their velocity, motion patterns and trajectory manipulation. The study of vortex dynamics is crucial to understanding how vortices can be used in future fluxon devices. The major interactions contributing to the complex dynamics of vortices are the vortex-current interaction, vortex-defect attraction, vortex-vortex repulsion, and vortex-surface interaction.

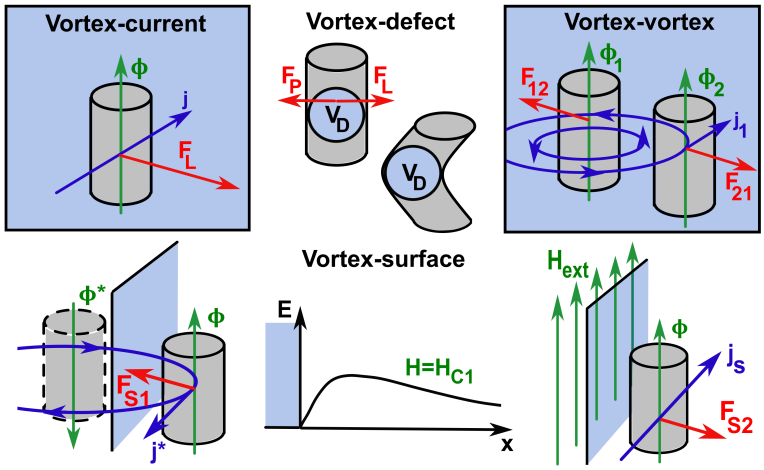

Figure 2.3: A schematic sketch of possible vortex interactions.

2.2.1 Vortex interactions

The schematic sketch in figure 2.3 is a visual guide for all interactions to follow.

Vortex-current interaction

An electric current of density j passing through a type II superconductor causes the raise of a Lorentz-like force [42] (for simplicity further refered to as just the Lorentz force) that acts on each individual vortex and moves them in a direction that is perpendicular to the quantized magnetic field of the vortex flux lines and the applied electric current. The Lorentz force on a single vortex is expressed as $\boldsymbol{F_L} = \boldsymbol{j} \times \boldsymbol{\Phi_0}$. The movement of vortices in turn generates an electric field $\boldsymbol{E} = -\boldsymbol{v} \times \boldsymbol{B}$, where v is the average velocity of all vortices and B is the magnetic induction in the sample (which is approximately the same as the external magnetic field). The electric field E and the applied electric current I are parallel, which leads to electric losses. This means that the flowing current will experience losses and will not flow infinitely long. The movement of vortices in steady motion is termed flux flow, and the resulting resistivity due to this motion is called flux flow resistivity ρ_f. If no pinning is available, the Lorentz force is only opposed by friction of the medium, $\boldsymbol{j} \times \boldsymbol{\Phi_0} = \eta \boldsymbol{v}$, where η is the viscous drag coefficient. The flux flow resistivity is then

$$\rho_f = \frac{E}{J} = \frac{B\Phi_0}{\eta}. \tag{2.6}$$

Bardeen and Stephen (BS) used a rather simplified model to calculate the viscous drag coefficient from the dissipation of energy of the moving vortex core [43]. In their model, they considered a fully normal conducting vortex core abruptly switching to fully superconducting state at radius $a = \xi_0$. Substituting their result for η in the equation 2.6 for flux flow resistivity, one obtains the BS flux flow resistivity

$$\rho_{BS} = \rho_n \frac{B}{H_{C2}}, \tag{2.7}$$

where ρ_n is the resistivity of the normal conducting state. The viscous damping accounts for an Ohmic conductivity, which means that the voltage increases linearly with current.

Vortex-defect interaction

The energy ϵ needed for a vortex to form inside a superconductor has two contributions. The self-energy of a flux line per unit of length ϵ_1 and the interaction energy ϵ_{12}. In the scenario where an entire flux line, including circulating currents, lies within a normal conducting area (nl-area), the entire energy ϵ multiplied by the volume of the flux line lying inside the nl-area V_D is spared. The energy saved is $\Delta E = \epsilon V_D$. This makes the normal conducting spot a preferred site for the flux line compared to the superconducting matrix. The force with which the line is held at this spot is called the pinning force F_P and it is proportional to $\Delta E/\lambda_L$.

Now we consider a different scenario, where the nl-area is smaller and only the flux line core fits inside but the circulating currents do not. In this case, it is the condensation energy G_C that is spared. The saved energy is $\Delta E = G_C V_D$ and F_P is proportional to $\Delta E/\xi_0$.

Not only nl-areas, but also areas with local decrease in superconducting parameters act as preferred pinning sites. Defects like impurities, holes, grain boundaries, thickness variations, and other spatial inhomogeneities can cause these local variations, many of which can be created purposefully and in a controlled manner. The pinning force is an opposing force to the Lorentz force and can guide vortices in a chosen direction or anchor vortices to avoid energy dissipation. The depinning current density J_C^* is now described as the maximum current density allowed before the vortices start to move and the resistivity starts to increase from zero, $\boldsymbol{F_P} = \boldsymbol{F_L} = \boldsymbol{J_C^*} \times \boldsymbol{B}$ [44]. If the pinning force is strong enough, it can preserve the perfect conductor properties even at high driving currents. However, thermally activated hopping from one pinning site to another can occur. This effect is called the flux creep. It should also be mentioned that the elasticity of the flux line comes into play when pinning to point defects, for instance. This makes the study of pinning mechanisms an extremely difficult field.

Vortex-vortex interaction

The interaction energy ϵ_{12} between vortex 1 at position r_1 and vortex 2 at position r_2 results from the field of vortex 1 being present at the position of vortex 2 and vice versa. The interaction is repulsive, similar to two wires with current running through them in the same direction. The acting interaction force F_{12} on vortex 1 can be calculated as the spatial derivation of the interaction energy. We obtain $\boldsymbol{F_{12}} = \boldsymbol{J_2(r_1)} \times \boldsymbol{\Phi_0}$, where J_2 is the supercurrent density due to vortex 2s' field at position of vortex 1. In an array of vortices, the repulsive forces between them are the reason for the formation of the triangular Abrikosov lattice [13], as this leads to the greatest separation between neighbors. The vortex mutual repulsion causes them to move in bundles once the Lorentz force exceeds the pinning force in a certain volume. In the case of a vortex and antivortex that have opposite directions of field, this force is attractive.

Vortex-surface interaction

The forces that act on a vortex trying to enter or exit a superconductor have two different natures [45]. The first force can be understood on the basis of the concept of an imaginary antivortex. At the surface, the supercurrent perpendicular to the surface must be zero to ensure continuity. This can be ensured by mirroring a vortex at the surface into an antivortex with Φ^* right outside the surface. As mentioned above, the vortex and antivortex attract each other, making the first part of the vortex-surface force F_{S1} attractive. The second force is due to the penetration of the external field H_{ext} into the surface at the edges. The field is shielded by a superconducting circulating current j_s. This results in a repulsive vortex-surface force F_{S2}. The joint forces create an energy edge barrier for flux motion in both directions, in and out of the superconductor, at the surface boarder. For $x \gg \lambda$ and high external fields the repulsive force dominates, whilst at $H = 0$ only the attractive force takes action. The barrier has as a consequence that vortices may not enter the interior at the GL calculated H_{C1}, but only at a certain higher field H_S, once the attractive force is dominated by the repulsive one. Exiting from the superconductor, when an external field is being lowered, on the other hand, is only possible at zero external magnetic fields. The delayed escape can be observed as a hysteresis in magnetization measurements.

Note that surface defects can locally exceed the H_S, lowering the edge barrier, and hence act as points of preferred entry for the vortices.

2.2.2 Langevin equation

Using a single vortex approximation, one can describe certain essential physical phenomena resulting from moving vortices very well. Calculations based on the Langevin equation offer a rather simple technique but can address various dynamic states. We consider the vortex being subjected to all the forces we introduced in the previous section and a fluctuating ("random") force in the form of a white noise thermal force F_{th}. These forces are opposed by the already mentioned friction and a Magnus force. The Magnus force takes effect because of the circulating currents around a vortex moving through the medium. The Magnus force causes a transverse motion, giving rise to Hall conductivity. The final Langevin equation for a single vortex is then given as:

$$\eta_0 \boldsymbol{v} + \alpha \boldsymbol{\Phi_0} \times \boldsymbol{v} = \boldsymbol{F_L} + \boldsymbol{F_P} + \boldsymbol{F_{12}} + \boldsymbol{F_{th}}, \tag{2.8}$$

where α is the Hall coefficient. This equation allows for instance to observe effects in nano-engineered pinning sites or slits.

2.2.3 Current-voltage curves

A convenient method to make observations and conclusions about the dynamics in experiment is the measurement of current-voltage curves. In the section on vortex-current interactions we learned that moving vortices cause an increase in the electric field. This can be observed

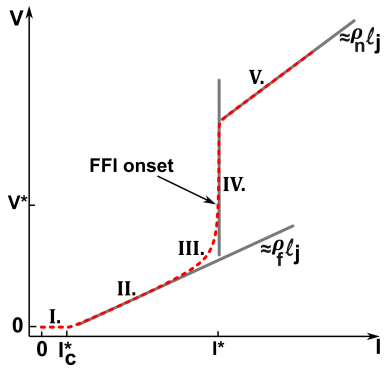

Figure 2.4: A typical current-voltage curve for a type II dirty superconductor. The regions are: I.) the pinned vortex state, II.) the linear flux flow regime, III.) the nonlinear flux flow regime, IV.) the FFI and V.) the normal conducting state.

as an increase in voltage since $V = -El$, where l is the distance between voltage contacts. Figure 2.4 depicts a typical current-voltage curve of a dirty type II superconductor. We recognize the following sections: I.) the pinned vortex state ending at J_C^*, II.) the linear flux flow regime with $V \approx \rho_f l j$, III.) the nonlinear flux flow regime, IV.) the flux-flow instability at coordinates I^*-V^*, and V.) the normal conducting state with $V \approx \rho_n l j$.

The linear regime is an quasi-equilibrium state, but moving vortices initiate non-equilibrium phenomena connected to various relaxation processes. These phenomena become stronger and visible in regions III.) and IV.) The next chapter is dedicated to these non-equilibrium mechanisms that are at the core of the study of this thesis. Regions III.) and IV.) are also addressed in more detail.

To calculate the vortex velocity from the measured voltage, we transform the equation for generated electric field $E = -v \times B = -V/l$. The velocity can thus be calculated with

$$v = V/Bl. \tag{2.9}$$

Here we assume that the induced magnetic field B in the sample is the same as the external applied magnetic field.

2.3 Non-equilibrium phenomena

As non-equilibrium phenomena we understand phenomena as a result of processes that have a certain time dependence that cannot be omitted. All of these processes have their own relaxation times. Introducing time dependence into the GL theory gives rise to the time-dependent Ginzburg-Landau theory (TDGL), which can model some nonstationary processes in superconductors.

2.3.1 Time-dependent Ginzburg Landau equations

Using the TDGL model one can establish relationships for the time derivative of the GL order parameter at a certain location, essentially mapping the movement of a vortex. It further explains how the dissipation function has two contributions. First is the dissipation caused by relaxation of the order parameter with relaxation time $\tau_{\triangle}$. As Tinkham explains, due to the movement of the vortex, the order parameter at a certain location varies in time. This introduces a relaxation of the order parameter that gives raise to dissipation [46]. The second contribution explained by Bardeen and Stephen is due to the presence of a normal conducting current in the vortex core [43]. This process is characterised by the relaxation time τ_j. Both of these mechanisms give contributions to the newly defined effective flux flow resistivity. This flux flow resistivity is proportional to the BS flux flow resistivity from expression 2.7. At low magnetic fields the known expression is complemented by u, the ratio between $\tau_{\triangle}$ and τ_j, and by a, a function covering the contributions of dissipation from the two mentioned processes. At high fields the additional term of β_A, the Abrikosov parameter determined by the structure of the lattice, is added. Once again the response has an Ohmic character and regions III.) and IV.) from figure 2.4 can not be described. This lays in the limitations of the TDGL theory. The TDGL theory is similarly to the GL theory only valid at close to T_C temperatures. A further necessary restriction is that one can only use the TDGL model for essentially gapless superconductors with small and slow deviations of the order parameter from the equilibrium state [47]. A generalized TDGL was written that made the theory applicable to dirty gapped superconductors but only when their inelastic electron-phonon diffusion length is smaller then ξ_0 [48], thus the deviations of the order parameter must happen slower than the electron-phonon scattering time τ_{ep}. The TDGL and generelized TDGL work only in a so-called local equilibrium approximation. This means the quasiparticles must essentially be in equilibrium with the heat bath. Vodolazov coupled the TDGL to the heat conductance equation, which allowed him to observe faster changes of the order parameter than τ_{ep} [33], but this method is limited by requiring the electron-electron scattering time τ_{ee} to be smaller than τ_{ep}. Numerical modeling using these models allow for discovery and visualization of previously hidden physical phenomena. Namely the spatial change of the Abrikosov lattice, and the appearances of vortex rivers and phase slips [49, 50]. This happens due to the finite $\tau_{\triangle}$. A moving vortex leaves behind a wake of suppressed superconductivity that attracts the vortices behind it to flow in its path [51]. Yet a very important phenomena is being left out from all these models, the diffusion of the quasiparticles from the moving vortex core into the superconducting matrix, changing the shape and size of the vortex. This idea was first introduced by Larkin and Ovchinnikov (LO) and is essential for the explanation and understanding of one of the causes of the nonlinear regime and the flux flow instability (FFI).

2.3.2 Flux flow instability

Larkin and Ovchinnikov model

Larkin and Ovchinnikov were the first to address the nonlinear electrical resistivity in the *I-V* curve of a dc-driven vortex system and described the FFI emerging at temperatures close to T_C [16]. The FFI is an abrupt jump from a low resistive state into a normal conducting state. The FFI can simply occur due to self-heating in the sample caused by moving vortices. This is essentially Joule heating from the vortex core normal conducting electrons. Yet, the FFI is present even in thin films coupled to low-temperature baths. LO described jumps as a consequence of high vortex velocities and a finite energy relaxation time τ_ϵ. The order parameter of a vortex moving with velocity v changes on the time scale of $\tau_\triangle \approx \xi_0/v$. Considering that the time $\tau_\triangle$ is shorter than the normal electron energy relaxation time (i.e., the inelastic scattering time) τ_ϵ, the energy of normal excitations increases in the wake behind the vortex and decreases inside the vortex core. Thus, the quasiparticle distribution function inside the core is changed. Near T_c, the order parameter is very sensitive to the quasiparticle distribution function, leading to a shrinkage of the vortex core [52]. Since $\tau_\triangle$ is becoming shorter with v, more and more electrons are left behind, and the diameter of the vortex is becoming smaller with increasing velocity. LO further calculated how the change of the vortex size affects the viscous drag of the medium. They found the following dependence on the velocity

$$\eta(v) = \frac{\eta(0)}{1 + \left(\frac{v}{v^*}\right)^2}. \tag{2.10}$$

v^* is the newly defined critical velocity. The viscous drag decreases with increasing velocity and the friction force $F_\eta = \eta(v)v$ increases until it reaches a maximum at v^* and then starts to decrease. Adding this force to the opposite directed F_L results in the final force F_{tot} on the vortex as

$$F_{tot} = F_L + F_\eta = \eta v + \frac{\eta(0)}{1 + \left(\frac{v}{v^*}\right)^2} v. \tag{2.11}$$

The viscous drag constant η is chosen here in a way to ensure a transition to the normal state at the pair breaking current. The plot of the absolute value of F_{tot} is shown in figure 2.5 (a). For $\eta(0) > 8\eta$, the force has an N-shaped dependency [53]. Hence, for a voltage-driven measurement, the measured current will experience the same N-shaped dependency with a peak at $V^* = v^* Bl$, where l is the distance between the voltage contacts. For a current-driven measurement, however, there is an upward curvature followed by a sudden switch to the higher conductive state. Driving the current up and then down again reveals a hysteresis behavior as shown in figure 2.5 (b). The upward curvature is what we previously described as the nonlinear region, and the sudden jump is the FFI. LO directly linked the critical velocity v^* to τ_ϵ with

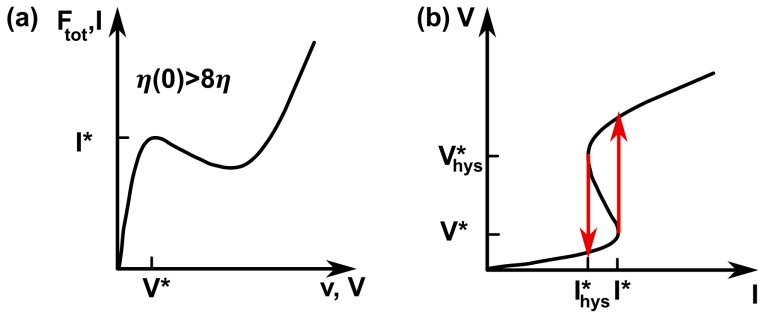

Figure 2.5: The N-shaped dependency of the total force on a vortex in (a) has the same shape as the voltage driven I-V measurement. The current driven measurement in (b) reveals a hysteresis with a transition during current-ramp-down at I^*_{hys} and V^*_{hys} .

$$v^* = \frac{D^{1/2}[14\zeta(3)]^{1/4}(1-t)^{1/4}}{\sqrt{\pi\tau_\epsilon}}, \tag{2.12}$$

where D, ζ and t denote the electron diffusion coefficient, Riemann zeta function and the reduced temperature T/T_C, respectively. This expression is again valid only for temperatures close to T_C, usually a good agreement with experiment is down to 80% of T_C.

Klein *et al.* used a simple model to further refine the LO mechanism [54]. A vortex motion creates an electric field that accelerates the quasiparticles within the vortex core. They start to bounce of the boundary between the normal vortex core (N) and the superconducting matrix (S) by the laws of Andreev reflection. This states that an electron with energy lower than the superconducting gap at the N/S interface can only penetrate into S by creating a Cooper pair in S and reflect back a hole into N. A similar Cooper annihilation and electron creation process occurs when a hole interacts with the N/S boundary. At each of the reflections the quasiparticle energy gets raised. Once the energy is in the order of twice the superconducting gap, the quasiparticle can escape the moving core, provided that the single-electron diffusion free path is larger than the vortex core size. The escape of the electron causes a shrinkage of the vortex core. It is further argued that a narrower vortex core can move more easily through the material because of a decrease in the viscosity and its velocity grows. A higher vortex velocity again leads to more dissipation. Ultimately, an avalanche process is kicked off, causing the FFI to occur.

Following these principles, Klein obtained the same expression for η as LO in 2.10. He also similarly attributes the finite τ_ϵ to cause the nonlinearity in the I-V curves. His expression for v^* differs from that of LO, nevertheless has the same dependence on T and τ_ϵ. The experiments though revealed a further dependence of v^* and that on the applied magnetic field.

Bezuglyj and Shklovskij model

Whilst LO assumed the phenomena of nonlinearity and FFI only as a consequence of finite τ_ϵ, these can also be a consequence of self-heating as mentioned in the beginning of this chapter. Bezuglyj and Shklovskij (BS) noted that self-heating of electrons is significant at large magnetic fields, due to a slow rate of heat removal in the sample that is inevitable in experiment [55]. Combining the LO model with the heat balance equation, they calculated the transition field B_T. For applied magnetic fields B lower than B_T the FFI is caused mainly by the LO mechanism, and at fields higher than B_T overheating dominates as the FFI mechanism due to weak heat removal. The transition field is given as

$$B_T = 0.374\, k_B^{-1}\, e_0\, R_\square\, h\, \tau_\epsilon, \tag{2.13}$$

where k_B, e_0, $R_\square$ and h are the Boltzmann constant, the elementary charge, sheet resistance and the heat transfer coefficient.

Heat removal can be carried out in two different ways depending on the relation between the mean free phonon length l_{ep} and the effective thickness d_{eff} [56]. The effective thickness is defined as $d_{eff} = d/\alpha$, where d is the sample thickness and α is the mean probability of phonon transmission from the superconducting film into the substrate. If $l_{ep} \ll d_{eff}$, the excited phonons are reabsorbed in the superconducting film and the film temperature rises above the substrate temperature. This process is known as Joule heating. If, on the other hand, $l_{ep} \gg d_{eff}$, then the phonons relax into the substrate. This process is called the electron overheating process and in this regime the heat transfer coefficient h is dependent on the electron-phonon scattering time τ_{ep}.

The BS theory, moreover, introduces an approach how to analyze FFI data in order to gain information about τ_ϵ, h and B_T. The following scaling law was found :

$$\begin{aligned} \frac{E^*}{E_0} &= \frac{(1-f(b))(3f(b)+1)}{2\sqrt{2}f(b)^{3/4}(3f(b)-1)^{1/2}}, \\ \frac{j^*}{j_0} &= \frac{2\sqrt{2}f(b)^{3/4}(3f(b)-1)^{1/2}}{(3f(b)+1)}. \end{aligned} \tag{2.14}$$

Here E^* is the electric field defined as the critical FFI voltage V^* divided by the length of the voltage contacts l. j^* is the critical current density that corresponds to the current density at which the FFI was observed. The remaining parameters are

$$E_0 = 1.02 B_T (D/\tau_\epsilon)^{1/2}(1-t)^{1/4}, \tag{2.15}$$

$$j_0 = 2.62(\rho_n\, e_0)^{-1}(D\,\tau_\epsilon)^{-1/2} k_B T_C (1-t)^{3/4}, \tag{2.16}$$

$$f(b) = [1 + b + (b^2 + 8b + 4)^{1/2}]/[3(1+2b)] \tag{2.17}$$

with the reduced magnetic field $b = B/B_T$. The physical meaning of j_0 is the current density j^* where the FFI point has $V^* = 0$. This should be the jump occurring at zero applied magnetic field.

By fitting the measured FFI data one obtains results for j_0 and E_0. The expressions for power

$$P^* = E^* j^*, \tag{2.18}$$

$$P_0 = E_0 J_0 = \frac{h}{d}(T_C - T) \tag{2.19}$$

allow then to calculate the heat transfer coefficient h. Plotting P^*/P_0 vs B and fitting to

$$P^*/P_0 = (1 - f(b)) \tag{2.20}$$

yields B_T.

Finally, from equation 2.13 we obtain the energy relaxation rate τ_ϵ. In the overheating regime, one can hence determine both τ_{ep} and and τ_{ee}. τ_{ep} is defined from

$$h = \frac{c_e d}{0.22\tau_{ep}} \tag{2.21}$$

with c_e being the electron specific heat defined by $c_e = (\pi^2/3)k_B^2 N(0)T$ (here $N(0) = m^2 v_F/\pi^2\hbar^3$ is the density of states). We use an estimate for the Fermi velocity, $v_F = 10^8$cm/s, and the value 224 J/m^{3}K for c_e. τ_{ee} is then determined from from the fitted τ_ϵ. BS defined the inverse of the energy relaxation τ_ϵ to be equal to the sum of the inverse of the electron phonon τ_{ep} and inverse of the the electron electron relaxation times τ_{ee}.

In the BS theory $v^* \propto h(1-t)^{1/4}B^{-1/2}$. This is in agreement with the experimentally observed v^* dependence on low magnetic field that could not be explained by the LO theory alone. Refinements of the LO theory were done by Doettinger that include the same $B^{-1/2}$ dependence as found in the BS theory.

Doettinger model

LO assumed that the non-equilibrium electron distribution is spatially uniform throughout the entire sample, but Doettinger noted that this is only true whilst $v^*\tau_\epsilon$ is larger than the intervortex distance a. As the applied magnetic field gets smaller and the intervortex distance grows, we get to a point where $a = v^*\tau_\epsilon := a_{cr}$, causing the distribution to be strongly spatially inhomogeneous. At fields below the cross-over field $B_{cr} = 1.14\Phi_0(v^*\tau_\epsilon)^{-2}$ the system is recovering to a spatially homogeneous state by allowing v^* to grow accordingly to the increase of a with decrease in the applied magnetic field. Since $a \propto B^{-1/2}$, v^* exhibits the power law $v^*(B) \approx B^{-1/2}$ for all fields lower than B_{cr} [57]. For magnetic fields above B_{cr}, v^* is constant, which is consistent with the LO theory. The exact definition of v^* in the Doettinger (DO) model is

$$v^* = \frac{D^{1/2}[14\zeta(3)]^{1/4}(1-t)^{1/4}}{\sqrt{\pi\tau_\epsilon}}\left(1 + \frac{a}{\sqrt{D\tau_\epsilon}}\right). \tag{2.22}$$

We see that in high fields when $a \ll \sqrt{D\tau_\epsilon}$, the equation approaches the LO defined, constant in field, v^*.

Pinning effects on FFI

The experiments on Nb films performed by Grimaldi *et al.* found a second crossover magnetic field B_{cr1} for the evolution of $v^*(B)$ [58]. For fields smaller than B_{cr1}, v^* increases with increasing applied magnetic field. For fields above B_{cr1} the dependence crosses over to the one found in the DO model, v^* decreases with increase in field. Note that this behavior is present for samples with strong disordered pinning. As discussed by Silhanek *et al.* this behavior can be explained by taking into account the intensity, type, and distribution of the pinning centers present [59]. Weaker pinning allows for coherent dynamics and stronger ordering of the vortices, which results in a very narrow delta-function-shaped velocity distribution. However, strong pinning to strongly disordered defects leads to a broad distribution of velocities. Since the FFI is an avalanche process, it is enough for a single vortex velocity to reach v^* for the entire system to collapse. However, the velocity measured in the experiment is the mean velocity $\langle v \rangle$. In the case of weak pinning, the narrow distribution accounts for a smaller deviance between $\langle v \rangle$ and v^* in comparison to a larger deviance in the broad distribution present for the strong pinning case. According to this study, weaker pinning accounts for a higher v^*. This explains the initial v^* increase with field for very low fields. At these low fields, as the field is being raised and the density of vortices compared to the number of pinning centers grows and the vortex-vortex interaction grows, pinning is effectively decreased. Vortices are hence ordering themselves and the velocity distribution narrows, which in end-effect makes the measured v^* to grow. In 2017 Shklovskij et al. found similar observations of the pinning effects on v^* based on a phenomenological study. In their work, they incorporated pinning into the combined BS-LO theory [60].

Local flux-flow instability model

LO in their theory described a FFI that occurs after the nonlinear part of the *I-V*. In experiments, the FFI is often observed already in the linear part. Bezuglyj *et al.* attributed this to be a consequence of localized normal conducting regions. Unlike in the LO theory where the FFI is assumed to happen all at once all over the sample region, an FFI can be triggered by only a minority of vortices at a certain location. One can observe such behavior in superconducting films with specific areas of defects or granularity. The defected areas pin vortices down, whilst vortices in-between them can move very fast. These moving vortices overheat and a temperature gradient along their path builds up [61]. If the temperature is higher than T_C, a switch to the normal conducting state occurs, but only along this path. A study on resistive domains showed that a normal conducting domain will grow past the S/N boundary only if the current density is higher than the minimum current density for the propagation of a normal domain J_P [62]. J_P depends on the ratio between Joule heating of the normal domain and its heat transfer. If the current density of the normal domain is lower than J_P, the normal domain will eventually shrink and the superconductivity will be recovered. However, if the current density is larger, the normal domain spreads into the entire sample, and an FFI is observed. The location of the FFI in this scenario is in the

linear part of the I-V curve. The found phenomena are supported by calculations of the BS-model-electron-overheating in a narrow bridge, where vortices are moving but are pinned everywhere outside of this bridge. This model is a refinement of the original BS model.

Edge-controlled instability model

A theoretical study of the FFI with consideration of sample edge effects was published by Vodolazov based on TDGL linked with the heat balance equation [33]. The use of the heat balance equation for the description of FFI is known to us from the BS model. However, in the BS model the heating and cooling effects were spatially averaged throughout the entirety of the sample, which covers the local effects caused by moving vortices. The edge-controlled instability model is another localized model. In this model, the heat balance equation is applied to each individual quasi-particle. In addition, the model takes vortex-surface interactions into account. Chapter 2.2.1 covers vortex-surface interactions. The edge barrier for vortex entry causes a local area with higher current density at the edge of the sample, leading to larger Joule dissipation and higher temperatures. Close to I^* vortex rivers with suppressed superconductivity are created across the sample starting at the hot edge. Abrikosov-Josephson-type vortices move in an ordered way along these normal conducting rivers. Returning to the considerations of Silhanek [59] this ordered motion allows the vortices to move very fast. The group of Embon *et al.* also reported an observation of Abrikosov-Josephson vortices in vortex rivers in a sample with a constriction using a nanoscale SQUID-on-tip imaging technique [24]. To examine the theoretical predictions of Vodolazov, Dobrovolskiy *et al.* realized an experiment on a sample with a close-to-perfect edge barrier and achieved vortex velocities of 10-15 km/s [63]. An experiment on a sample with a single notch milled on one side of a superconducting sample causes the so-called current crowding effect in the sample, leading to a higher current density at the tip of the notch and acting as a preferred site for vortex entry. This additional single defect causes symmetry breaking, destroys the ordered motion present for the perfect edge sample, and reduces v^*. One of the goals of this thesis was to perform experiments on samples with different quality edges as a result of different fabrication techniques and to compare how it influences the vortex dynamics and location of the FFI. The results of this study can be found in the chapter 5.

The edge-controlled instability model is made for materials, where $\tau_{ee} \ll \tau_{ep}$, this is essentially the case for dirty superconductors. The energy relaxation time in this model is then expressed as

$$\tau_\epsilon = \tau_{ep}/4.5 + \tau_{esc}(1 + C_e/C_p). \tag{2.23}$$

Here, τ_{esc} is the time it takes for non-equilibrium phonons to escape into the substrate, and C_e and C_p are the heat capacities of electrons and phonons at T_C.

Further FFI mechanisms

Throughout the years, various other mechanisms, distinct from the LO mechanism, were studied as additional causes of an FFI, e.g., crystallization of the vortex system [64], thermal runaway effect due to Joule heating at the current contacts [65], the Kunchur hot-electron instability [66] at low temperatures, phase-slip centers and lines [67], or formation of localized normal domains due to an inhomogeneous current distribution [49]. To exclude Joule heating as the cause of the FFI in all presented measurements, we looked at the power dissipation P in various fields. P has shown a clear field dependency. This contradicts a Joule heating caused FFI, where P should be independent of the magnetic field [68].

2.3.3 Relaxation times

In the beginning of this chapter on non-equilibrium phenomena, we mentioned that these phenomena are characterized by relaxation times. Some have already been mentioned throughout the chapter. Here we also summarize the information in the following table.

TDGL	very large $\tau_\triangle$
Generelized TDGL	$\tau_\triangle > \tau_{ep}$
LO and DO Model	$\tau_\epsilon \simeq \tau_{ep}$
BS Model	$1/\tau_\epsilon = 1/\tau_{ep} + 1/\tau_{ee}$
TDGL + heat balance equation	$\tau_{ee} \ll \tau_{ep}$ and $\tau_\epsilon = \tau_{ep}/4.5 + \tau_{esc}(1 + C_e/C_p)$

Table 2.1: Relaxation times of non-equilibrium phenomena as used in various theories

All of the derivable relaxation times from these theories are for temperatures close to T_C.

2.4 Superconducting single photon detectors

One of the reasons why we are interested in energy relaxation times is to improve SSPDs (figure 2.6). The working principle of an SSPD is the detection of a photon by measuring a voltage jump across the detector. This voltage jump appears as a consequence of the photon colliding with the superconducting detector. The energy of the photon is translated into heat that locally raises the temperature above T_C and superconductivity is locally broken down, creating a hot spot [11, 69]. In order to detect even the smallest of energies, it is important to operate the detector at temperatures and bias currents that put the detector in a close-to-pair-breaking state. Depending on the properties of the material and the detector shape, the hot spot can either spread and a normal conducting band will stretch throughout the entire width of the detector, or only a hot spot remains with current having to flow around the hot spot. Whilst in the first case the voltage jump appears due to what is essentially a Josephson weak link, in the second case the voltage jump is a FFI appearing due to fast vortex motion triggered by the current crowding around the hot spot [70]. In both cases though, the energy

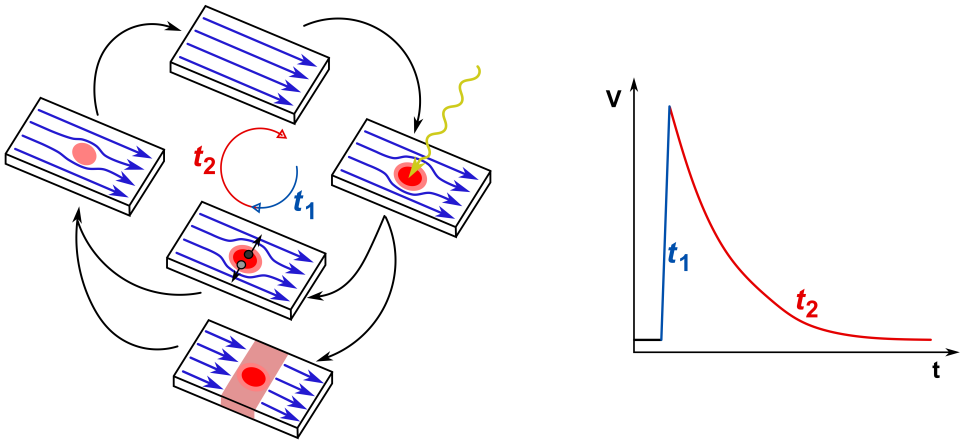

Figure 2.6: The working cycle of a superconducting single photon detector. First the incident photon (yellow) creates a hot spot (red). Through inelastic scattering the spot widens and the current is redirected to flow around it, locally raising the current density. If the current density exceeds critical values a normal conducting band (pink) across the detector appears and a voltage jump is registered (t_1 in the V-t curve). If no heated band is created, increased current density initiates vortex-antivortex flow (grey spots). The fast vortex flow leads to a FFI voltage raise (t_1 in the V-t curve). In both cases the hot spot eventually shrinks, superconductivity is recovered and the voltage returns back to its initial low state (t_2 in the V-t curve).

eventually dissipates, superconductivity recovers, and the voltage returns back to its initial low state. Only once the voltage fully returns back is the detector ready to detect another photon. This means that there is a certain dead time, when the detector cannot detect any new incoming photons. A good detectors dead time should be held at minimum, and thus a quick energy relaxation, short τ_ϵ, is important.

In SMSPDs (micrometer-sized SSPDs) the voltage jump mechanism is theorized to appear due to the fast vortex FFI [70, 71]. Therefore, the vortex motion itself and the location of the FFI is important. In this thesis, all studied structures are patterned to replicate the shape of a SMSPD.

Chapter 3

Methodology

The following chapter includes details on sample fabrication and sample characterization, details of all the equipment and procedures used during measurements, and information about programs and methods used for numerical simulations.

3.1 Film fabrication methods

All films studied in this thesis were produced using DC magnetron sputtering. To perform electrical transport measurements on these films, the samples were structured using three different techniques: laser beam etching, focused ion beam (FIB) milling, and UV lithography in conjunction with lift-off.

3.1.1 DC magnetron sputtering

A sketch of the dc magnetron sputtering method can be found in figure 3.1. This method is categorized into a group of methods that apply physical vapor deposition (PVD) to thinly coat desired surfaces. PVD works by letting a solid target transition into a vapor phase that later condenses onto a surface. In order for the transition to take place, one can utilize various methods, for instance heat sources (evaporation PVD), or, as in this case, sputtering. A negative voltage is applied to a conductive target material, whilst the substrate is placed under the positive anode. The entire chamber space where the target and substrate are placed must be evacuated to at least 10^{-7} mbar before an inert gas, argon, is inserted. Electrons accelerated in the electric field ionize the argon gas. This leads to a plasma (of argon ions and secondary electrons) formation with a visible glow discharge. The positively charged argon ions (Ar^+) are then accelerated towards the cathode, where, due to their relatively high mass, they are able to sputter out the target atoms. These then travel back through the inert gas towards the substrate, where they form a set of tightly bound atomic layers. When the pressure in the chamber is high, the sputtered target atoms collide with the inert gas a lot on their way towards the substrate, causing them to scatter. The scattered target atoms approach the surface under nonperpendicular angles, making them stick to protruding

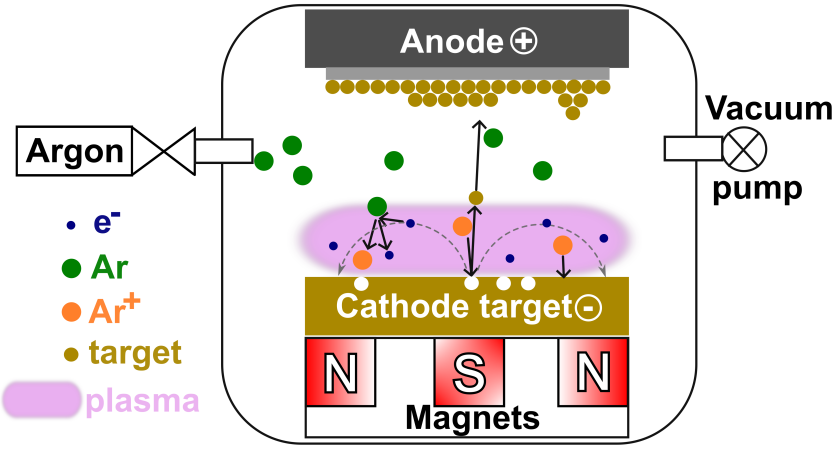

Figure 3.1: Sketch of the dc magnetron sputtering process. Ar inert gas atoms get ionized by electrons in the localized plasma and are accelerated towards the target cathode, where they sputter out atoms of the target material. The target atoms afterwards travel towards the substrate underneath the anode, where they form thin layers of the sputtered film.

atoms, which, in turn, causes a very nonuniform coating due to shadowing. However, lowering the pressure in the chamber would decrease the ionization efficiency and thus lowering the sputtering rate.

The trick to lowering the sputtered target-atom scattering but keeping the ionization efficiently high is in localizing the plasma. This is done by placing permanent magnets below the cathode area. The crossed electric and magnetic fields result in a Lorentz force acting on the secondary electrons being ejected from the cathode. This force traps them in a circular motion around and close to the cathode. In the cathode region they ionize argon and create a very dense localized plasma even at low inert gas pressures due to the confined space. The dense plasma results in many collision events between Ar^+ and the target, keeping the sputtering rate high, whilst the now possible low inert gas pressure (10^{-3} mbar compared to 10^{-2} mbar with no magnetic field) ensures low scattering and consequently a uniform coating. Another advantage of utilizing magnetic fields in the process of magnetron sputtering is a lower operating voltage at the same efficiency rate when compared to classical dc sputtering (couple hundred V instead of couple kV). Comparing dc magnetron sputtering to evaporation PVD, magnetron sputtered target-atoms have much larger energies than evaporated atoms. Whilst evaporated atoms have energies corresponding to their binding energy, typically somewhere around a single eV depending on the target material, magnetron sputtered atoms can have energies anywhere between 5 and 50eV. The high energy atoms give magnetron sputtering the advantage of fast coating procedures (∼100Å/s, but only ∼1Å/s for dielectrics), as well as uniformity of the sputtered film compared to films made through evaporation. All of this makes dc magnetron sputtering a great technique to create thin, uniform films.

The inert gas pressure, voltage, sputtering time, substrate temperature, target-substrate distance, and target and substrate material have all an impact on the final thickness and

texture of the sputtered film.

The Nb films were sputtered by Sebastian Kölsch at the Goethe University in Frankfurt am Main, Germany, on a custom-build setup. The MoSi films were sputtered by Mikhail Mikhailov at the B. Verkin Institute for Low-Temperature Physics and Engineering of the NAS of Ukraine in Kharkiv.

3.1.2 Laser beam etching

By pulsating a laser source, we can hit the surface of a thin film with high-energy photons at specific intervals. The energy used must be high enough to heat the film up to its melting point. The material then melts and is locally displaced. In thin films laser etching can electrically isolate regions from one another by completely removing the films material in the etched path and leaving a non-conductive spacing between the two regions. Laser etching is thus used to cut bridges and contact pads for electrical transport measurements. Our samples were etched using the LGI-505 gas laser source with a 337-nm wavelength, a pulse duration of 7 ns, and with an efficiency of up to 1000 pulses per second. The laser beam leaves behind an overlapping circle pattern that resembles that of a pattern left after metal welding (figure 5.1 (a)). The laser beam has a focal spot diameter of about 6 μm and causes a further evaporation of the film within a distance of an additional 2–3 μm around the spot size. The edge of the laser pattern determines the edge of the film. This edge has a sawtooth-like strip edge profile, meaning that laser etching leaves behind a fairly rough edge. The power of the laser beam, focal spot size, and speed of beam rastering determine the exact appearance of the edge.

3.1.3 Focused ion beam-induced milling

The ion beam source in an FIB system is a liquid metal ion source (LMIS). In our case, the metal used was gallium. In an LMIS a tungsten needle is submerged in a melted metal reservoir (figure 3.2 (a)). The metal is melted by passing current through a heating coil. The melted metal then flows towards the $\sim 4\,\mu m$ wide tip of the needle. An electric field is created between the reservoir and a torus-shaped extraction electrode, placed in front of the needle, by applying a high voltage between the two. The liquid gallium is drawn by the field into a conical shape and forms a Taylor cone at the tip of the needle with a radius down to 2 nm in size. Here, it comes to field evaporation in the form of ion emission at the cone apex. Once the ion beam hits the film surface, ions with keV energy have a penetration of only a couple of atomic layers. On impact, due to their high mass compared to electrons, it comes to displacement of atoms in the film and to sputtering of atoms, ions, and secondary electrons. The gallium ions can either be backscattered or stay implanted in the film. In thin films the beam can etch away material, and so can be similar to laser etching used for film patterning. FIBs are often integrated in scanning electron microscopes, which gives these systems a great advantage of a live SEM image to monitor the FIB processing. For our samples, we have used the dual-beam SEM/FIB system FEI Nova NanoLab 600 at 30 kV (30 pA). The spot

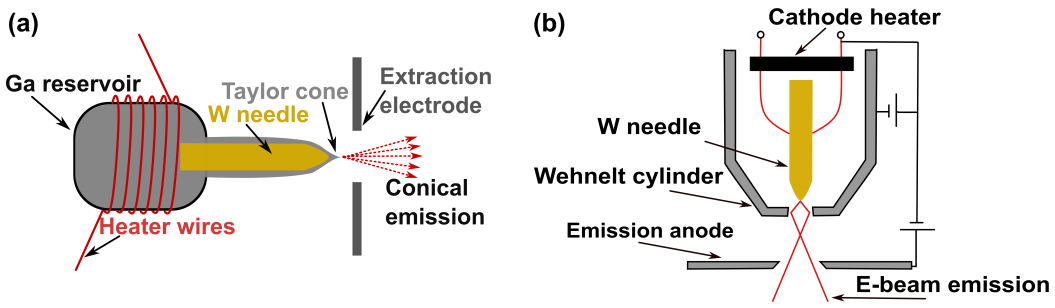

Figure 3.2: Sketch of a liquid metal ion source (a) and a Schottky electron gun (b).

size is about ~ 20 nm in size and the gallium ions are implanted in the sample another ~ 10 nm from the spot. Overall, FIB milling leads to creating much smoother edges as compared to laser etching.

3.1.4 UV-lithography in conjunction with lift-off

Whilst the previous two techniques followed only after the film was dc magnetron sputtered to pattern it, the method of UV-lithography to pattern films has steps that precede the magnetron sputtering phase. Any photolithography starts with the coating of the substrate with a photoresist. Photoresists are light-sensitive materials that change their response to photoresist developers after exposure to light. In case of positive resists, light exposed areas of the resist will decompose in the developer, whilst in negative resists, shielded areas decompose and the exposed areas stay put. By placing photomasks over resists we can control which areas get exposed to light and which remain shielded. Hence, we can create patterned layers of resist on the surface of substrates. These can then be coated by a metallic layer. The layer sticks both on top of the resist and in the resist-free spots directly to the substrate. After the remaining resist is removed by a chemical solvent, the metallic layer remains in place only where it was deposited directly on the substrate. Here, we will describe the detailed fabrication steps using a positive resist. This calls for a photomask that only allows light in areas where in the end we want our metal deposited.

1. Cleaning: To ensure that the substrate is clean, dry, and free of organic particles, the substrate must be rinsed in acetone and isopropyl alcohol (IPA) and bathed for about 4 minutes in an ultrasound IPA filled bath. Nitrogen gas is used to dry the substrate.

2. Spin coating: LabSpin 6 by SÜSS MicroTec is used to spread a droplet of positive UV-photoresist AZ 701 MIR by fast rotation in an even layer over the substrate. See figure 3.3 (2).

3. Soft bake: This process is required to harden the resist as well as to improve its adhesion and to improve the stability of the lithographic performance. For this purpose, the coated substrate is heated to 90°C for 90 s (depending on the resist used).

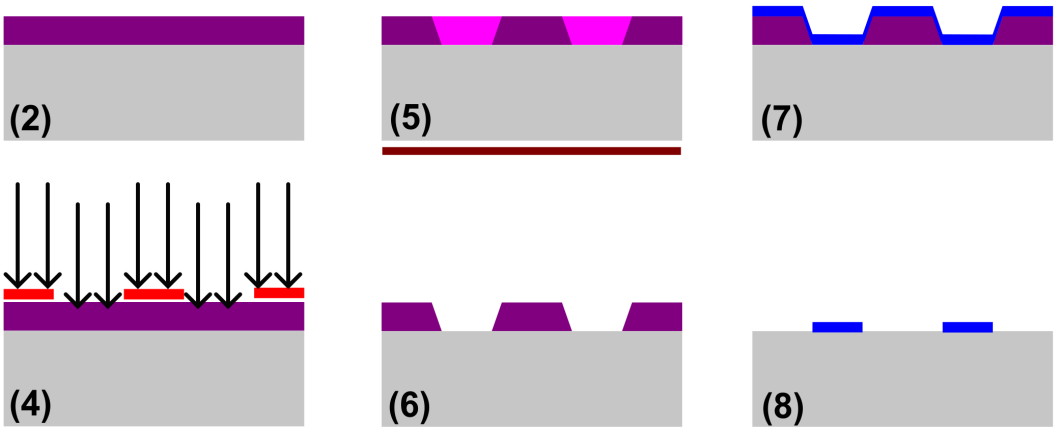

Figure 3.3: Shown are the UV-lithography steps: (2) Spin-coating, (4) Exposure, (5) Post exposure bake, (6) Development, (7) DC magnetron sputtering and (8) Lift-off.

4. Exposure: The MA8 mask aligner from SÜSS MicroTec was used to align the photomask in direct contact with the substrate. The coated substrate is then illuminated through the photomask with a UV dose of 270 mJ/cm^2 generated by a Hg lamp with a wavelength range of 350-450 nm. See figure 3.3 (4).

5. Post-exposure bake: This process is recommended to maximize the process latitude (a wider range of light exposures will lead to acceptable results) and to weaken the standing-wave effect. The standing wave effect is caused by the back scattered light from the substrate that interacts with the light passing downwards, resulting in a ripple edge of the resist after development. The post-exposure bake temperatures should be in the 110 to 115°C range. See figure 3.3 (5).

6. Development: A compatible developer to the resist must be used to decompose the light exposed positive resist. In this case for AZ 701 MIR the used compatible developer is the AZ 726 MIF. The substrate is bathed for 60 s in the developer, washed with deionized water, and dried with nitrogen gas. See figure 3.3 (6).

7. DC magnetron sputtering: The sample is then covered with a metallic layer in the process described in section 3.1.1. See figure 3.3 (7).

8. Lift-off: The last step is to remove the remaining resist that is now covered with a layer of metal. Removing the resist will lift it off together with the metal layer leaving behind a metallic film only where it was deposited directly onto the substrate. The used chemical solvent for lift-off is a dimethylsulfoxid (DMSO) based solvent, TechniStrip Micro D350, at 90°C for 1 to 1.5 hours. In the end a final cleaning of 4 minutes in an IPA filled ultrasound bath is performed. See figure 3.3 (8).

The edges of films pattered with UV-lithography have a roughness between the roughness of the very rough laser beam etched films and the considerably smooth FIB milled films, but

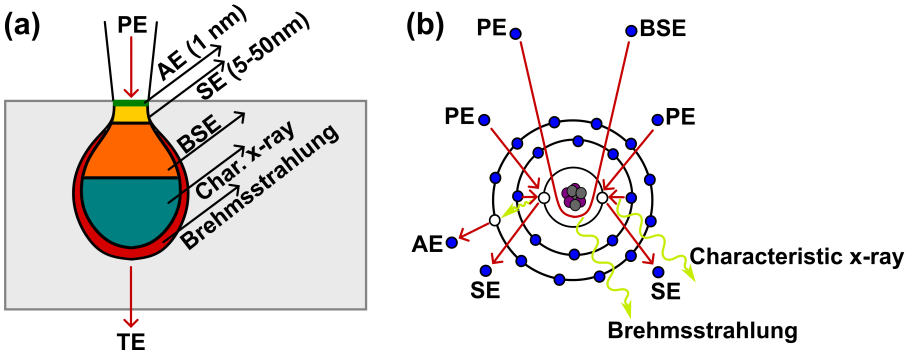

Figure 3.4: The incident beam consisting of primary electrons (PE) can lead to the emission of the Auger electrons (AE), the secondary electrons (SE), the characteristic X-ray, the continuum X-ray (Bremsstrahlung), and of the backscattered electrons (BSE). Electrons detected on the opposite side of the sample (grey) are the transmitted electrons (TE). In (a) is shown the depth of origin of these detectable signals and in (b) is a schematic explanation of the events creating the signals in an atom.

closer to the FIB milled edges.

3.2 Film characterization methods

For characterization of the films the used techniques were scanning electron microscopy (SEM), energy-dispersive X-ray spectroscopy (EDX), transmission electron microscopy (TEM), atomic force microscopy (AFM), and optical microscopes. Many of the about to follow techniques use electrons for investigation and imaging of samples. The reason for this is their very good resolution compared to, for instance, visible light used in optical microscopy. Resolution is related to wavelength, as smaller wavelengths can resolve greater details. Due to the wave-particle duality, electrons have a wavelength given by the de Broglie wavelength: $\lambda_B = \frac{h}{p}$, where p is the particle momentum. Expanding this relation with the relativistic energy-momentum relation we get: $\lambda_B = \frac{hc}{\sqrt{E^2 - E_0^2}} = \frac{hc}{\sqrt{E_{kin}^2 - 2E_{kin}E_0}}$. Here E_0 is the rest energy of the electron ($= m_0c^2$) and E_{kin} is the kinetic energy of the electron. We see that the more energetic the electrons are, the smaller is their wavelength and the better is their resolution. For instance an electron accelerated with 200 kV voltage has a 2.51 pm wavelength, compared to hundreds of nanometers for visible light. This allows electronmicroscopy to have an atomic or close to atomic resolution.

3.2.1 Scanning electron microscopy

In an SEM instrument, a beam of electrons is shined onto an examined sample. These, what we call the primary electrons (PE), can interact with the sample in various ways. They can lead to emission of Auger electrons (AE), secondary electrons (SE), characteristic X-ray or continuum X-ray (Bremsstrahlung), or they can be reflected back as backscattered

electrons (BSE) (for understanding, see figure 3.4). The choice of detector then establishes the observation particle/radiation and thus the measurement. The detection of characteristic X-rays for elemental analysis is described in the following section. AE, SE and BSE differ in the penetration depth as well as the energy they have when exiting the sample. SE are the lowest energetic ones with energy on the order of 50 eV, and they originate from a depth of 2-50 nm. They are the most commonly used imaging mode for SEM. The primary beam scans the sample surface point by point. For SE the resolution is about 10nm. The intensity of the detected signal given by the number of emitted SE is what gives the final image. When the primary beam hits an angled surface, like the edge of a mound or a valley, more SE escape at this point compared to a flat surface. This angled region is then displayed lighter in the final image. SE detection in SEM is therefore a great technique to image surface morphology, such as roughness or shape of the surface. Imaging of non-conducting surfaces might be difficult though, because charging effects, where the primary electrons accumulate on the surface, cause various distortions in SE imaging.

BSE have a much higher energy and reach into larger depths than SE ($\sim 1\,\mu$m). This lowers their resolution, but the scattering process is dependent on the elements present. BSE get scattered much more on larger atoms (large Z) than on small ones (small Z). The intensity is thus larger for elements with larger Z and they appear lighter in the final image. Detection of BSE can not be used for exact elemental analysis and stoichiometry deduction, but it can visualize different phases and elements well.

Some SEM instruments can also have an AE detector. This was not the case in the used dual beam FEI Nova 600 NanoLab SEM/FIB. AE have desecrate energies given by the three shells involved in AE creation. The desecrate energies can be directly linked to the atomic number Z and thus provide elemental composition. In this thesis, the elemental analysis was instead performed using EDX spectroscopy as described in the following section.

In the SEM instrument, the electron beam is produced by a Schottky electron emitter (figure 3.2 (b)). A very sharp tungsten tip is heated to 1800 K. This temperature is still too low for thermoelectrons to emit. The tungsten-tip emitter is surrounded by the Wehnelt cylinder that is set to a negative electrical potential relative to the emitter. A strongly positively biased, relative to the emitter, anode is placed in front of the Wehnelt cylinder. The strong electric field between the anode and the emitter can be used to lower the escape energy of electrons, whilst the Wehnelt cylinder focuses the e-beam. The electrons are emitted with keV energy. FEI Nova 600 NanoLab has in-lens electron detectors. SE are guided by a magnetic field upward along the optical axis of the objective lens towards a detector, an anode that detects an electron by a voltage rise.

3.2.2 Energy-dispersive x-ray spectroscopy

This elemental analysis technique is used to determine the composition stoichiometry of the fabricated films. This technique analyzes the characteristic radiation created during a fluorescence event. An incident beam (which can be an electron or X-ray) knocks out an

electron. The hole left behind can be filled by an electron from an orbital that is further placed from the nucleus. The difference in their binding energies is then released in the form of a characteristic X-ray. Moseley's law is an empirical law calculated from the binding energy difference between two levels with quantum numbers n_i and n_f ($n_i > n_f$). The law connects the energy of the characteristic X-ray and the atomic number Z as follows

$$E = E_{n_i} - E_{n_f} = R_H \left(\frac{1}{n_f^2} - \frac{1}{n_i^2} \right) (Z - b)^2, \tag{3.1}$$

where R_H is the Rydberg constant (=13.6 eV) and b is a screening constant dependent on the type of spectral line. For instance for the spectral line K_α, corresponding to a transition from L-shell into the K-shell, the b constant is 1. For the spectral line L_α, corresponding to a transition from M-shell into the L-shell, the b constant is 7.4.

The energy of the characteristic X-rays is detected via a semiconductor diode Si(Li) detector. Photons interact with the detector mainly by a photoelectric effect, creating a swarm of electron-hole pairs. These travel to the opposite sides, and a voltage pulse is detected that can be recalculated into energy. Because the b screening constant reduces the nucleus charge to an effective value depending on the spectral line, a single chemical element in the EDX spectrum has peaks by multiple energy values corresponding to different transitions. The positions of these peaks for individual elements are known and can be fitted. The stoichiometry can then be calculated from the intensity of these peaks. Internal standards of known concentration are used to calibrate the calculation.

In this work, the EDX was performed in an SEM equipped with an EDAX Genesis 2000 spectrometer running at 5 kV (1.6 nA). Notably, EDX works well for elements with Z>11. Elements with lower Z have a higher chance that the initial interaction will result in creation of an Auger electron rather than a characteristic X-ray, so they are hard to detect.

3.2.3 Transmission electron microscopy

TEM can be used for imaging or electron diffraction to gain information about the crystallographic structure. Similarly to SEM an e-beam is shined onto the sample, but unlike in SEM, detected is what gets transmitted through the sample, transmitted electrons (TE). In this manner TEM provides information on the inner structure of samples, but is limited to very thinly sliced samples (below 150 nm). After the e-beam travels through the sample it follows through a series of objective electromagnetic lenses and, in the end, is focused on a scintillator that converts electrons to photons that can be recorded by a charge-coupled device (CCD) camera. A CCD is an array of capacitors that can accumulate charge and convert them to a measurable voltage pulse. An image of the specimen is then reconstructed from the individual array elements, where each element represents one pixel. Different shades of the image correspond to different densities within the sample. By choosing the aperture location below the sample, one can choose to visualize only the scattered electrons (dark mode), or only the nonscattered electrons (bright mode). In dark mode denser materials

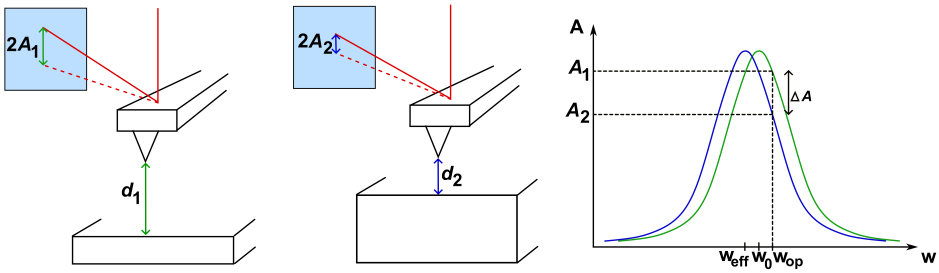

Figure 3.5: The working principle of AFM: The cantilever is oscillated at a constant frequency $w = w_{op}$ above the sample. When the sample is closer to the tip (in distance d_2), attractive forces change the resonance frequency w_0 (of distance d_1) to the new resonance frequency w_{eff}. This change is registered as a change in amplitude A of the laser spot oscillation on the detector from A_1 to A_2.

appear lighter, whilst in bright mode denser areas appear darker. One can also distinguish the high Z elements, that cause more scattering, from low Z elements. The TEM instrument used was the Tecnai F30.

3.2.4 Selected area electron diffraction

Another analysis technique executable on the TEM instrument is the selected area electron diffraction (SAED) technique. Given the discussed wave-particle duality, electrons obey the Bragg's rule during diffraction. An electron wave diffracted on a crystal lattice will interfere constructively only when $2dsin\theta = n\lambda$. Here, d is lattice plane distance, θ is the angle of incidence, and n is an integer number. By adjusting the magnetic lenses in such a way that the back focal plane rather than the image plane lands on the CCD camera, one can observe diffraction patterns. Single crystals result in a collection of bright spots, a larger number of differently oriented crystallites result in bright rings, and amorphous solids result in no clear concentration of signal.

3.2.5 Atomic force microscopy

This surface analysis technique is part of a group of scanning-probe-microscopy techniques. What connects all these techniques in this group is the use of a physical probe that scans the surface. Another technique from this group is the scanning tunneling microscope (STM). However, STM is limited to conducting samples. AFM does not have this restriction, and when compared to further microscopy techniques such as the SEM or TEM, AFM allows for vertical resolution of the surface, making it a great technique for creating topology maps and checking the height of structures and quality of edges after fabrication. A sketch of the working principle of AFM can be found in figure 3.5. The working principle is based on the atomic forces between a very sharp AFM measuring tip ($\approx$ 10 nm) and the probe surface. The most prominent of these forces are the short-range repulsive Pauli-exclusion force and the

long-range attractive Van der Waals force. The final force $F(d)$, plotted against the distance between the tip and the surface d, is thus shaped as the Lennard-Jones potential.

The measuring tip is located at the free end of a cantilever. The cantilever moves vertically, either away from the sample or toward it, depending on d. The deflection of the cantilever Δz is proportional to Hooke's law as: $F(d) = -k\Delta z$, where k is the spring constant of the cantilever. Hence, measuring Δz gives us information about the force $F(d)$, and this gives us information about the distance d and consequently the surface height. The use of this technique can be damaging to the surface, so to avoid contact of the tip with the sample during rastering, which can damage the sample surface, one uses the non-contact, dynamic mode instead. In this mode, piezoelements oscillate the cantilever above the sample surface with a certain frequency. The resonance frequency of the cantilever is given as $w_0 = \sqrt{\frac{k_0}{m}}$, just as in a free harmonic oscillator. When the cantilever approaches the sample, the attractive Van der Waals forces change the effective spring constant to $k_{eff} = k_0 - \frac{\partial F}{\partial z}$, and the resonance frequency changes to a new effective resonance frequency w_{eff}. To detect changes to w_{eff}, one actually drives the cantilever at constant frequencies w_{op} just above w_0 and looks for the change in the amplitude of the oscillation. The amplitude change ΔA at frequencies just above w_0 is highly sensitive to changes in resonance frequency and hence in sample height.

The deflection of the cantilever Δz and the oscillation amplitude A are measured by shining a laser on the backside of the cantilever and observing the location of the reflected laser spot via a photodiode array. The resolution of an AFM is with $\approx 0.1 - 10$ nm on the atomic scale. In this work, two AFM instruments were used, the Dimension Icon by BRUKER and the Nanosurf EasyScan 2.

3.3 Transport measurements

The transport measurements were performed using the 4-point technique. The sample is prepared in the form of a bridge with 4 leads leading to the bridge from contact pads. Two outer leads are used to pass current through ($I+$ and I -), and the two inner leads are used for voltage readout ($V+$ and V-). The 4-point technique reduces the contribution of the wires to the final resistance measurement. The experimental geometry of the transport measurements can be seen in figure 3.6. First we will introduce the used contacting techniques and afterwards describe the two used systems on which transport measurements were performed.

3.3.1 Bonding techniques

To contact the sample pads to the holders of the used devices, silver paint bonding or the wire bonder machine were used depending on the size of the bonded pads.

Silver paint bonding is performed by gluing down a 50 μm gold wire using a conductive paint. The paint is an adhesive loaded with silver particles. The volume resistivity is about 1 $m\Omega cm$. Usually, the end of a 0.3 mm diameter copper wire was used to leave a droplet of the paint on the pad, and the gold wire was then pushed into the droplet from the side and

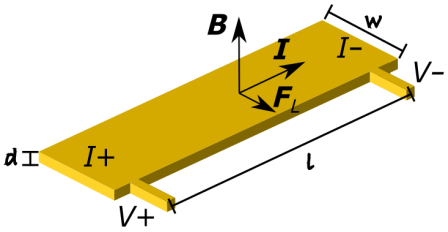

Figure 3.6: Transport measurement geometry for a sample of width w, length l and thickness d. The Lorentz force F_L gives raise to a measurable finite voltage.

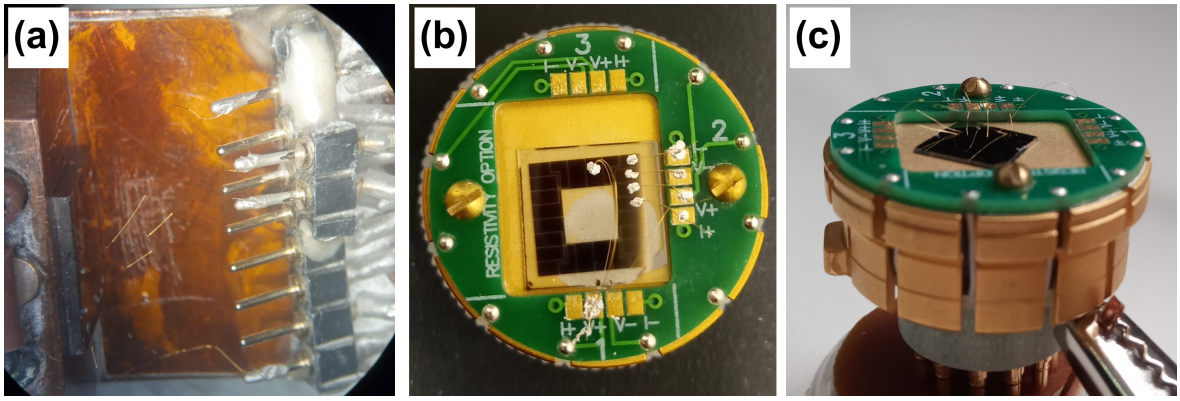

Figure 3.7: Examples of sample silver paint bonding on the holder of the He bath cryostat from Oxford (a) and on to the PPMS puck (b). Wire bonder bonding is shown on the PPMS puck in (c).

let to dry.

The bonder machine used was the HB10 Wire Bonder from tpt. It is a wire bonder with an automatic z-axis movement. The wire bonder was used with a gold wire of 25 μm diameter. There are many attachment techniques, of which the wedge bonding technique was used. During wedge bonding, the wire is threaded angled under the tip of a sharp needle. The needle is then lowered down to the surface of the pad, and an ultrasound is applied. The wire is thus pressured down and vibrated at kHz frequencies. This causes the atoms of the metal wire and the metal substrate to mix. After a couple milliseconds, the two materials fuse together. The parameters to optimize from material to material are the ultrasonic energy (US), the bonder downward force (F), and the ultrasonic bond time (t). Metals actually never get into a melted phase during the bonding procedure, so this bonding is often called friction welding or cold welding. Following parameters were used to bond the pads of the PPMS holder (Bond 1) to golden pads of the sample (Bond 2):
Bond 1 $\rightarrow$ US=220, t= 210 ms, F=300 mN; Bond 2$\rightarrow$ US=240, t= 210 ms, F=350 mN.

Silver paint bonding is sturdier and does not require any parameter adjustments when bonding to different samples, but due to the bonding performed manually it can get very difficult once the pads are smaller than 1mm in either direction. When the pads are very small, the silver paint can spread to surrounding pads and short-cut them with each other.

The wire bonder, on the other hand, can bond in an area of 25 μm diameter. The difficulty of using the wire bonder is that it requires one to find the correct parameters to use for your samples. The wire bonder bonds are also very fragile, and the bond sturdiness is very dependent on the surface roughness. For measurements on the Oxford magnet system, only silver paint bonding was done because the other end of the gold wires had to be glued to the magnet holders pins, something that is not possible using the wire bonder. Some examples of bonding are shown in figure 3.7.

3.3.2 Physical property measurement system

The PPMS, as it's name suggests, is a very versatile system to measure various physical phenomena. Here, we will describe the general operation of the cryostat and the magnet, as well as the working principles of using the PPMS for transport measurements. A photo of the setup and a schematic drawing can be found in figure 3.8. The PPMS consists of a nitrogen jacketed dewar. The liquid helium container can hold up to 87 l of helium. This container is then isolated by a vacuum space and additionally cooled by a 48 l container of liquid nitrogen placed above the helium container. All of this is then surrounded by superinsulation.

The PPMS probe that is submerged in the helium consists of a 9-T Nb-Ti superconducting magnet surrounding the well-isolated sample chamber. On the bottom of the sample chamber are a 12-pin connector, where the sample puck (or measurement rods) can be inserted, two thermometers in good thermal contact with the sample puck (one for low temperatures and one for high temperatures), and a heater. The sample chamber has another heater at its neck and is surrounded by a cooling annulus and insulation layers.

The top of the PPMS probe ends in a probe head that sits on top of the dewar. All electrical wiring from the sample chamber leads out to the probe head. Additionally, two helium-fill ports and the ports connecting the helium container, the sample chamber, and the cooling annulus to a vacuum pump are also located here. The sample chamber can be accessed from here by removing the stainless steel flange that covers the opening. This can only be done when the sample chamber is warmed up to room temperature to prevent condensation, when no field is being applied, and when the "vent continuously" mode is on, meaning that the chamber is flushed with helium gas from the helium container to avoid air entering the chamber space. Once the sample chamber is closed again, a couple of cycles of venting with the helium gas and pumping it out must be performed to clean the space from remaining air.

On the bottom of the PPMS probe is the impedance assembly that is directly submerged in the liquid helium.

The operation of the PPMS is controlled by the model 6000 PPMS controller and the model 6700 magnet controller. The MultiVu application is the software application for the controllers.

Temperature control

To cool the sample chamber, liquid helium is pumped into the tubes of an impedance assembly from the helium container at the bottom of the PPMS probe. For temperatures above 4.2 K, the helium is firstly vaporized in the impedance tubes by a heater and only then pumped as a vapor gas into the cooling annulus, which consequently cools down the sample chamber. However, for temperatures below 4.2 K, the cooling annulus is pumped directly with liquid helium. This is the so-called "pot-fill" mode and it can take up to 45 minutes to fill the cooling annulus (and about the same time once it needs to be emptied). Once the annulus is full, the heater connected to the impedance tube heats up, which leads to vaporization of a small amount of liquid helium inside the impedance tube and creation of a bubble that blocks further liquid helium from being pumped inside of the cooling annulus. By pumping, we can then lower the pressure in the cooling annulus, which lowers the liquid heliums boiling point below 4.2 K. Temperatures as low as 1.9 K can be reached in this way.

To raise the temperature of the sample chamber, the heaters at the bottom of the sample chamber and the neck of the chamber are turned on, and the liquid helium from the annulus is vaporized. The impedance tube helium-gas flow is restored. The samples in the sample chamber can achieve temperatures between 1.9 and 400 K (1000 K for VSM with the oven option).

Magnetic field control

For static fields the magnet is switched to a "persistent" mode. In this mode the magnet does not dissipate any energy, as the current is trapped in the SC-wire winding of the magnet that is fully submerged in the liquid helium. Changing of the field requires changing the current flowing in the winding. To do this, the magnet is switched to a "driven" mode. In this mode, the power supply that is in parallel connection to a small portion of the SC winding is turned on, and the current is matched to the one in the SC winding. Then a heater switches the part of the magnets winding that is parallel to the power supply non-superconducting. This forces the current of the SC magnet to flow through the power supply. Now, the current can be switched to a new value, the heater can be turned off, and all of the winding is back to being superconducting. The new current value is now trapped in the winding.

The PPMS probe is equipped with a helium meter. In order to operate the SC magnet the helium level cannot drop below 60%. Otherwise, the magnet is exposed and will quench.

Resistivity option

The resistivity option of the PPMS provides a standard PPMS sample puck, where up to three samples can be connected to pads for a 4-point transport measurement. THE PPMS comes with preexisting hardware and software to perform transport measurements with a 5 mA upper current limit and about 20 nV voltage resolution. Due to the need for larger currents and high resolution, almost all measurements were performed with external hardware. A

6221 Keithley dc and ac current source and a 2182A Keithley 2 channel nanovoltmeter were used.

The highest achievable current of the current source is 105 mA. To protect the samples from burning through, the applied current should be limited by the maximum current density that the sample and wires can pass before melting. Most of the time, there is only a rough estimate to this upper limit as exact calculations are quite difficult. The heat generated by a passing current of a sample of thickness t, given by $Q = I^2Rt$, not only turns into internal thermal energy, but is also lost by radiation to the surroundings. Rough estimate for the maximal current I_{max} can be calculated by setting the heat equal to just the internal thermal energy as follows:

$$I^2Rt = c_p\rho_V Al(T - T_0) \rightarrow I_{max} = \sqrt{\frac{c_p\rho_V A^2(T_m - T_0)}{\rho t}}, \tag{3.2}$$

where c_p is the specific heat, ρ_V is the mass density, A is the cross-sectional area through which the current flows, l is the length, T is the temperature to which the sample heats up, T_0 is the starting temperature and T_m is the melting temperature. We see that the maximal current is highly material dependent (through c_p, ρ_V, and ρ) and decreases with smaller A. Note that as the temperature of the sample increases, the percentage of heat lost to radiation increases. This means that the sample will melt only at currents that are higher than those calculated by this simple approximation.

The nanovoltmeter on channel 1 can achieve a resolution down to 1 nV, on channel 2 to 10 nV.

The measurements can be automated by a program in Python using the Spider development environment written by Sabri Koraltan. From here one can operate the PPMS temperature and magnetic field, set the current, and note the voltage read-outs.

3.3.3 Helium bath cryostat with superconducting solenoid

The second system used for transport measurements was the cryostat by Oxford Instruments. A photo of the setup and a schematic drawing can be found in figure 3.9. The cryostat consists of a vacuum and Mylar sheet-isolated helium dewar that can hold up to 34 l of helium. Submerged in it is another vacuum isolated dewar, the variable temperature insert (VTI). The VTI is surrounded by the solenoid NbTi-Nb_3Sn superconducting magnet. The VTI leads up to an opening at the top of the cryostat system, where one can insert the sample rod. The sample rod ends with a space to glue down a sample and 10 pins to contact to to perform transport measurements. In addition, the sample rod is equipped with a heater and a temperature sensor. The VTI also has its own heater and a temperature sensor. Similarly to the PPMS, for loading and unloading a sample, the VTI has to be warmed up to room temperature and continuously vented by gaseous helium.

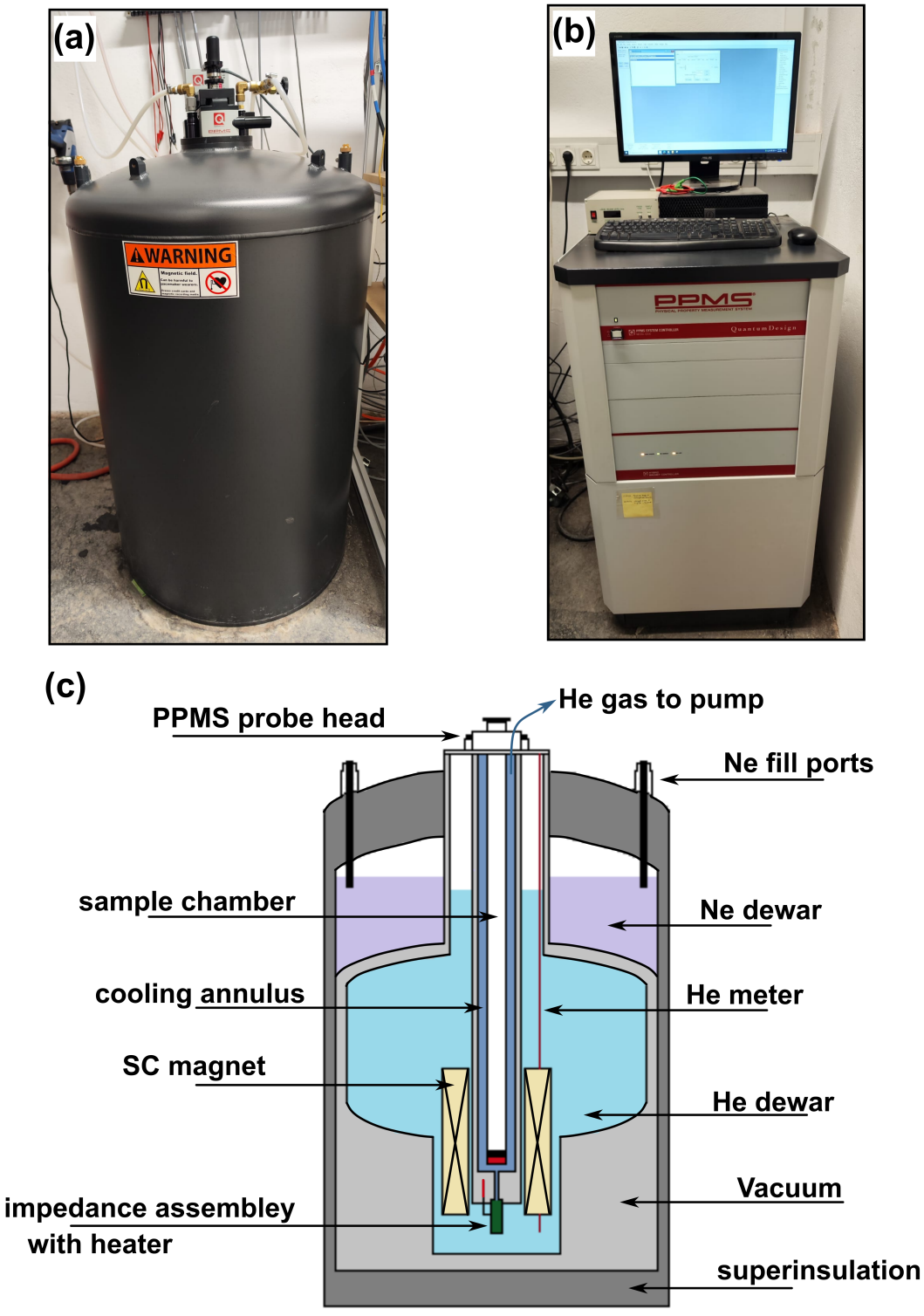

Figure 3.8: A photo of the PPMS cryostat (a) and of the PPMS and magnet controller (b). In (c) is the schematic drawing of the PPMS cryostat. Here, blue represents the liquid helium, purple liquid nitrogen, light gray vacuum isolated space and in red are temperature sensors and heaters. Pictured are only some of the main parts of the cryostat for a better understanding of the setup.

Temperature control

The VTIs main function is to control the temperature of the sample space. An opening of a capillary, connecting the liquid helium dewar and the VTI, can be operated by twisting a needle valve. Through an open capillary, liquid helium is siphoned inside the VTI and can then be pumped out in its gaseous form by a rotary pump placed at the top of the VTI. This allows for cooling of the sample space by evaporation of the helium liquid, followed by cold gas flow around the sample rod. Strong pumping can lower the pressure in the VTI and temperatures below 4.2 K can be reached. The temperature is also regulated by a Lakeshore 336 temperature controller that reads out the values of the temperature sensors placed inside the VTI and at the bottom of the sample rod. Then it can send power through the heaters as needed. The samples inside the Oxford system can reach temperatures between 1.4 and 400 K.

Magnetic field control

The superconducting solenoid can produce magnetic fields up to 13 T when operating at a helium liquid temperature of 4.2 K. The helium dewar is equipped with a lambda plate above the magnet. The lambda plate is connected to a vacuum pump and has a valve that can be opened to suck a small amount of liquid helium inside. The low pressure inside brings the lambda plate liquid helium temperature down, and this in response cools the helium liquid remaining in the dewar. Using the lambda plate assembly, one can operate the magnet below 4.2 K temperatures and reach up to 15 T fields. The magnet is powered by the Oxford PS120-10 power supply. Changing of the field works on the same principle as described for the PPMS.

The helium dewar is equipped with a helium meter. In order to operate the SC magnet the helium level cannot drop below approximately 20%. Otherwise, the magnet could quench. The same can happen if one does not follow the recommended maximum field ramp rates for the system.

Resistivity option

The same external hardware was used as described for the PPMS. All measurements were operated using a computer connected to the devices via a GPIB interface. Using the program written by Bernd Aichner in the programming environment TestPoint, one can control the magnetic field, set the current, and take note of the voltage read-outs.

3.4 Numerical simulations

Numerical simulations in the scope of this thesis were performed using either the TDGL alone or the modified TDGL in conjunction with the heat balance equation.

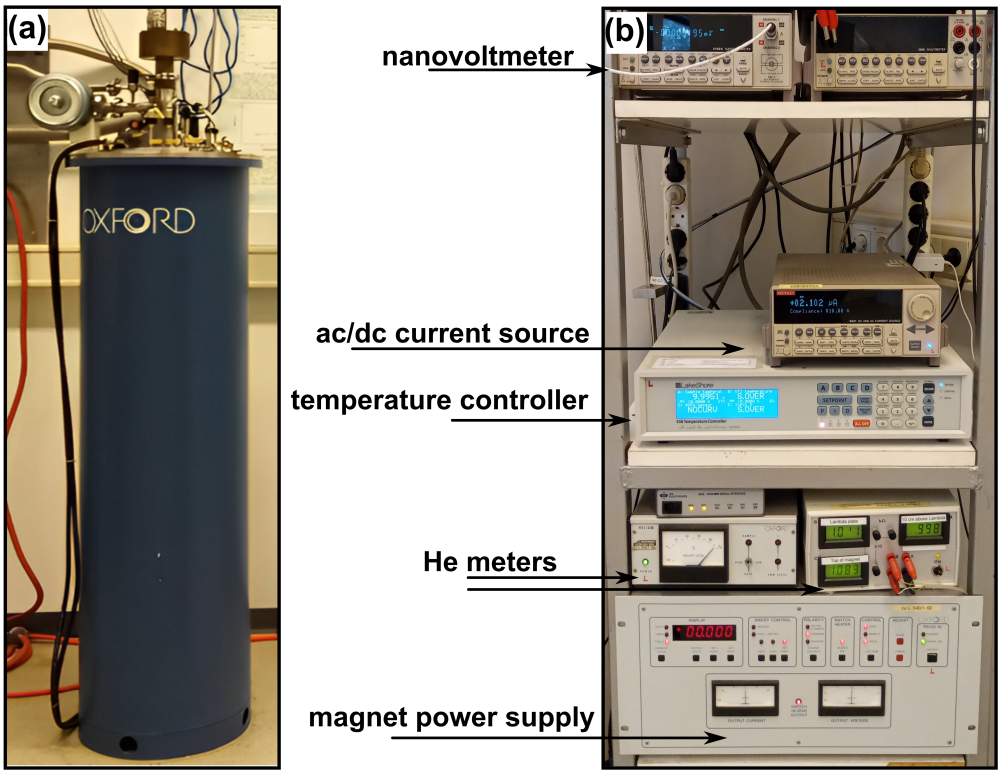

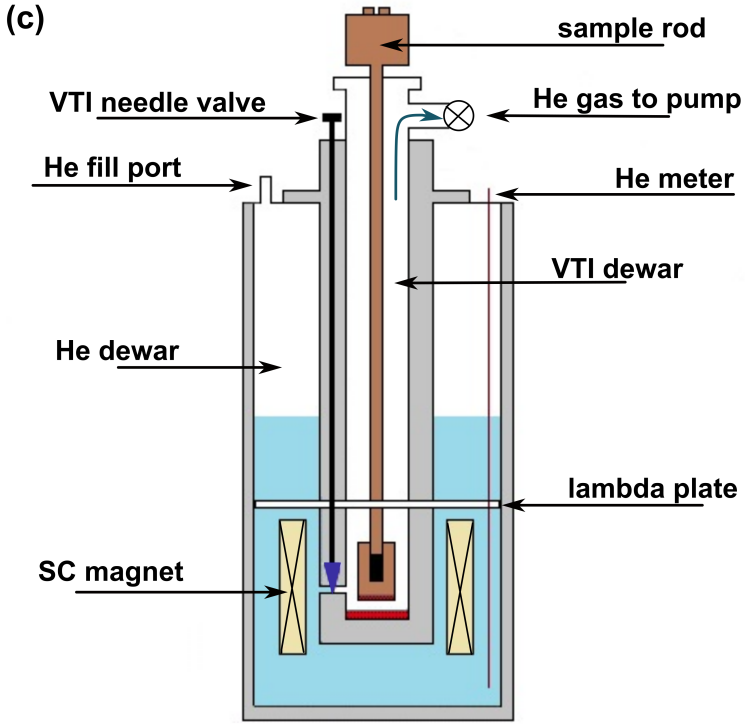

Figure 3.9: A photo of the helium bath cryostat with superconducting solenoid (a) and of the setups devices (b). In (c) is the schematic drawing of the cryostat. Here, blue represents the liquid helium, gray the vacuum isolated space and in red are temperature sensors and heaters. Pictured are only some of the main parts of the cryostat for a better understanding of the setup.

The ordinary TDGL was modeled with link variables to facilitate the preservation of the gauge invariance under discretization. The zero electric potential gauge was chosen. The computational grid is a uniform square grid. As boundary conditions, one uses the condition that the normal component of the supercurrent to the surface must be zero. Defects inside the superconductor are modeled by changing the GL parameter κ. More information on these simulations can be found in the bibliography entry [72].

In the modified TDGL in conjunction with the heat balance equation, Vodolazov modified the ordinary TDGL by introducing the superconducting current defined by the Usadel equations and a finite electron temperature T_e. This allows one to observe non-equalibrium phenomena. The heat balance equation is solved to find T_e as well as the phonon temperature T_p. The boundary condition is again that the normal component of the supercurrent to the surface must be zero. Used are also additional boundary conditions for T_e and the order parameter depending on the edge (along or perpendicular to the current). The simulations are described in more detail in the bibliography entry [29]. The local consideration of temperature in this model uncovers local FFI and local non-equilibrium phenomena.

Chapter 4

Thickness dependencies

The superconducting properties of two materials of various thicknesses are described in this chapter. We study the thickness dependence of amorphous MoSi and of polycrystalline Nb samples. Both of these are in the dirty limit. The reason we chose to work with dirty limit superconductors is that dirty limit electrons need more energy to escape the vortex core and therefore they result in larger v^* and shorter τ_ϵ as compared to clean superconductors [73]. The edge-controlled instability model that we want to test is made for materials where $\tau_{ee} \ll \tau_{ep}$. This is true for dirty limit superconductors.

4.1 Molybdenum silicon

The molybdenum silicon films were prepared on substrates consisting of a Si wafer with a thermally grown 230-nm-thick dielectric SiO_2 layer. The sample was then cosputtered using dc magnetron sputtering (3.1.1) with a molybdenum target and a silicon target. First, a 3 to 5-nm thick Si buffer layer was sputtered. On top of this layer, a MoSi layer was sputtered with the aim of achieving the composition stoichiometry of $Mo_{70}Si_{30}$. Lastly, all was covered with a 3-nm thick Si capping layer. The produced thicknesses of the MoSi layer were 6, 10, 15 and 25 nm. The correctness of the composition stoichiometry was checked by EDX (3.2.2). Cross-section images using TEM (3.2.3) of the cut out vertical lamellas from the sample are given in figure 4.1 a) for a 15-nm thick MoSi sample, where one can clearly distinguish between the various layers of the sample. In figure 4.1 b) the missing ring structure in the SAED (3.2.4) pattern of the film provides evidence of the amorphousness of the film. The AFM (3.2.5) measurements have shown that the roughness of the sample surfaces is less than 0.1 nm.

All MoSi samples characterized in this chapter were cut out for transport measurements using laser beam etching 3.1.2 to bridges of specific width w and length between the voltage contacts l. In figure 4.1 c) is an example of one of the MoSi films laser cut for a 4-point transport measurement and contacted using silver paste and gold wires. All data of the 6, 10 and 15 nm samples were obtained at the Oxford magnet system. Data of the 25 nm sample were taken on the PPMS.

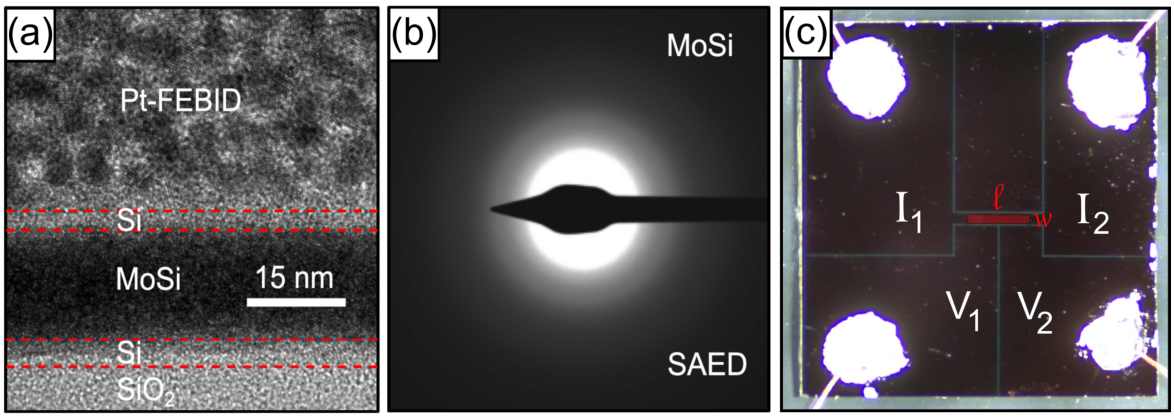

Figure 4.1: MoSi film characterization: Pictured is the TEM image of the vertical cross-section (a), the SAED of the film (b) and the experimental geometry (c) with the sample bridge highlighted in red. The contacts for passing current are I_1 and I_2, and for measuring voltage V_1 and V_2.

4.1.1 Cooling curves and critical temperature

For the basic characterization of the samples, cooling curves were taken for all samples. In the 4-point geometry, voltage was noted for a constant current of 0.1 mA from room temperature down to below T_C temperatures. The voltage is then recalculated to resistivity with $\rho = \frac{V(wd)}{Il}$. The final curves for the thinnest and thickest sample are depicted in figure 4.2 (a). Apart from the clearly visible drop in resistivity at what we define as T_C, we also observe a rise in normal resistivity (for all T>T_C) with decreasing temperature. This transition is called the superconductor-insulator transition (SIT), as opposed to the more frequently seen superconductor-metal transition (SMT), where normal resistivity drops with increasing temperature. SIT is typical for disordered films and is known to be induced by reduced film thickness. The nature of this behavior is not fully understood, but one of the contributors to this behavior is the weak localization of the electrons as a result of quantum interference effects of the electron waves in disordered electron systems [74, 75]. This weak localization leads to corrections to resistivity due to superconducting phase fluctuations [76–78] and/or increase in the Coulomb interaction [79]. Our MoSi samples, as proven through previously mentioned measurements, are amorphous, which already on its own makes them disordered systems. The further suppression of thickness of the films causes increased surface scattering, and hence lowers their electron mean free path, which increases their effective disorder. It is clearly seen in figure 4.2 (a) that the width of the SIT transition is larger for the thinner sample, which supports the previously mentioned theories that SIT is more pronounced for systems with higher disorder. The calculated residual resistivity ratio RRR, defined here as the ratio between resistivity at 300 K and 10 K, falls from 0.95 to 0.87 for the 25 nm and the 6 nm sample, respectively. A better representative of the SIT growth is the width between resistivity at 300 K and 10 K, ΔR. The results for all thicknesses can be

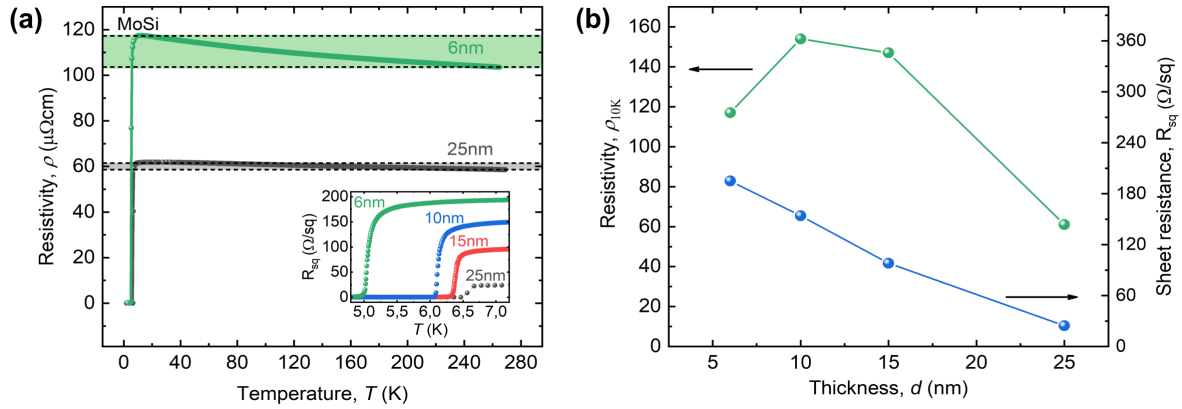

Figure 4.2: MoSi cooling curves: Resistive curves taken for temperatures from 260 down to 3 K for the thinnest (6 nm) and thickest (25 nm) studied MoSi sample (a). Highlighted area shows the raise in resistivity between 260 and 10 K. The inset shows the sheet resistance curves. Further is plotted the sheet resistance and resistivity at 10 K for all thicknesses (b).

found in the table 4.1.

The sheet resistance R_{sq} above the transition, as seen in the inset of figure 4.2 (a) and in (b), increases with decreasing thickness. In MoSi, we are dealing with a metallic amorphous system, but much can be learned from previous studies done on pure metals or metallic multilayered structures [80–83]. In these studies it is shown that there exits a range of thickness with $\rho \propto d^{-1}$. Considering that the normal state resistivity, as defined in the Drude model, is also proportional to l^{-1}, the implication is that the mean free path l is limited by the thickness of the layer. As mentioned above, this can be simply understood as an increase in the scattering from the surface, hence the decrease of l, as the thickness is lowered. ρ saturates for large d in ρ of the bulk material, and for very small d to $\rho(l \simeq a_0)$,where a_0 is the interatomic spacing. The latter follows from the Ioffe-Regel rule [84]. The rule limits the value of l to equal and above the values of a_0, because smaller values do not allow for metallic transport.

Although all of this gives a good general insight into the topic, the enhancement of R_{sq} as well as the change in other superconducting properties in amorphous films are much more complicated. It should also be noted that in our results ρ did not show a linear behavior with thickness as described in the mentioned theories, but instead has a peak at 10 nm (figure 4.2(b)). Only R_{sq} increases monotonically with decreasing thickness. Several models were developed to link R_{sq} with d, but also to T_C. Hence, let us first look at the development of T_C with thickness.

Figure 4.3(a) shows the resistivity normalized by its value at 10 K for temperatures in the vicinity of the transition for all sample thicknesses. The vertical lines point to the critical temperatures T_C. These are chosen as the point where the 0.75 horizontal line intersects the

cooling curve, known as the 75% criterion. The intersections of the 0.1 and 0.9 horizontal lines with the cooling curve line-out the width of the SC transition ΔT_C. The SC transition width is here pictured for the 6 nm sample as the green highlighted area. We detect a decrease of T_C and an increase in ΔT_C with decreasing sample thickness d. This is summarized in figure 4.3 (b).

The decrease in T_C is also observed in experiments in which the samples are increasingly irradiated with higher fluence [85, 86]. Here, researchers link this decrease with the decrease in the long-range order parameter S due to defects that are introduced into the lattice by irradiation [87]. This suggests that systems with higher disorder will have lower T_C. This is in alignment with the previously mentioned hypothesis that lower thickness accounts for higher effective disorder and thus we observe T_C decrease. In addition, we can compare the broadening of ΔT_C with fluence in irradiation experiments [88], with the broadening of ΔT_C we observe with decreasing thickness. In irradiation experiments this behavior is explained as the creation of microregions with different T_C from the matrix. Similar conclusions have been derived for amorphous films. Researchers found that in SC amorphous thin films superconducting phase fluctuations in homogeneous disorder can create regions with superconducting islands immersed into a normal/metallic matrix around the transition [89–91]. This means that in the surroundings of the critical temperature region there exists a spatially inhomogeneous superconducting state in homogeneously disordered systems. As the temperature decreases, the density of these islands increases. This allows proximity-induced coupling between them, and eventually a full superconducting state is reached [92, 93].

For the shape of the T_C-d curve is known, it has a very slow to no decrease in thick films. Here, T_C can be considered constant and equal to T_B, the bulk critical temperature. Then, starting from a certain thickness, a decrease in T_C starts to be more and more pronounced as proximity-coupled SC islands appear in the critical temperature region.

For the analytical description of the T_C-d curve, Simonin derived an equation by inserting a surface energy term into the Ginzburg-Landau equation [94]. The resulting dependence goes as follows:

$$T_C = T_B(1 - \frac{d}{d_c}), \tag{4.1}$$

where d_c is a fitting parameter that represents the thickness bellow which superconducting properties will disappear. In figure 4.3 (b) the dotted curve is the Simonin fit to our data. Both T_B and d_c are taken as fit parameters. We observe that the data point for the 6 nm sample deviates from the curve that fits the data points of the other thicknesses. The 6 nm sample is also the one that showed a rather unexpected decrease in ρ. The possible reason for the unexpected behavior will be addressed in a later part.

The fitted $T_B =$ is 6.93 K. This is in fairly good agreement with the literature where for a 200 nm thick MoSi sample, with the same composition as ours, a T_C of 6.6 K was reported [95]. The offset from the literature value can perhaps be due to the usage of a different criterion (such as the 75% we used) to determine T_C. The second parameter d_c with a value of 1.06 nm is also in a rather good agreement with recent studies on MoSi thin films, where

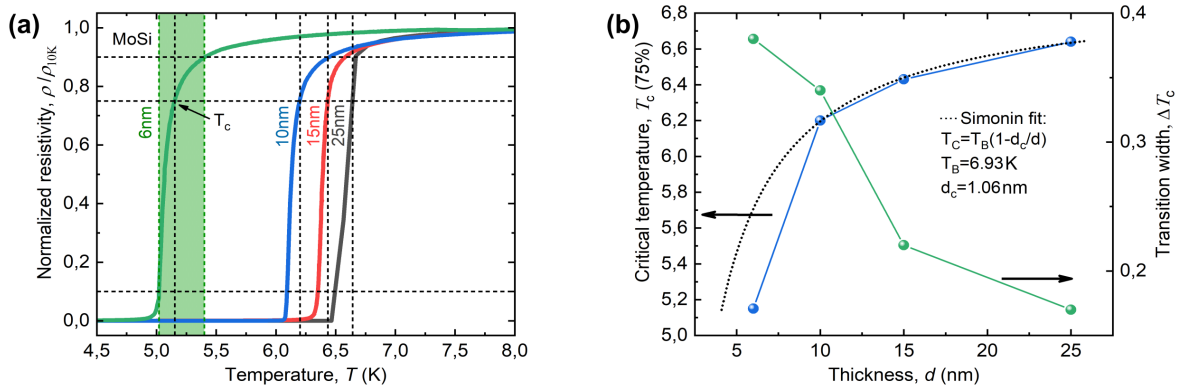

Figure 4.3: MoSi critical temperature: Superconducting transitions for all studied MoSi samples presented as the disappearance of the normalized resistivity (a). The vertical dashed lines point to the individual critical temperatures T_C. Highlighted green area represents ΔT_C for the 6 nm sample. All values of ΔT_C and T_C are plotted against their thickness in (b). The dashed line is the Simonin fit to the T_C curve.

a d_c of 1.46 nm was reported [96]. In these studies, MoSi had a stoichiometry of 83-17, in contrast to our 70-30.

Simonin law was not specifically developed for amorphous films, but rather to describe the T_C evolution with thickness for any superconducting thin films. To specifically address the case of amorphous films, Finkel'stein developed a model modifying the BCS equation to take into account the change in Coulomb interactions due to homogeneous disorder. He observed that T_C scales better with R_{sq} than it does with thickness. The relationship between T_C and R_{sq} is as follows:

$$T_C = T_B e^{\gamma} \left[\frac{\left(\frac{1}{\gamma} + \frac{r}{4} - \sqrt{\frac{r}{2}}\right)}{\left(\frac{1}{\gamma} + \frac{r}{4} + \sqrt{\frac{r}{2}}\right)} \right]^{\frac{1}{\sqrt{2r}}}, \tag{4.2}$$

where γ is the fitting parameter and :

$$r = \frac{e^2}{2\pi^2\hbar} R_{sq}. \tag{4.3}$$

The result of the fit to the data is in figure 4.4 (a). Again, no god fit was found to include the data of the 6 nm sample. As a result of the fitting we obtained a T_B of 6.75 K, not far from what we derived with the Simonin law, and a γ of 6.9. This is in the order of values for other homogeneously disordered materials like TiN with γ between 6.8 and 6.2 [90], MoGe with $\gamma = 8.2$ [97], or even MoSi (83-13 stoichiometry) with $\gamma = 7.66$ [96].

For the 6 nm sample that seems to be misaligned compared to the rest of the taken data points, we can only draw some assumptions. From the data we gathered, if we assume that the fitting models are correct, it seems that the sample is actually thinner and has a lower

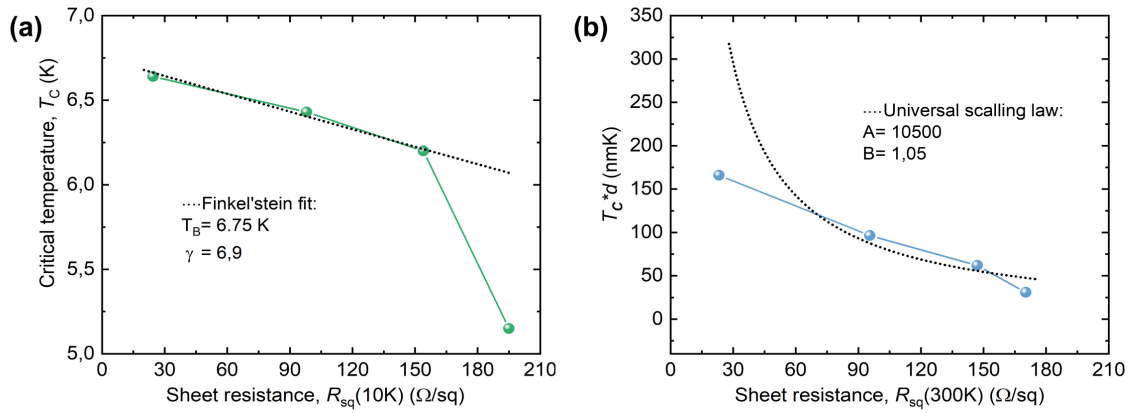

Figure 4.4: MoSi fitting models for R_{sq} and T_C: Dashed lines are fits to the Finkel'stein model (a) and Universal scaling law (b)

Si content than what we thought. Whilst a thinner sample accounts for the lower T_C we observed, a stoichiometry deviating from 70-30 to one with a higher Mo and lower Si content accounts for the lower ρ we observed. The Finkel'stein fit to include the 6 nm data point has a higher T_B and a higher γ than the one fitted for the rest. Once again a lower Si content MoSi has a higher T_B and as we see in ref. [96] also higher γ. This again supports our assumptions.

This stoichiometry and thickness change in the 6 nm sample could have happened if some of the Si from the MoSi layer stuck to the Si buffer and/or capping layer, effectively lowering the thickness and Si content of the MoSi layer. In thicker samples this might have been also the case, but because of the larger thickness, the stoichiometry in the middle of the sample stayed as desired and the change in thickness was negligible. In the cross-sectional TEM figure 4.1 (a) one can actually observe how the Si (lighter dots) at the edges of the MoSi layer is more concentrated.

Lastly, we tried to fit the data with the Universal scaling law developed by Ivry *et al.*[98]. The proposed scaling law is suggested to fit the data better and reduce scatter compared to the previously fitted models by linking T_C to both R_S and d. The scaling law is the following power law:

$$dT_C = AR_{sq}^{-B}, \tag{4.4}$$

where A and B are fitting parameters. For amorphous films B should be larger than 1. Despite the great success of the law to fit an extremely large library of data of different materials and thicknesses, it has failed to fit our data as seen in figure 4.4 (b).

All findings of this subsection are summarized in table 4.1. The energy gap $\Delta(0)$ for all samples is also included, estimated by equation 2.1.

d [nm]	w [μm]	l [μm]	T_C [K]	ΔT_C [K]	ρ_{10K} [$\mu\Omega$cm]	R_{sq}(10K) [Ω/sq]	R_{sq}(300K) [Ω/sq]	ΔR [$\mu\Omega$cm]	RRR	$\Delta(0)$ [μeV]
6	200	1000	5.15	0.38	117	195	170.3	24.7	0.87	781.06
10	200	1000	6.2	0.34	154	154	147	7	0.95	940.28
15	182	616	6.43	0.22	147	98	95.5	2.5	0.97	985.78
25	200	1000	6.64	0.17	61	24.4	23.2	1.2	0.95	1007

Table 4.1: MoSi critical temperature and resistivity summary. The table consists of results for the sample width w, voltage contact length l, critical temperature T_C, transition width ΔT_C, normal resistivity at 10 K ρ_{10K}, square resistance at 10 K and 300 K R_{sq}(10 K) and R_{sq}(300 K), width of the resistivity raise ΔR, residual resistivity ratio RRR and the energy gap $\Delta(0)$.

4.1.2 Upper critical field

Figure 4.5 depicts the normalized resistive curves measured from no applied magnetic field and then up to magnetic fields where no transition is anymore visible, or up to the highest magnetic field achievable by the setup. These measurements are shown for the 6 nm (a), 10 nm (b), and 25 nm (c) samples. The 15 nm sample results are found in the following chapter, figure 5.2. We note that the broadening of the transition with an increasing field is more pronounced in the thinner samples. This again hints at the presence of an inhomogeneous superconducting state in the thinner samples. The intersections with the dashed horizontal line at 0.75 give the value of T_C at the curves corresponding applied field. In figure 4.5 (d) the result of this analysis, the upper critical field B_{C2} versus temperature, is plotted for all thicknesses.

To obtain B_{C2} for T=0, one must perform a fit procedure to the measured data. Since in high magnetic fields superconductivity can be destroyed due to orbital pair breaking and/or the action of the spin-paramagnetic effect, the upper critical field $B_{C2}(0)$ is limited by these effects. Whilst the orbital pair breaking happens as aftermath of the Lorentz force acting on paired electrons, spin-paramagnetic effect breaks superconductivity as a result of Zeeman splitting when the Pauli-paramagnetism energy is equal to the superconducting condensation energy. Werthamer, Helfand and Hohenberg (WHH) derived a description for the temperature dependence of B_{C2} from the Gor'kov theory taking into account the effects of the orbital and spin-paramagnetic effect, and also spin-orbital scattering [99]. The WHH equation is expressed as:

$$ln\frac{1}{t} = \left(\frac{1}{2}+\frac{i\lambda_{so}}{4\gamma}\right)\psi\left(\frac{1}{2}+\frac{\overline{h}+\lambda_{so}/2+i\gamma}{2t}\right)+\left(\frac{1}{2}+\frac{i\lambda_{so}}{4\gamma}\right)\psi\left(\frac{1}{2}+\frac{\overline{h}+\lambda_{so}/2-i\gamma}{2t}\right)-\psi\left(\frac{1}{2}\right)$$
$$\text{with } t=\frac{T}{T_C};\quad \overline{h}=\frac{4B_{C2}(0)}{\pi^2(-dB_{C2}/dT)_{t=1}};\quad \gamma=\left[(\alpha\overline{h})^2-(\lambda_{so}/2)^2\right]^{1/2}. \tag{4.5}$$

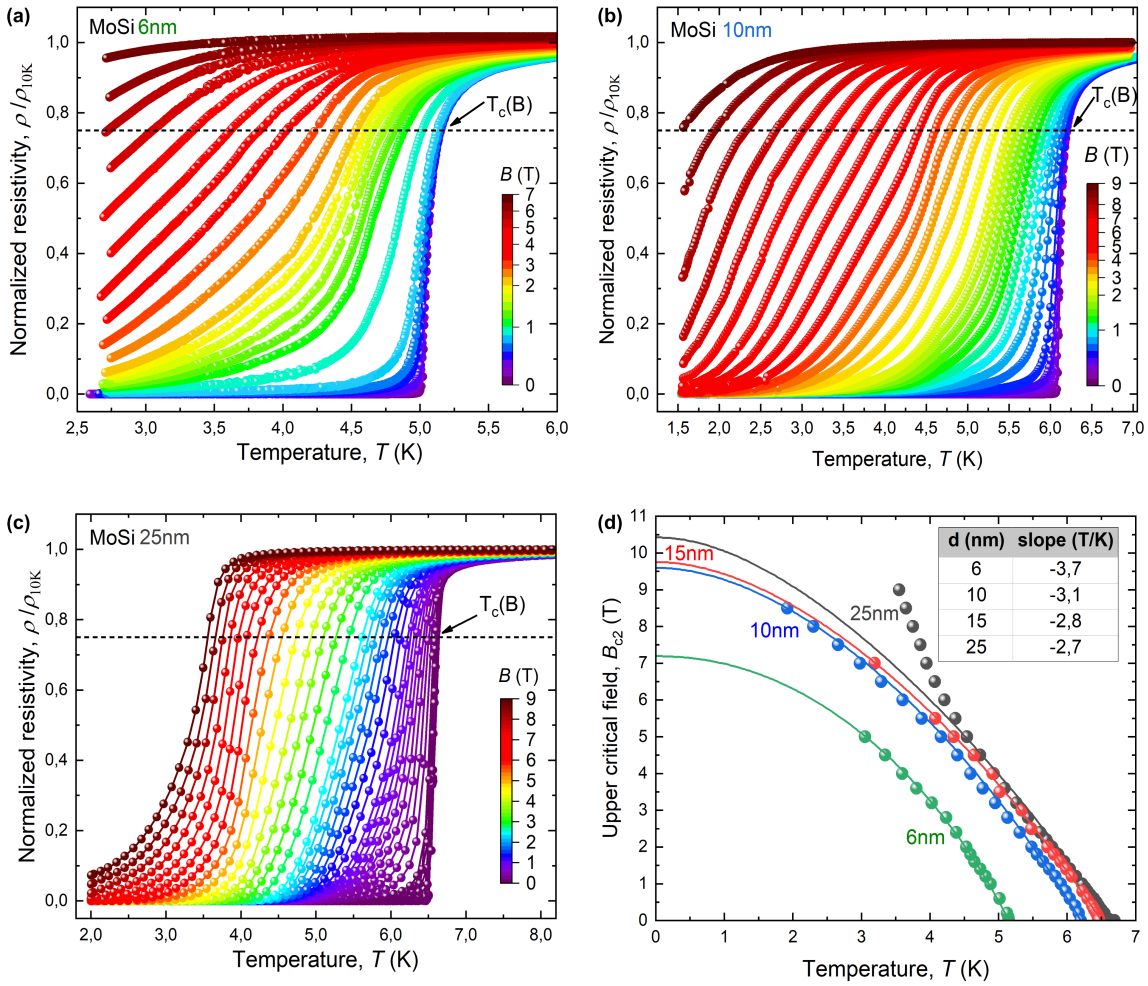

Figure 4.5: MoSi upper critical field: Normalized resistive curves taken at various magnetic fields for a MoSi 6 nm- (a), 10 nm- (b) and 25 nm-thick (c) film. The dashed line represents the 75% criterion at which values for the upper critical field were taken from. In (d) the resulting upper critical field are plotted against temperature. The solid line is a fit to the WHH equation.

Here, λ_{so} is the spin-orbit scattering constant, α is the Maki parameter, and $\psi(x)$ is the digamma function.

When λ_{so} and α are equal to zero, $B_{C2}(0)$ is the same as the orbital limiting field $B_{orb}(0)$. In the presence of the spin-paramagnetic effect $B_{C2}(0)$ is reduced due to the existence of a paramagnetically limited field $B_P(0)$. $B_{C2}(0)$ has then values bellow $B_{orb}(0)$. The ratio expressing the contribution of the two limiting fields $B_{orb}(0)$ and $B_P(0)$ to the final $B_{C2}(0)$ is given by the Maki parameter α, where

$$\alpha = \sqrt{2}B_{orb}(0)/B_P(0). \tag{4.6}$$

In samples where spin-orbit scattering is strong ($\lambda_{so} > 0$), electron spins can be randomized. This weakens the effect of the spin-paramagnetic limiting.

The fittings to the WHH equation 4.5 can be seen as the solid lines in figure 4.5 (d). The used slope (dB_{C2}/dT) in the equation for all samples was taken in the vicinity of T_C and can be found in the table in figure 4.5 (d). The WHH equation describes the data quite well for the 6, 10 and 15 nm sample. The 25 nm sample showed a rather unexpected temperature development with a sharp increase in upper critical fields below 4 K. Since this behavior has previously not been observed in any MoSi measurements, we suspect that the high fields might have dislodged a corner of the sample from the holder and thus the angle between the external magnetic field B and the sample area A was differentiating from the original 90°. In figure 4.6 (a) we compare upper critical field curves for the 15 nm sample at a 90 and 0° angle. We conclude that an angle smaller than 90° would indeed lead to observing the measured positive upturn in the upper critical field. Remeasurement of the 25 nm sample at high fields is needed, but for the current purpose the WHH equation 4.5 for the 25 nm sample was made only for the low field data.

The fitted parameters λ_{so} and α can be found in figure 4.6 (b). Here we also find $B_{C2}(0)$ taken from the WHH fitted curves at 0K. The plotted orbital limiting field B_{orb} is calculated using equation

$$B_{orb}(0) = -0.693(dB_{C2}/dT)_{T=T_C}T_C. \tag{4.7}$$

This equation is derived from the WHH equation for λ_{so} and α equal zero and can be rewritten as $B_{orb}(0) = 0.693B_{C2}(T)[1-(T/T_C)]^{(-1)}$. In this form we see that apart from the 0.693 prefactor, it is consistent with the Maki and de Gennes (MDG) microscopic description for the temperature dependence of B_{C2} in the dirty limit ($l \ll \xi(0)$) [100, 101].

Lastly, the paramagnetically limited field B_P plotted in figure 4.6 (b) is calculated using equation 4.6.

The parameter α is highest for the thinnest sample and is reduced as the thickness increases. This means that the Pauli limiting field is very large for thick samples and bulk MoSi samples. In these samples, $B_{C2}(0)$ is only limited by the orbital field. Based on our results, where the Pauli limiting field is even lower than the orbital limiting field, we can conclude that spin-paramagnetism and spin-orbit scattering should be taken into account for thin films, as they have influence on the final appearance of the curve $B_{C2}(0)$. We observe

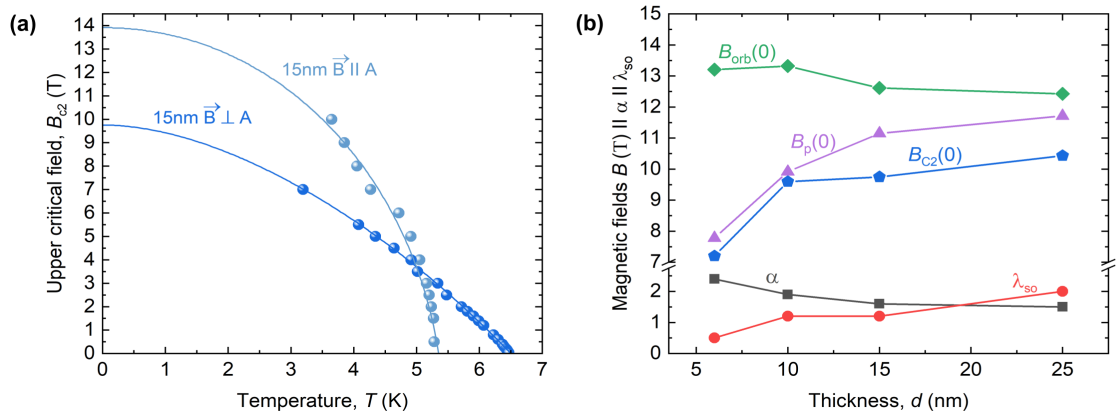

Figure 4.6: MoSi WHH fitting: In panel (a) is the comparison of upper critical field curves for the 15 nm sample at an external field that is perpendicular (dark blue) and parallel (light blue) to the surface. Solid lines are fits to WHH equation. In panel (b) we see the WHH fitted parameters λ_{so} and α, and all the limiting fields at 0K.

that the $B_P(0)$ curve resembles that of the T_C dependence on d. This is in line with the origin of the Pauli limiting upper critical field that limits superconductivity when the Pauli paramagnetism energy G_P is equal to the superconducting condensation energy G_C. The Pauli limiting field is then calculated as:

$$G_P = G_C$$
$$\frac{1}{4}(g\mu_B)^2 N(0) B_P^2 = \frac{1}{2} N(0) \Delta_0^2$$
$$B_P = \frac{\sqrt{2}\Delta_0}{g\mu_B} \approx \frac{\sqrt{2}\ 1.76 k_B T_C}{g\mu_B} \approx 1.86 T_C, \tag{4.8}$$

where g is an electron g-factor, μ_B is the Bohr magnetron, $N(0)$ is the density of states at the Fermi level, and Δ_0 is the superconducting gap that is $\approx 1.76 k_B T_C$.

B_{orb} can be derived from the Ginzburg-Landau-Abrikosov-Gor'kov (GLAG) theory as $B_{orb} = \kappa\sqrt{2} B_C$ [102]. In the dirty limit Gor'kov Goodman derived $\kappa = \kappa_B + C_1\sqrt{\gamma}\rho$, where κ_B is the bulk value of the Ginzburg-Landau parameter, γ is the Sommerfeld coefficient, and C_1 is a constant [103]. GLAG theory further defines $B_C = C_2 T_C \left(1 - \frac{T}{T_C}\right)\sqrt{\gamma}$ with a C_2 constant. Combining all gives us the orbital upper critical field in the dirty limit as defined by GLAG theory:

$$B_{orb} = C_3 T_C \left(1 - \frac{T}{T_C}\right) \gamma\rho, \tag{4.9}$$

where C_3 is a constant. From this equation we can understand the shape of the $B_{orb}(0)$ curve in figure 4.6 (b). As the thickness of the samples is reduced the slight decrease in

T_C is compensated by ρ growth, hence we observe only a slow increase of $B_{orb}(0)$. At very low thicknesses the sharp T_C decrease then overpowers the ρ contribution to $B_{orb}(0)$ and we observe a decrease in the parameter. A further decrease in the field is expected for even thinner samples. This is in agreement with a previous result found in amorphous ultrathin films of Niobium [91]. The final $B_{C2}(0)$ is then resulting from the combination of the two limiting fields.

d [nm]	dB_{C2}/dT [T/K]	B_{orb} [T]	B_{C2} [T]	WHH α	WHH λ_{so}	B_p [T]	D [cm^2/s]	ξ_0 [nm]	λ_L [nm]	Λ [μm]
6	-3.7	13.21	7.2	2.4	0.5	7.78	0.296	4.998	499.517	83.173
10	-3.1	13.32	9.6	1.9	1.2	9.91	0.354	4.977	522.307	54.56
15	-2.8	12.61	9.74	1.6	1.2	11.15	0.392	5.115	498.383	33.118
25	-2.7	12.42	10.43	1.5	2	11.71	0.406	5.153	317.645	8.072

Table 4.2: MoSi upper critical fields summary: Table contains results for the slope, orbital limiting field B_{orb}, upper critical field B_{C2}, Maki parameter α, spin orbit scattering constant λ_{so}, Pauli limiting field B_p, diffusion constant D, coherence length ξ_0, penetration depth λ_L and Pearl length Λ.

All results of this subsection are summarized in table 4.2. Included are also results for the diffusion constant D (eq. 2.5), the coherence length ξ_0 (eq. 2.3), the penetration depth λ_L (eq. 2.4) and the Pearl length Λ. Pearl length is calculated from

$$\Lambda = 2\lambda_L^2/d \tag{4.10}$$

and its results categories all of our samples as wide strips for which $w > \Lambda$.

4.1.3 Critical current and current-voltage curves

Figure 4.7 (a) shows an I-V measurement for the 10nm sample at 5.0K temperature chosen at random. However, the behaviors to be described are found in all samples and at all temperatures. The logarithmic representation allows one to see all regions of the I-V curve as described in the subsection 2.2.3. Each section is labeled in the figure with the corresponding section number. The nonlinear section III. is very subtle to non-existent, because the FFI jumps occur already in the linear regime. The pinned region I. with a constant very low voltage ends in the depinning current I_C^*. Because it is usually difficult to observe this regime change, due to oscillations or complete absence of the pinned regime, one uses a voltage criterion to define a critical current I_C. The criterion is seen as the dashed horizontal line in figure 4.7 (a). Where ever the I-V curve crosses the dashed line is where we set the critical current I_C. We have chosen a voltage of 0.5 mV as the voltage criterion. This might seem quite high and is clearly positioned high into the linear flux-flow regime, but we have chosen this criterion to later be able to define the critical current for all applied magnetic fields

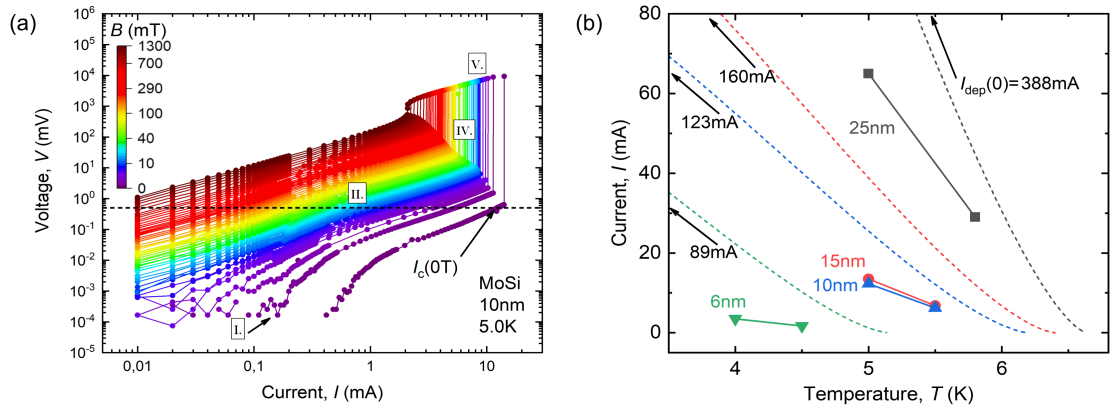

Figure 4.7: Shown are the MoSi I-V curves for the 10 nm sample in 5.0 K temperature in logarithmic scale (a). They are measured at external magnetic fields that correspond to the color code in the scale bar. The vertical line at 0.5 mV is the criterion for the defined critical current $I_C(0)$ plotted in (b) for all sample thicknesses. Whilst symbols are measurement data points, solid lines are the pair-breaking currents. The matching colors represent the same thickness.

without having to interpolate many curves. In this chapter, we were only interested in the zero magnetic field $I_C(0T)$, crossing with the most right curve. The results for all sample thicknesses and measured temperatures are found in figure 4.7 (b). Data points for the 25 nm sample are interpolated from lower currents. To protect the samples from burning, we have not measured using currents above 20 mA. We observe that the thinner the sample, the lower I_C it has. We assume that this is a consequence of a smaller number of pinning centers present in a thinner sample that can pin down vortices. Vortices will be present in the sample even at zero applied magnetic field due to the field created by currents flowing through the sample. We also compare our results to the theoretically highest achievable pair-breaking current defined for dirty superconductors at zero magnetic field by Romijn et al. [40] as follows:

$$I_{dep} = I_{dep}(0)\left[1 - \left(\frac{T}{T_C}\right)^2\right]^{3/2} \tag{4.11}$$

with the zero Kelvin $I_{dep}(0)$ calculated as [104]:

$$I_{dep}(0) = 0.74\frac{w[\Delta(0)]^{3/2}}{e_0 R_{sq}\sqrt{\hbar D}}\frac{1}{\sqrt{1 + w/(\pi\Lambda)}}. \tag{4.12}$$

The factor $1/\sqrt{1 + w/(\pi\Lambda)}$ must be included for wide strips, like ours, to take into account the non-uniformly distributed current throughout the width of the sample. The resulting curves can be found as the dashed lines in figure 4.7 (b). Matching colors correlate the calculated pair-breaking current with the measurement data of the same thickness. We observe the

same thickness dependence and similar temperature dependence. We also observe that the 25 nm sample is in a not yet normal state, but in a high resistive state (corresponding to 0.5 mV), already at about 60% of the theoretical I_{dep}. The 15 and 10 nm samples reach the high resistive state with 30-50% of I_{dep}, and the 6 nm sample is already highly resistive at about 16% of I_{dep}. Again we attribute the reaching of the higher resistive state at a smaller percentage of I_{dep} in the 6 nm sample to a lower number of pinning centers. But, as for all sample thicknesses, I_C is not reaching high enough values that would be of interest for applications. The following chapter introduces an idea how to alter these samples to push the I_C values closer to the theoretically predicted values. The table 4.3 contains the results for I_C and $I_{dep}(0)$.

In figure 4.8 are the I-V curves in linear scale for the 6 (a,b), 10 (c,d), 15(e,f) and 25 nm (g,h) sample. The panels on the left side are taken at about 88% of T_C and the panels on the right at about 78%. They are measured at external magnetic fields that correspond to the color code in the scale bar. Straight vertical lines correspond to region IV., the FFI region, from subsection 2.2.3. For each curve, we take note of the voltage V^* and current I^*, where the FFI raises from. An example of this procedure is given in figure 4.8 (g) by the black arrows. For the thickest sample in figure 4.8 (g,h), the I-V curves for low magnetic fields do not end in FFI jumps. This is because we have limited the highest applied currents to 20 mA to protect the samples from burning, and the jumps for these low fields only occur at currents above this security limit.

4.1.4 Critical velocity

Once we have collected the data we can calculate the critical velocity v^* as introduced in subsection 2.3.2 with $v^* = V^*/Bl$. The results are plotted in figure 4.9. As described in subsection 2.3.2, we use various models to obtain information about energy relaxation time τ_ϵ.

LO and DO models

The first model to be fitted is the LO model. LO predicted v^* to be constant in all external magnetic fields B. Hence we set v^* to a single value by fitting a horizontal line to the data at higher magnetic fields. Setting this value into equation 2.12 gives the result for τ_ϵ as defined by LO. The results for two temperatures and all samples can be found in figure 4.9 (a,b). From this analysis we conclude that τ_ϵ increases with thickness and has values raging from 76 to 412 ps when the temperature is at about 88% of T_C and from 149 to 1358 ps at about 78%. τ_ϵ also raises with dropping temperature. In the LO model $\tau_\epsilon \simeq \tau_{ep}$. A drop in temperature causes fewer electron-phonon interactions and hence explains the higher τ_ϵ. Many effects like contributions of τ_{ee} to τ_ϵ, effects of self-heating, or the dependence of v^* on field at low magnetic fields are left out from the LO model. This suggests that the results of this model might be far from the real value of τ_ϵ. To address the magnetic field dependency we have tried to fit the DO model that takes this into account. The data were fitted to

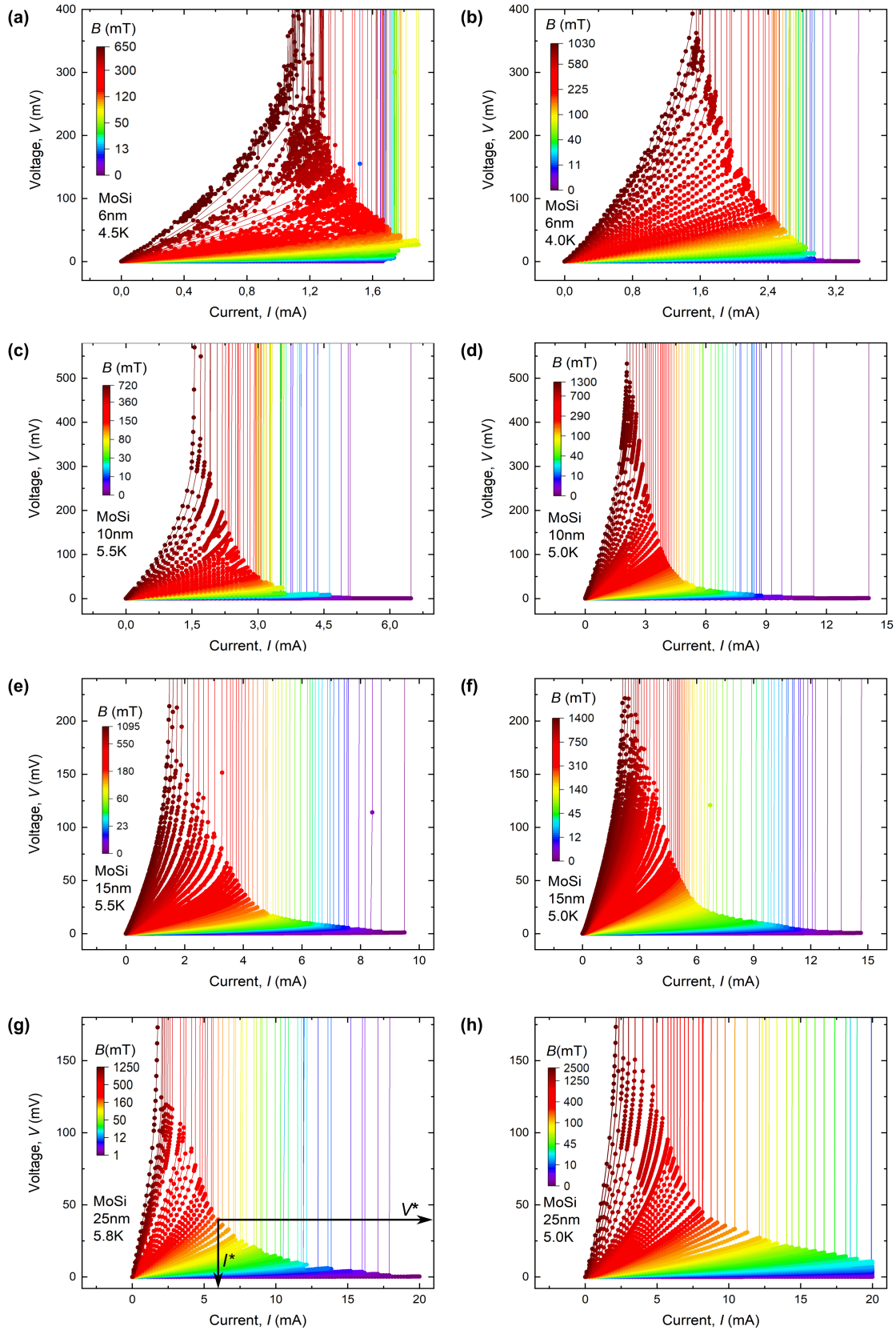

Figure 4.8: MoSi I-V curves for the 6 (a,b), 10 (c,d), 15 (e,f) and 25 nm (g,h) samples. They are measured at external magnetic fields corresponding to the color code in the scale bar. Panels on the left side are taken at about 88% of T_C and on the right at about 78%.

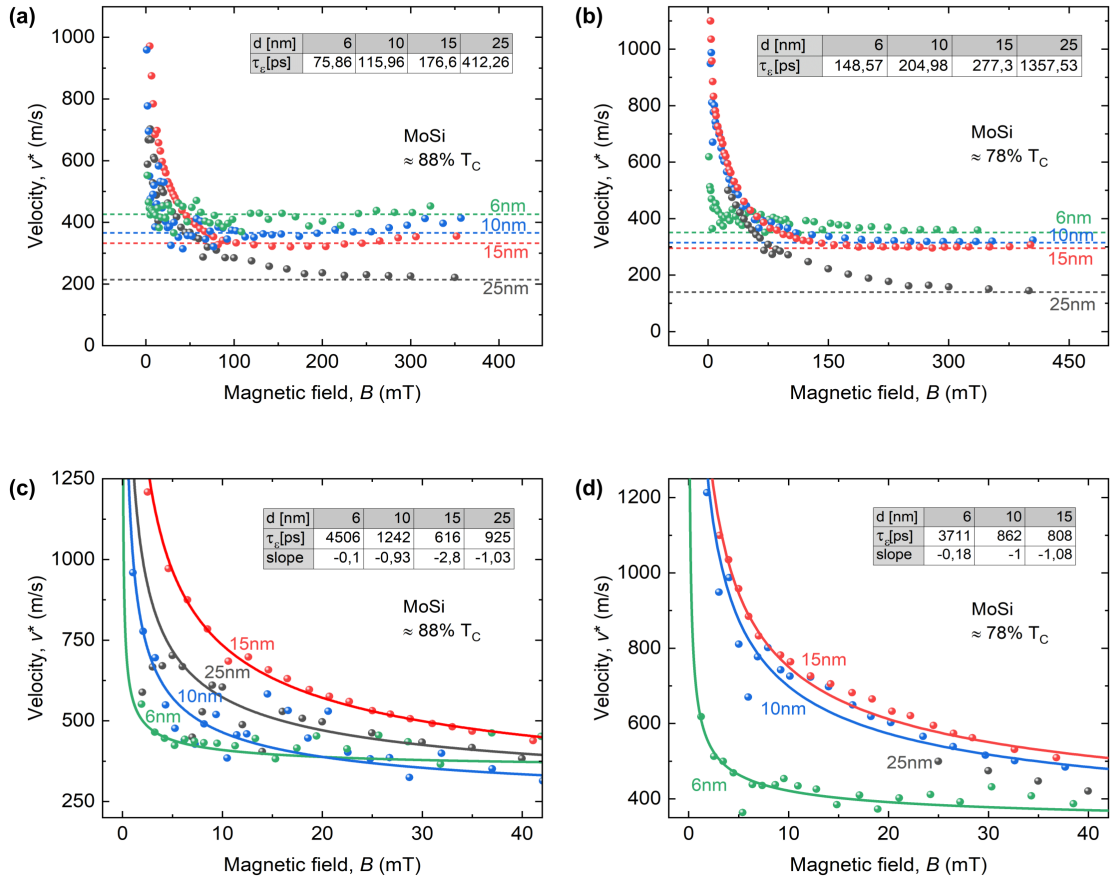

Figure 4.9: MoSi maximal velocity v^* for all thicknesses fitted by LO model (a,b) and by DO model (c,d). Panels on the left side are taken at about 88% of T_C and on the right at about 78%. Symbols are measured data, solid lines are fitting curves. Resulting fitting parameters are given in the tables included in each panel.

equation 2.22 from the DO model. Since this models uniqueness comes from being able to fit the low magnetic field data, we have concentrated on fitting the data at only low magnetic fields. Fitting the entire magnetic field range was not possible, as good fits at low magnetic fields result in very bad fits at high magnetic fields. Furthermore, in addition to τ_ϵ, we had to leave the parameter of slope, present in the equation in the definition of the parameter D, as a free parameter. The resulting curves and the fitted parameters are found in figure 4.9 (c,d). No curve is fitted to the 78% T_C 25 nm data because of the lack of data points for low magnetic fields as a consequence of the security current limit mentioned. The slope fitted values are much lower than previously found from the B_{C2} measurements (compare with the values in table 4.2) and suggest a not observed rash increase in B_{C2} in the vicinity of T_C. Further, the dependency to thickness is flipped compared to before and is mostly raising with thickness. The same goes for the resulting τ_ϵ that is now shortening with thickness and dropping temperature in contrast to the results of the LO model. All of this suggests that the DO model fails to represent the data correctly in low magnetic fields and the resulting τ_ϵ, with values between 800 to 4500 ps, is incorrect. All the fitted parameters of the LO and DO model can be found in table 4.3 and the resulting τ_ϵ for both models in table 4.5.

MoSi		(≈78% T_C)			(≈88% T_C)		
d [nm]	$I_{dep}(0)$ [mA]	I_C [mA]	v^*_{LO} [m/s]	$(dB_{C2}/dT)_{DO}$ [T/K]	I_C [mA]	v^*_{LO} [m/s]	$(dB_{C2}/dT)_{DO}$ [T/K]
6	89.27	3.5	351	-0.18	1.68	425.9	-0.1
10	123.37	12.29	315	-1	6.2	366	-0.93
15	159.78	13.47	295	-1.08	6.8	332	-2.8
25	388.11	65	139	-	29	214	-1.03

Table 4.3: Table contains results for the zero-temperature pair-breaking current $I_{dep}(0)$, critical current I_C, critical velocity from the LO model v^*_{LO} and the slope from DO model $(dB_{C2}/dT)_{DO}$ for two temperatures for MoSi.

BS model

The BS model was fitted by fitting the equations 2.14 to the FFI measured data plotted as current density j^*/j_0 against the electric field E^*/E_0. For the value j_0 was taken the j^* value at zero applied magnetic field. This is an extrapolated value for the 25 nm sample, because of the security current limit. The only fitting parameter is E_0. From equation 2.19 we calculated h. The results of this fitting can be found in figure 4.10 at 5.0 K for the 10 (a), 15 (b), and 25 nm (c) sample and at 5.5 K for the 25 nm sample (d). Whilst the points are measurement data points, the solid lines are fits. It is clear that the fits are deviating extremely from our data points. The difference between the measurement and the fitting curve is further highlighted by the colored area. It seems that the thinner the films get, the

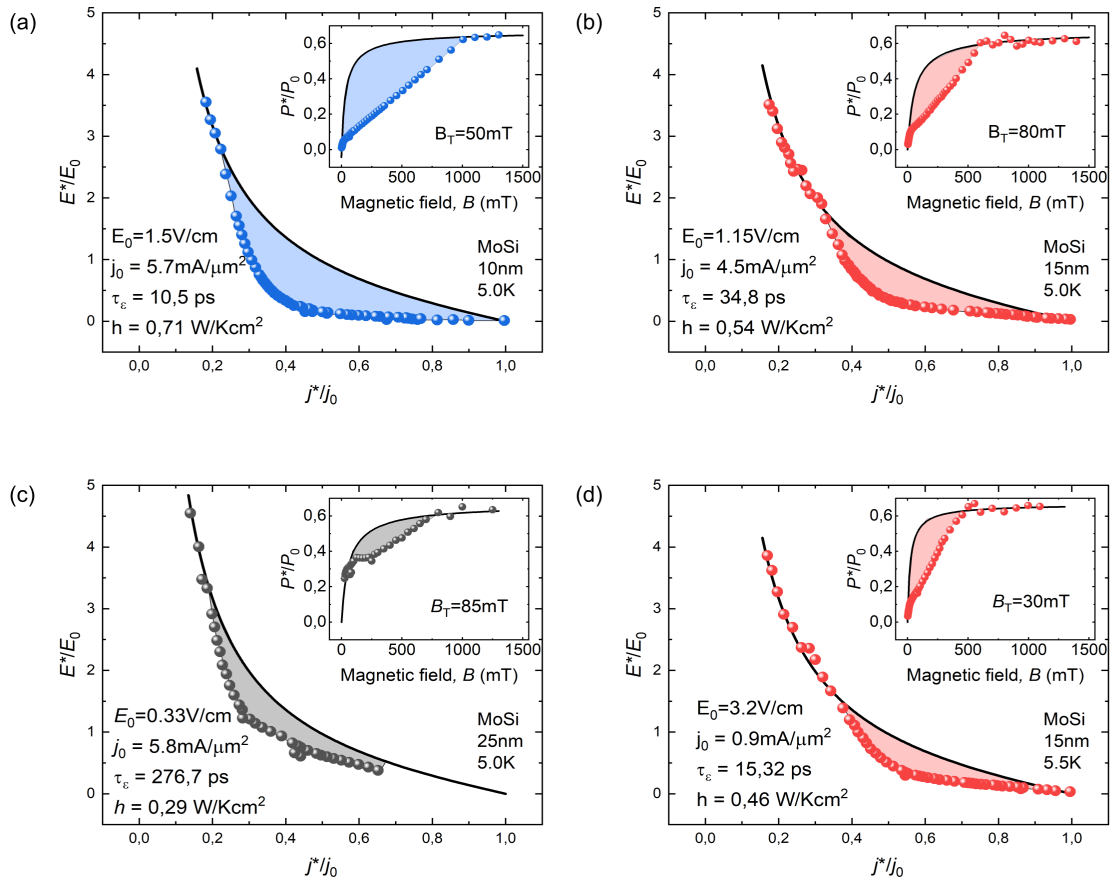

Figure 4.10: MoSi measurement data fitted to the BS model at 5.0 K for the 10 (a), 15(b) and 25 nm (c) sample and at 5.5 K for the 25 nm sample (d). Symbols are measured data, solid lines are fitting curves. Colored areas highlight the deviance from the model. All fitted and calculated values are listed inside the panels.

larger is the deviation from the fit. From this trend, one could expect that the data would fit the BS model well for bulkier samples. The authors of the BS model in their paper [55] tested their theory on a 58 nm thick In sample, which is more than twice as thick as our thickest sample. Due to the deviation, it was not possible to fit the thinnest sample of 6 nm to the model. Nevertheless, we continue our analysis by plotting P^*/P_0 against B and fitting to the equation 2.20 for the remaining three thicknesses. The fitting parameter is the transition field B_T. The fitted values and fitting curves can be found in the insets of the panels in figure 4.10. Finally, from equation 2.13 we obtain results for the energy relaxation time τ_ϵ. We observe the same dependence of τ_ϵ on thickness and temperature as in the LO model. Increase in τ_ϵ with increasing thickness and decreasing temperature. However, the value of τ_ϵ is an order of magnitude smaller compared to the values derived from the LO model.

MoSi	($\approx$78% T_C)					
d [nm]	E_0 [V/cm]	j_0 [mA/μm^2]	h [W/Kcm^2]	B_T [mT]	τ_{ep} [ns]	τ_{ee} [ps]
6	-	-	-	-	-	-
10	1.5	5.7	0.71	50	1.436	10.577
15	1.15	4.5	0.54	80	2.834	35.233
25	0.33	5.8	0.29	85	8.795	285.688

Table 4.4: Table contains results for the fitted electric field E_0, current density j_0, the heat transfer coefficient h, the transition field B_T, the electron-phonon relaxation time and the electron-electron relaxation time from the BS model for MoSi.

The transition field B_T increases with increasing thickness, but decreases with increase in temperature. Since B_T separates the regions where either the LO effect or overheating dominates the FFI mechanism, the dependence found on temperature seems correct. A higher setup temperature surely will cause overheating to occur sooner, and hence lowers the B_T value. We also note that none of the found B_T values can explain the deviating results obtained by fitting the DO model at low magnetic fields. Fitted were fields up to only 40 mT, so crossing of B_T and with that connected overheating should not have been a problem.

If we consider that we are in the overheating regime as described in the BS model, we can also calculate the electron-phonon τ_{ep} and electron-electron relaxation τ_{ee} times. Considering to be in the overheating regime seems to be well validated for thin films. The equation 2.21 is used to determine τ_{ep} and the equation of the BS model from table 2.1 to determine τ_{ee}. The Fermi velocity is for this purpose assumed to be 10^6m/s for all samples. The results of the BS model fitting can be found in table 4.4, and the results for τ_ϵ for all models to be compared with one another in the section summary table 4.5.

In conclusion, we saw that none of the models used to find τ_ϵ fit our thin film data

well. The reason for this is the lack of consideration of pinning, localized overheating, and localized flux-flow instabilities in these models. Looking back to figure 4.9 we note that we do not observe any transition field B_{cr1} as defined in chapter 2.3.2 subsection Pinning effects on FFI. This is because MoSi is only weakly pinning. Nerveless pinning must be taken into account to explain the models not fitting the data points.

We suppose that the edge quality of the samples is the main reason for the bad fits. In the following chapter 5, we will investigate whether fabricating a sample with a close-to-perfect edge will improve the fits and result in reasonable values for τ_ϵ. Since we are interested in MoSi for its use in SSPDs, we would like samples with the highest possible I_C and lowest τ_ϵ, so they can operate at high currents and recover quickly. From our thickness study, we saw that while τ_ϵ is getting smaller for thinner samples, I_C is also getting smaller. Hence we compromise with a middle thickness of 15nm to study further.

MoSi	($\approx$78% T_C)			($\approx$88% T_C)		
d [nm]	τ_ϵ (LO) [ps]	τ_ϵ (DO) [ps]	τ_ϵ (BS) [ps]	τ_ϵ (LO) [ps]	τ_ϵ (DO) [ps]	τ_ϵ (BS) [ps]
6	149	3711	-	76	4506	-
10	205	862	11	116	1242	-
15	277	808	35	177	616	15
25	1358	-	278	412	925	-

Table 4.5: Table contains results for the fitted energy relaxation times τ_ϵ as found using the LO, DO and BS model for two temperatures for MoSi.

4.2 Niobium

Niobium films were prepared on sapphire (Al_2O_3) substrates. The films were dc-magnetron sputtered (3.1.1) and lithographically structured (3.1.4) into Hall bars. The dc-magnetron sputtering was performed at room temperature. The room temperature sputtering of Nb creates dirty limit granular Nb films [105]. All films were covered with a 7 nm Si capping layer. The produced Nb films were 11, 20 and 40 nm thick. An example of one of the final Nb Hall bar of width w and with a distance between the voltage contacts l can be seen in figure 4.11. The sample in the image is contacted by silver paint to gold wires, as is required for transport and hall measurements. Data for all thicknesses were taken using the PPMS.

4.2.1 Cooling curves and critical temperature

The cooling curves for niobium were measured at a constant current of 0,1 mA. They were taken from room temperature down to bellow T_C temperatures. The measured voltage was

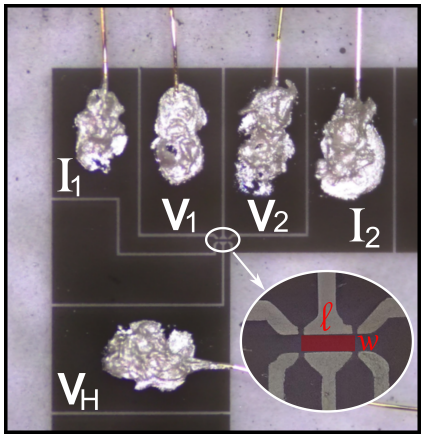

Figure 4.11: Nb experimental geometry with the sample bridge zoomed in and highlighted in red. The contacts for passing current are I_1 and I_2, and for measuring voltage V_1 and V_2. The contact V_H was made for Hall measurements.

recalculated to resistivity with $\rho = \frac{V(wd)}{Il}$. The final curves for the thinnest and thickest sample can be seen in figure 4.12 (a).

Nb, unlike the previously analyzed amorphous MoSi, has a polycrystalline structure down to at least a thickness of 4 nm. Zaytseva et al. found a transition to an amorphous state for thicknesses below 3.3 nm [91], but since our thinnest sample is of 11 nm thickness, all our samples are polycrystalline. We observe this on the lack of the SIT that was observed for MoSi. The normal resistivity of Nb drops with the decreasing temperature, a signature of an SMT. The high residual resistivity ρ_{10K} with values between 18 and 29 $\mu\Omega$cm suggests that Nb is in the granular dirty limit, where the grain boundaries make up for a significant contribution to the residual resistivity [105]. The width of the transition for different thicknesses can be seen in figure 4.12 (a) as the highlighted areas. We see that for different thicknesses this area is almost the same. The RRR and ΔR for all thicknesses can be found in table 4.6. In SMT the RRR is > 1 and depends on the purity of the sample. Thus, the thickness of the sample should not influence the purity of the sample, and the RRR will not change. Only for very small thicknesses, or clean limit superconductors, the substrate may influence the purity of the sample by a substantial amount compared to the small sample thickness, and a decrease in RRR is expected [106]. However, this decrease is expected for thinner thicknesses than the ones described here.

As depicted in the inset of figure 4.12 (a) and then again in (b), the residual sheet resistance increases with decreasing sample thickness. The reasoning for this is the same as that for MoSi. In short, a decrease in thickness decreases the electron mean free path and leads to a higher resistivity. We confirm this trend for the sheet resistance, but not for resistivity itself. The resistivity has a peak at a thickness of 20 nm. We have also seen this in MoSi, and we have attributed this to a change in the stoichiometry of the thinnest sample. In Nb, we are not sure what leads to this behavior. The simplest explanation would be that

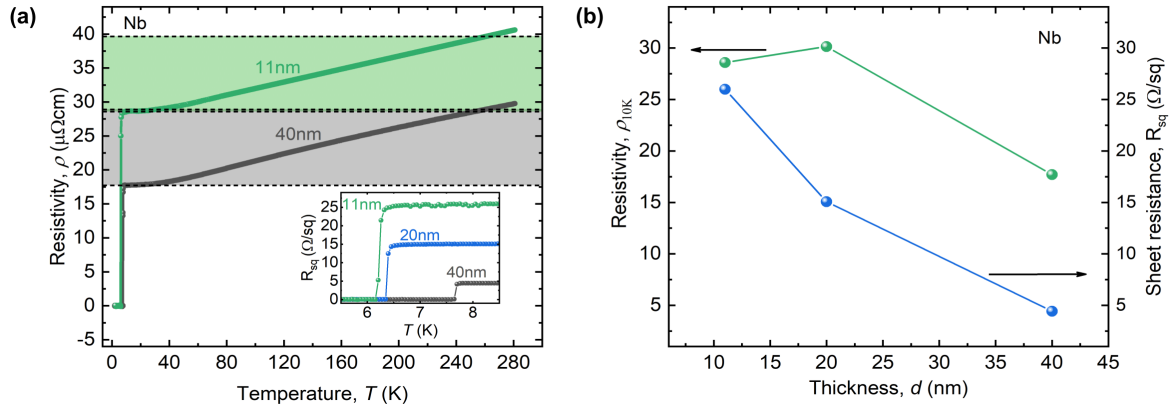

Figure 4.12: Nb cooling curves: Resistive curves taken for temperatures from 260 down to 3K for the thinnest (11 nm) and thickest (40 nm) studied Nb sample (a). Highlighted area shows the drop in resistivity between 260 and 10K. The inset shows the sheet resistance curves. Further is plotted the sheet resistance and resistivity at 10K for all thicknesses (b).

the 20 nm sample had slightly more defects compared to the other samples.

Figure 4.13 (a) shows the resistivity normalized by its value at 10K for temperatures in the vicinity of the transition for all sample thicknesses. The vertical lines point to T_C of each sample as found by the 75% criterion. The width of the transition is highlighted for the 11 nm sample as the area between the 10 and the 90% value of the 10K-resistivity. Results for T_C and ΔT_C are plotted in figure 4.13 (b). We observe a decrease in T_C, but only a very slight increase in ΔT_C with decreasing thickness. The large increase in ΔT_C for MoSi was attributed to its amorphousness; therefore, it is not expected for ΔT_C to grow for the polycrystalline Nb. Whilst in MoSi the transition width grew by 10.5 mK per nm decrease in thickness, in Nb it is only 2.5 mK. The transition is very sharp and narrow even at 11 nm, and the decrease in ΔT_C might actually just be an error factor due to the insufficient number of data points in the sharp transition.

As for the T_C-d behavior from 4.13 (b), we were unable to fit the Simonin equation 4.1. The lack of more sample thickness data and the possibility of the 20 nm sample having more defects compared to the other two, which would make its T_C lower, makes the fit unreasonable. However, we had success with the universal scaling law, which makes a connection between $T_C * d$ and R_{sq}(300 K). Since a different defect structure of one of the samples would change both T_C and R_{sq}, its data point would only change its position on the fitted curve, but would still fit on the same line as the rest of the data. The results of this fitting can be found in figure 4.14. Here, the fitting parameter B lower than 1 correctly suggests a polycrystalline structure.

Note that the Finkel'stein fit explored for the MoSi samples is specific to amorphous films and cannot be used for Nb.

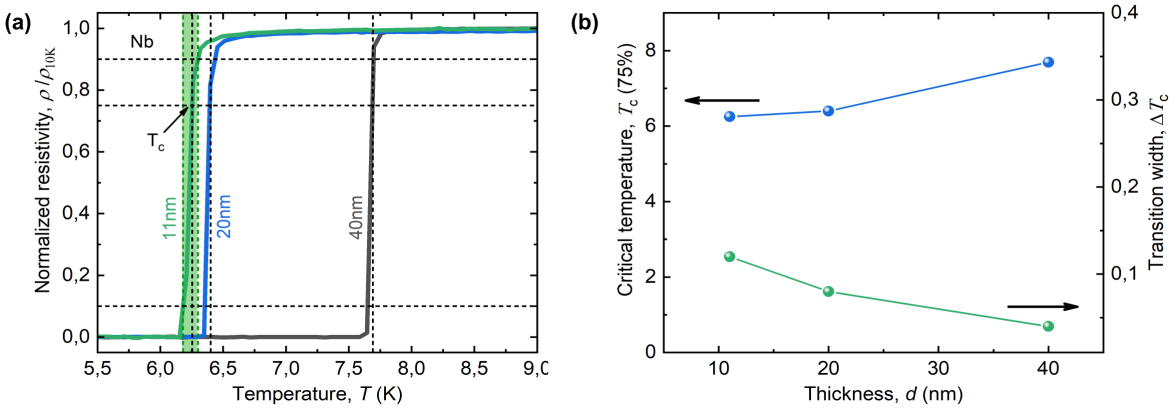

Figure 4.13: Nb critical temperature: Superconducting transitions for all studied Nb samples presented as the disappearance of the normalized resistivity (a). The vertical dashed lines point to the individual critical temperatures T_C. Highlighted green area represents ΔT_C for the 11 nm sample. All values of ΔT_C and T_C are plotted against their thickness in (b).

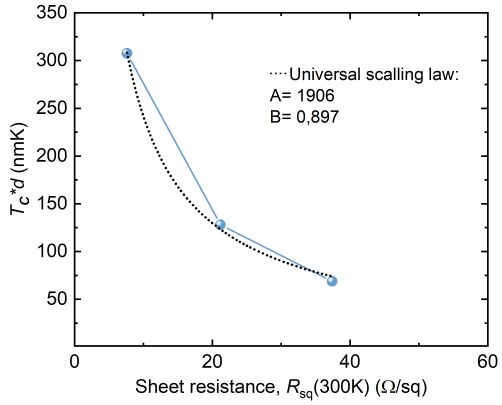

Figure 4.14: Nb data fitted to the Universal scaling law

d [nm]	w [μm]	l [μm]	T_C [K]	ΔT_C [K]	ρ_{10K} [$\mu\Omega$cm]	R_{sq} (10K) [Ω/sq]	R_{sq} (300K) [Ω/sq]	ΔR [$\mu\Omega$cm]	RRR	$\Delta(0)$ [μeV]
11	30	100	6.25	0.12	28.59	25.99	37.42	11.05	1.38	947.9
20	30	100	6.4	0.08	30.14	15.07	21.19	10.71	1.35	970.61
40	30	100	7.69	0.04	17.71	4.43	7.62	11.19	1.63	1166.29

Table 4.6: Nb critical temperature and resistivity summary. The table consists of results for the sample width w, voltage contact length l, critical temperature T_C, transition width ΔT_C, normal resistivity at 10 K ρ_{10K}, square resistance at 10 K and 300 K R_{sq}(10 K) and R_{sq}(300 K), width of the resistivity raise ΔR, residual resistivity ratio RRR and the energy gap $\Delta(0)$.

All findings of this subsection are summarized in table 4.6. The energy gap $\Delta(0)$ for all samples is also included, estimated by equation 2.1.

4.2.2 Upper critical field

Figure 4.15 depicts the normalized resistive curves measured from the absence of applied magnetic field and then up to the magnetic fields where no transition is visible anymore. These measurements are shown for the 11 nm (a), 20 nm (b) and 40 nm (c) samples. Again we observe that the broadening of the transition with increasing field is not very large, especially when compared with the large broadening that occurs for the amorphous MoSi. The intersections with the dashed horizontal line at 0.75 give the value of T_C at the curves corresponding applied field. In figure 4.15 (d) the result of this analysis, the upper critical field B_{C2} versus temperature, is plotted for all thicknesses. The data is fitted with the WHH equation 4.5. The value of the slope in the equation is taken from a linear fit in the vicinity of T_C and can be found in the table inside the figure.

The fitted parameters λ_{SO} and α can be found plotted against thickness in figure 4.16. Further in the figure is included the resulting $B_{C2}(0)$ from the WHH fitting, B_{orb} calculated by equation 4.7, and B_P calculated by equation 4.6.

We observe no paramagnetic limiting or spin-orbit scattering for the two thicker samples. The 11 nm sample, however, seems to be limited by the paramagnetic limiting field. This result is the same as what was found for MoSi. In bulk samples the paramagnetic limiting field is so high that it does not have an effect on the final B_{C2} and therefore it is equal to B_{orb}.

The shape of B_{orb} can be again understood from equation 4.9. B_{orb} follows the shape of the curves of ρ and T_C. For polycrystalline materials B_{orb} is known to increase with decreasing thickness, but due to the observed peak in ρ for the 20 nm sample, we observe a drop in B_{orb}. B_{C2} is then further reduced as a consequence of finite B_P. Comparing our results with those found in [91] on Nb films, they also found the region around 10 nm thickness to be the onset

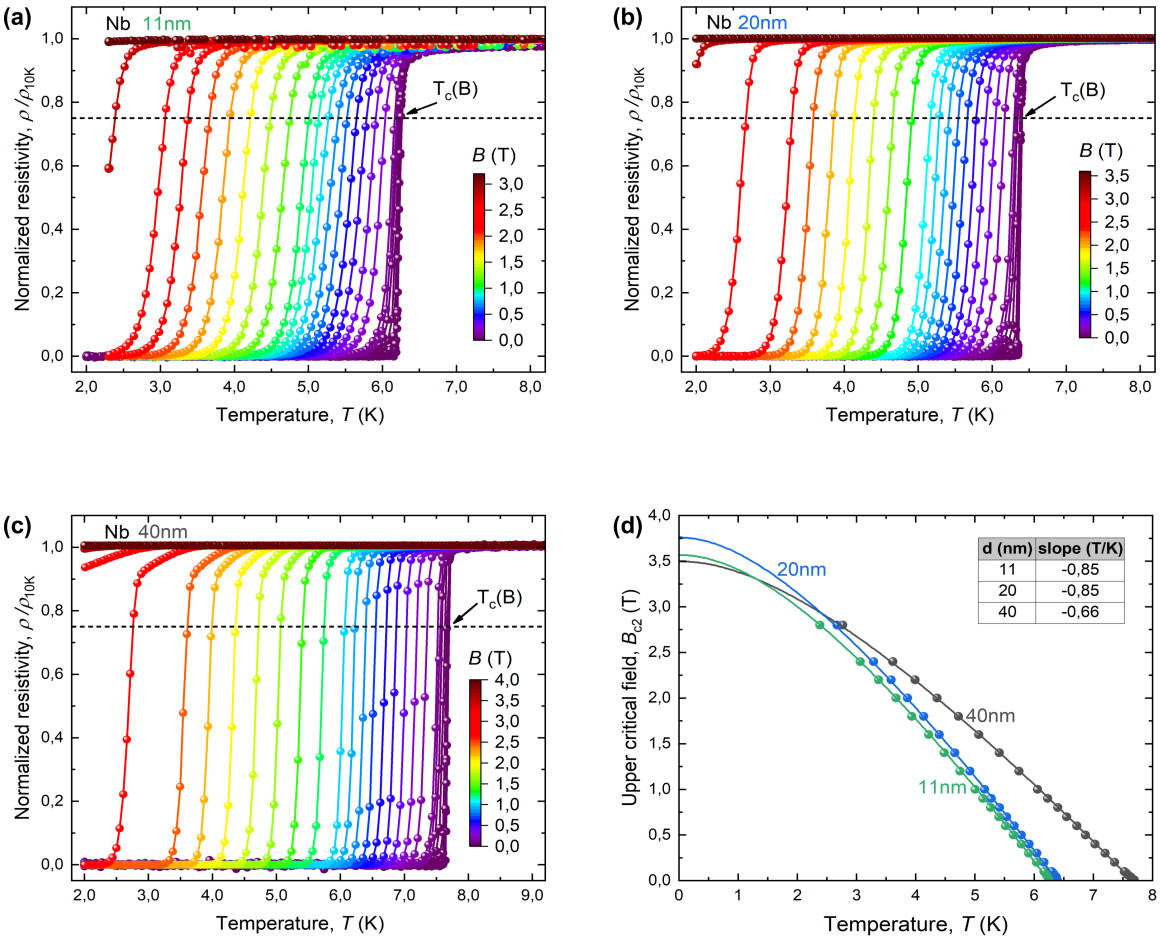

Figure 4.15: Nb upper critical field: Normalized resistive curves taken at various magnetic fields for a Nb 11 nm- (a), 20 nm- (b) and 40 nm-thick (c) film. The dashed line represents the 75% criterion at which values for the upper critical field were taken from. In (d) the resulting upper critical field are plotted against temperature. The solid line is a fit to the WHH equation.

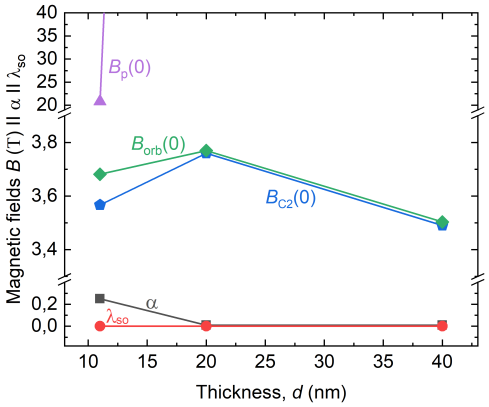

Figure 4.16: Nb WHH fitting: The WHH fitted parameters λ_{so} and α, and all the limiting fields at 0 K.

of paramagnetic limiting.

All results of this subsection are summarized in table 4.7. Included are also results for the diffusion constant D (eq. 2.5), the coherence length ξ_0 (eq. 2.3), the penetration depth λ_L (eq. 2.4) and the Pearl length Λ. Pearl length is calculated from

$$\Lambda = 2\lambda_L^2/d \tag{4.13}$$

and its results categories all of our samples as wide strips for which $w > \Lambda$.

d [nm]	dB_{C2}/dT [T/K]	B_{orb} [T]	B_{C2} [T]	WHH α	WHH λ_{SO}	B_p [T]	D [cm^2/s]	ξ_0 [nm]	λ_L [nm]	Λ [μm]
11	-0.85	3.68	3.57	0.25	0	20.83	1.29	9.467	224.145	9.135
20	-0.85	3.77	3.76	0.01	0	533.15	1.29	9.355	227.427	5.172
40	-0.66	3.5	3.49	0.01	0	495.47	1.662	9.704	159.352	1.27

Table 4.7: Nb upper critical fields summary: Table contains results for the slope, orbital limiting field B_{orb}, upper critical field B_{C2}, Maki parameter α, spin orbit scattering constant λ_{so}, Pauli limiting field B_p, diffusion constant D, coherence length ξ_0, penetration depth λ_L and Pearl length Λ.

4.2.3 Critical current and current-voltage curves

Figure 4.17 (a) shows the I-V curve of the 20 nm sample at 5.8 K in the logarithmic scale to highlight the regions described in the subsection 2.2.3. Each section is labeled in the figure with the corresponding section number. The nonlinear section III. is missing, because the FFI jumps occur already in the linear regime. Similarly as before, we use a voltage criterion

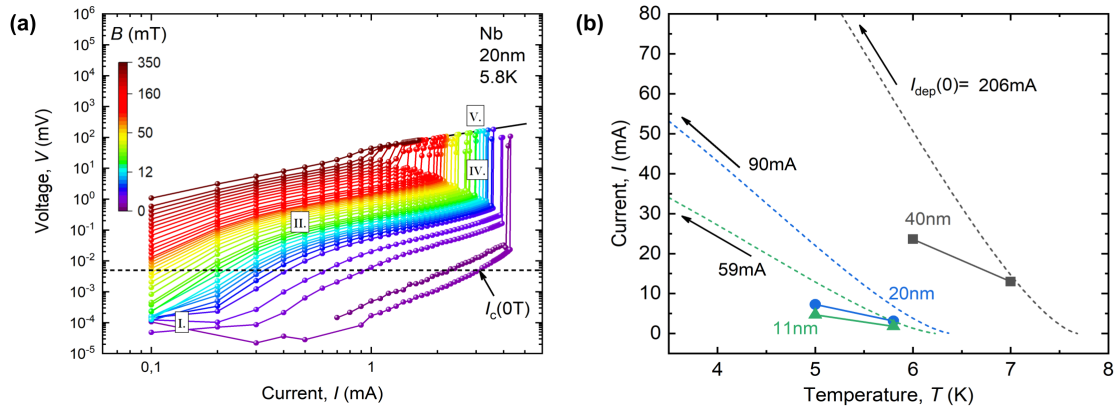

Figure 4.17: Shown are the Nb I-V curves for the 20 nm sample in 5.8 K temperature in logarithmic scale (a). They are measured at external magnetic fields corresponding to the color code in the scale bar. The vertical line at 5 μV is the criterion for the defined critical current $I_C(0)$ plotted in (b) for all sample thicknesses. Whilst symbols are measurement data points, solid lines are the pair-breaking currents. Matching colors represent same thickness.

to define a critical current I_C. The criterion is seen as the dashed horizontal line in figure 4.17 (a). We have chosen the voltage of 5 μV as the voltage criterion. This is different from the criterion we have chosen for MoSi, but we chose this to be able to read out the data without interpolation. The results for $I_C(0)$ for all sample thicknesses and measured temperatures are found in figure 4.17 (b). Once again we observe that the thinner the sample, the lower I_C it has. The temperature dependence of I_C is compared with the theoretically highest achievable pair-breaking current calculated by equation 4.11 and is depicted as the dashed lines in figure 4.17 (b). Matching colors correlate the calculated pair-breaking current with the measurement data of the same thickness. We observe the same thickness dependence and similar temperature dependence. At 78% T_C the I_C value of the thickest sample is only about 46% of the theoretically predicted value and the two thinner samples are only around 35% of the theoretically predicted value. We attribute some of this decrease in critical current to poor edge quality, as explained in the next chapter. A comparison of I_C between the MoSi and Nb samples should be avoided due to the different voltage criterion used to define I_C. The table 4.8 contains the results for I_C and $I_{dep}(0)$.

In figure 4.18 are the I-V curves in linear scale for the 11 nm (a,b), 20 nm (c,d) and 40 nm (e,f) sample. The panels on the left side are taken at about 90% of T_C and the panels on the right at about 78%. They are measured at external magnetic fields that correspond to the color code in the scale bar. Straight vertical lines correspond to region IV., the FFI region, from subsection 2.2.3. For the thickest sample in the lower temperature range in figure 4.8 (f), the I-V curves for low magnetic fields do not end in FFI jumps. This is because we have limited the highest applied currents to 20 mA to protect the samples from burning, and the

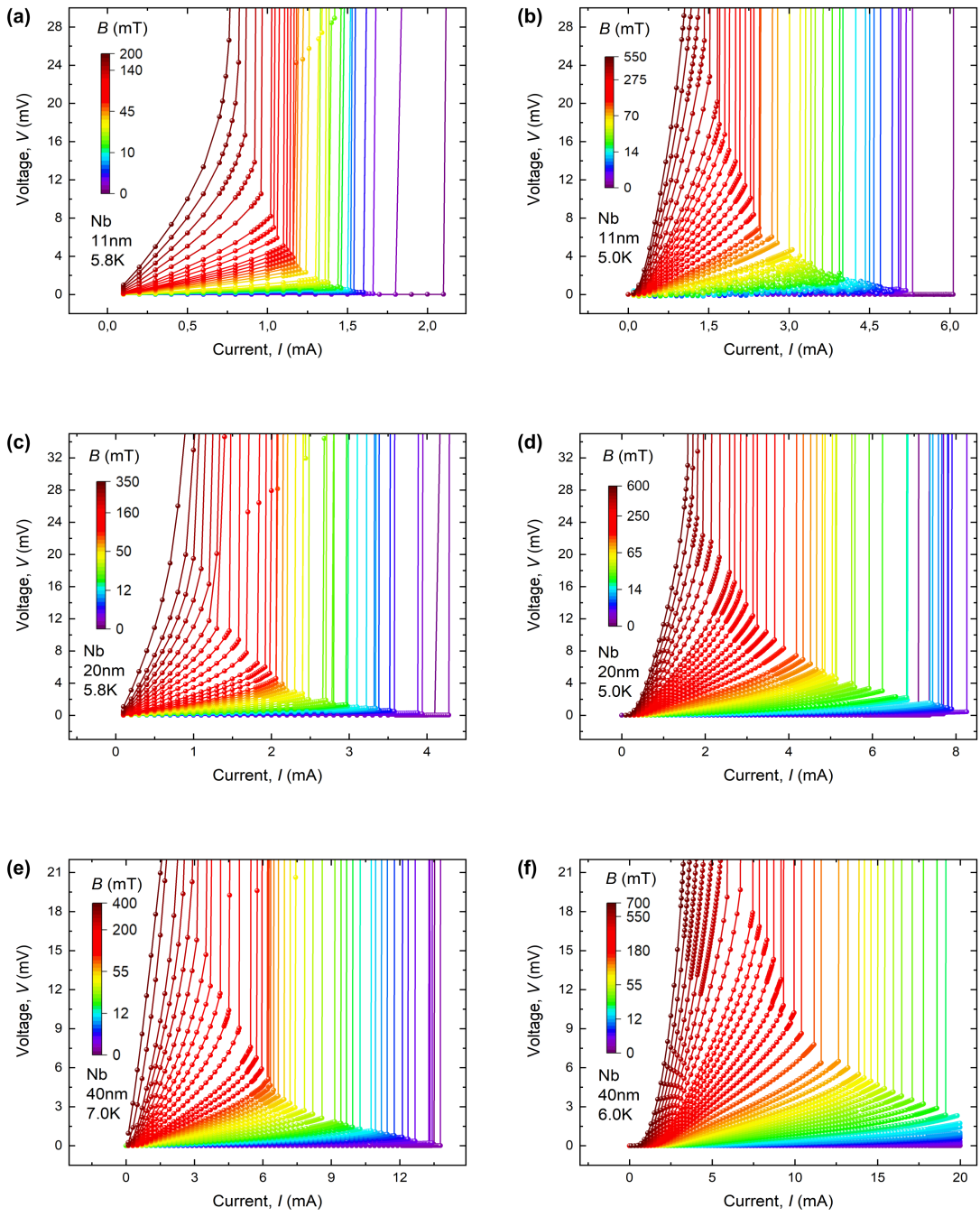

Figure 4.18: Nb I-V curves for the 11 nm (a,b), 20 nm (c,d), and 40 nm (e,f) samples. They are measured at external magnetic fields corresponding to the color code in the scale bar. Panels on the left side are taken at about 90% of T_C and on the right at about 78%.

jumps for these low fields only occur at currents above this security limit.

4.2.4 Critical velocity

The calculated critical velocity v^*, as introduced in subsection 2.3.2 with $v^* = V^*/Bl$, is plotted in figure 4.19.

LO and DO models

First, ignoring the complicated field dependency of v^*, we fit the LO model to the data. We set v^* to a single value by fitting a horizontal line to the data at higher magnetic fields. In cases where v^* does not approach and settle to a single value, we set the horizontal line to the highest achieved v^*. Then taking this value into equation 2.12 gives the result for τ_ϵ as defined by LO. The results for two temperatures and all samples can be found in figure 4.19 (a,b). From this analysis we conclude that τ_ϵ increases with thickness and has values raging from 34 to 130 ps when the temperature is at about 90% of T_C and from 163 to 457 ps at about 78% of T_C. The thickness dependence is the same as that found for MoSi. However, the values are a little bit lower, suggesting a more efficient energy relaxation in Nb compared to that of MoSi. τ_ϵ raises with dropping temperature. This is again consistent with findings in MoSi and can be explained by a drop in electron-phonon interactions at lower temperatures.

Looking at the magnetic dependency of v^* we conclude that it is much more complicated than what is described by the DO model alone. In low fields we observe a raise in v^* up until a certain field B_{cr1} as defined in chapter 2.3.2 subsection Pinning effects on FFI. This rise is a consequence of strong pinning to non-homogeneously distributed defects. This pinning weakens whilst vortex-vortex interaction raises with raising field and allows the vortices to order themselves. Hence, a rise in measured average velocity is observed. Once all vortices are ordered, the dependency on field is expected to switch to the one known from the DO model. However, we have observed a further section where an increase in v^* is present with increasing field. This happens in the intermediate fields. This is especially dominant in the 11 nm sample at 90%T_C (figure 4.19 (a)). We attribute this to very strong localized overheating that turns a part of the film normal conducting. This would be masked as high vortex velocity, due to the increase in voltage used to calculate v^*. The onset of this intermediate field v^* increase is at about 25-30 mT, which is consistent with the later found transition field B_T from the DO model.

The data were fitted to equation 2.22 from the DO model. The importance was given to fit the data at low magnetic fields. However, data points for fields lower than the crossover field B_{cr1} are omitted from the fit. Fitting the entire magnetic field range was not possible, as good fits at low magnetic fields result in very bad fits at high magnetic fields. In addition to τ_ϵ, we had to leave the parameter of slope, present in the equation in the definition of the parameter D, as a free parameter. The resulting curves and the fitted parameters are found in figure 4.19 (c,d). No curve is fitted to the 78% T_C 40 nm data because of lack of data points for low magnetic fields as a consequence of the security current limit. The fitted values for

slopes are lower than those previously found from B_{C2} measurements (compare to values in table 4.7). The dependency on thickness is flipped compared to before and is increasing with thickness. The same goes for the resulting τ_ϵ that now shortens with increasing thickness and dropping temperature in contrast to the results of the LO model. Similarly as for MoSi, the DO model fails to represent the data correctly in low magnetic fields, and the resulting τ_ϵ, with values between 330 and 3000 ps, is most probably incorrect. All the fitted parameters of the LO and DO model can be found in table 4.8 and the resulting τ_ϵ for both models in table 4.10.

Nb		($\approx 78\%T_C$)			($\approx 90\%T_C$)		
d [nm]	$I_{dep}(0)$ [mA]	I_C [mA]	v^*_{LO} [m/s]	$(dB_{C2}/dT)_{DO}$ [T/K]	I_C [mA]	v^*_{LO} [m/s]	$(dB_{C2}/dT)_{DO}$ [T/K]
11	59	4.69	680	0.2	1.8	1142	0.035
20	90	7.3	500	1.214	3.14	728	0.36
40	206	23.6	470	-	13	700	0.569

Table 4.8: Table contains results for the zero-temperature pair-breaking current $I_{dep}(0)$, critical current I_C, critical velocity from the LO model v^*_{LO} and the slope from DO model $(dB_{C2}/dT)_{DO}$ for two temperatures for Nb.

BS model

The BS model was fitted by fitting equations 2.14 to the FFI measured data plotted as current density j^*/j_0 against the electric field E^*/E_0. For the value j_0 was taken the j^* value at zero applied magnetic field. This is an extrapolated value for the 40 nm sample, because of the security current limit. The only fitting parameter is E_0. From equation 2.19 we calculated h. The results of this fitting can be found in figure 4.20 at 78% of T_C for the 11 (a), 20 (b) and 40 nm (c) samples and at 90% of T_C for the 20 nm sample (d). Whilst points are measurement data points, the solid lines are fits. Just like for MoSi, the fits are deviating in the middle region from our data points. The difference between the measurement and the fitted curve is further highlighted by the colored area. Previously, we have seen that the thinner the films, the bigger the deviation from the fit. This seems to be the case again for Nb. Although we see a big improvement in the fit going from the 11 to the 20 nm sample, we do still observe a deviance from the fit at the 40 nm sample. The deviance is now on the opposite side of the curve. This suggests that the model actually underestimates when the FFI occurs. Up until now, the model overestimated the location of the FFI, which means that there was an effect present in the measurements that triggered the FFI sooner (meaning at smaller currents and voltage) than what BS predicted. In the next chapter, we will talk about how the edge can trigger the FFI sooner. For the 40 nm sample the underestimation can be a consequence of localized overheating, raising the measured voltage. Nevertheless we continue our analysis

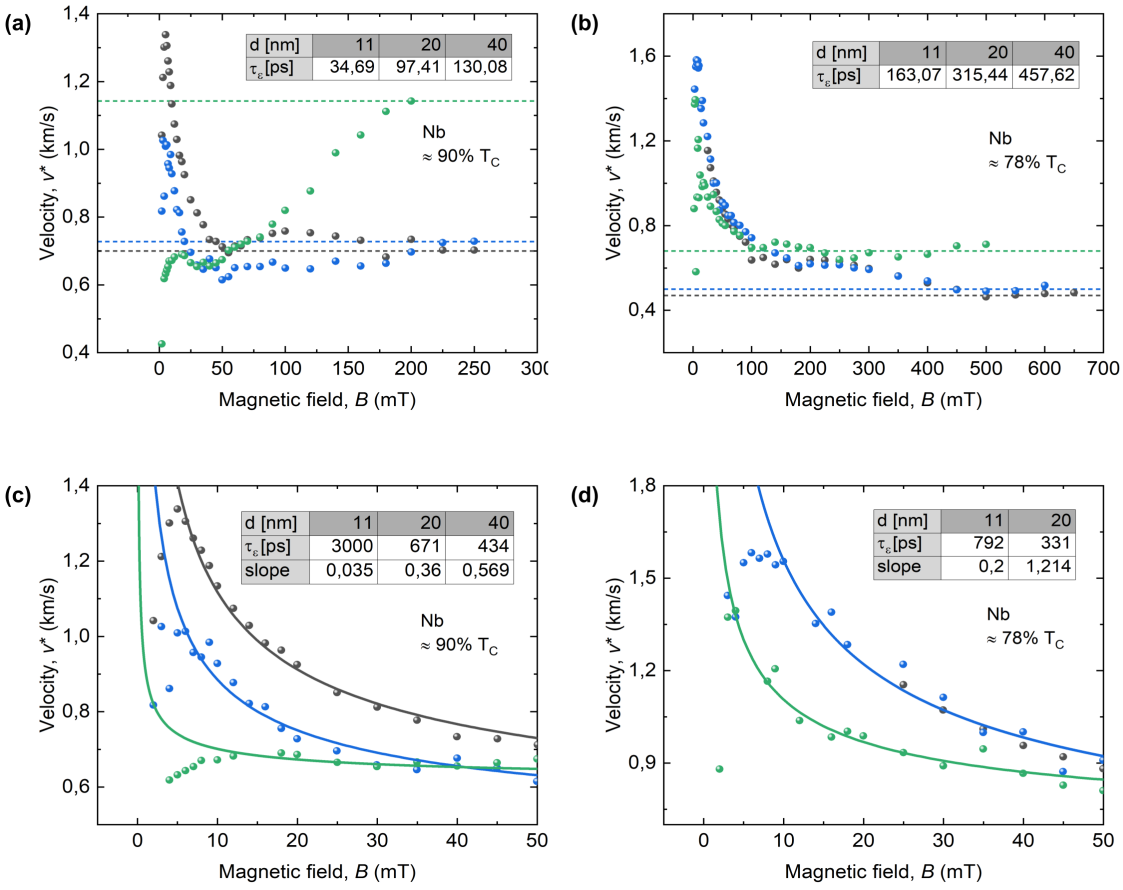

Figure 4.19: Nb maximal velocity v^* for all thicknesses fitted by LO model (a,b) and by DO model (c,d). Panels on the left side are taken at about 90% of T_C and on the right at about 78%. Symbols are measured data, solid lines are fitting curves. Resulting fitting parameters are given in the tables included in each panel.

by plotting P^*/P_0 against B and fitting to the equation 2.20. The fitting parameter is the transition field B_T. The fitted values and fitting curves can be found in the insets of the panels in figure 4.20. Finally, from equation 2.13 we obtain results for the energy relaxation time τ_ϵ. We observe the same dependence of τ_ϵ on thickness and temperature as in the LO model. Increase in τ_ϵ with increasing thickness and decreasing temperature. The value of τ_ϵ is an order of magnitude smaller compared to the values derived from the LO model for the 11 nm and 20 nm sample. The 40 nm sample value of 479 ps is very close to the LO derived value of 457 ps. This suggests that for bulkier samples, when the equation 2.14 fits the data well, the obtained τ_ϵ value will not differ much from the obtained value of the LO model.

Nb	($\approx 78\%T_C$)					
d [nm]	E_0 [V/cm]	j_0 [mA/μm^2]	h [W/Kcm^2]	B_T [mT]	τ_{ep} [ns]	τ_{ee} [ps]
11	1.35	16	1.9	25	0.59	11.89
20	0.85	14.7	1.78	35	1.14	30.79
40	0.075	21	0.38	35	12.9	498.18

Table 4.9: Table contains results for the fitted electric field E_0, current density j_0, the heat transfer coefficient h, the transition field B_T, the electron-phonon relaxation time and the electron-electron relaxation time from the BS model for Nb.

In the overheating regime as described in the BS model, we can also calculate the electron-phonon relaxation τ_{ep} and electron-electron relaxation τ_{ee} times. The equation 2.21 is used to determine τ_{ep} and the equation of the BS model from table 2.1 to determine τ_{ee}. The results of the BS model fitting can be found in table 4.9 and the results for τ_ϵ for all models to be compared with one another in the section summary table 4.10.

Nb	($\approx 78\%T_C$)			($\approx 90\%T_C$)		
d [nm]	τ_ϵ (LO) [ps]	τ_ϵ (DO) [ps]	τ_ϵ (BS) [ps]	τ_ϵ (LO) [ps]	τ_ϵ (DO) [ps]	τ_ϵ (BS) [ps]
11	163	792	12	35	3000	-
20	315	331	30	97	671	9
40	458	-	480	130	434	-

Table 4.10: Table contains results for the fitted energy relaxation times τ_ϵ as found using the LO, DO and BS model for two temperatures for Nb.

In summary, we saw very similar results to those found for MoSi when it came to the energy relaxation times. The lack of consideration of local FFI effects causes inconsistencies in the models. The justification for this statement follows from the next chapter.

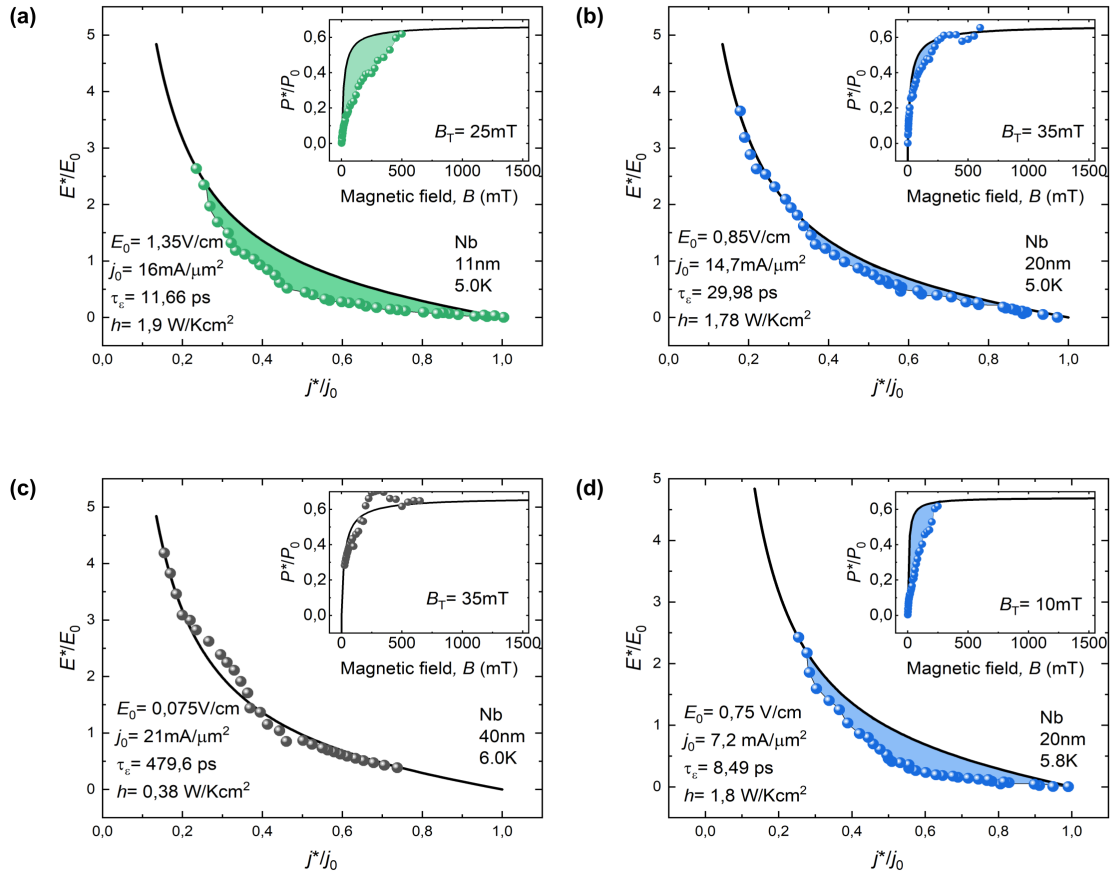

Figure 4.20: Nb measurement data fitted to the BS model at 5.0 K for the 11 nm (a) and 20 nm (b) sample, at 6.0K for the 40 nm (c) sample and at 5.8 K for the 20 nm (d) sample. Symbols are measured data, solid lines are fitting curves. Colored areas highlight the deviance from the model. All fitted and calculated values are listed inside the panels.

4.3 Conclusions

When comparing the two samples of different crystallization, amorphous and polycrystalline, based on their thickness dependence study, we conclude that apart from ΔT_C and B_{C2}, the thickness dependence of all parameters seems to have the same trends despite the different crystallization. The energy relaxation times obtained for both materials are in the same unit scale. It is then the difference in the diffusion constant that makes MoSi a favorable material for SSPD use. A lower D of the MoSi will ensure that the hotspot, created after a photon strikes the SSPD, remains contained to a smaller area. This smaller area can recover quicker, giving MoSi the advantage of a shorter dead time.

Chapter 5

Edge barrier effects

The thickness studies from the previous chapter hinted on the presence of effects that are not described in the present models used to obtain the energy relaxation times. Since this parameter is used to judge materials for their potentiality for use in SSPDs, it is important to find a reliable way to gain information about the relaxation time. We have seen how in Nb the lack of incorporating vortex pinning in the DO model made it impossible to describe the low field regime, but even for MoSi, which essentially is weakly pinning, the DO model did not fit the entire region of fields, nor did it lead to convincing results of τ_ϵ. We have also seen that the BS model fits worsen for thinner samples. This means that effects were present that led the FFI to occur at lower currents than what the BS model predicted. The idea of finding the responsible effects came from the local flux-flow instability model and the edge-controlled instability model as introduced in chapter 2.3.2. The local flux-flow instability model recognizes that an FFI jump in the linear regime is connected to a localized normal conducting region. This region can, under certain conditions, grow and switch the entire sample to a normal conducting sample. This means that it undergoes an FFI jump. However, the model introduced is very specific to the case of a heated band crossing the sample. In our experiments, we observed the FFI jump to occur in the linear regime, but we do not believe to have such a heated band. In the edge-controlled instability model, similar local FFI is described. Here, the localization comes from the edge barrier for vortex entry. Defects on the edge cause hot spots as a consequence of local suppression of the edge barrier due to variation of the material parameters. Notches in the edge cause hot spots as a consequence of the current crowding effect. The hot spots can then shift the occurrence of the FFI jump. The edge-controlled instability model does not provide us with a tool to extract energy relaxation times. In order to fit the original BS model to thin film data, we need to suppress any defects and notches on the edge by creating very smooth, clean edges. We also saw that the thinner the sample, the farther we were from fitting the BS model. This is because in a thinner sample the edge effect overshadows any present volume effects.

We chose MoSi to perform the measurements on, because it did not show overheating and had weaker pinning than Nb. MoSi is a dirty superconductor, which makes it a great

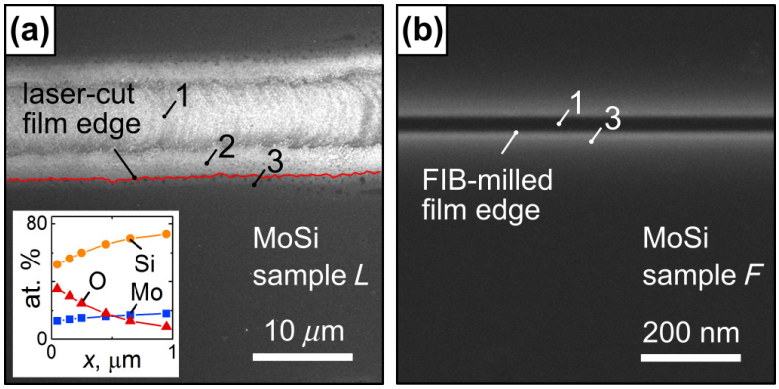

Figure 5.1: MoSi edge roughness: SEM images of the patterned edges of the laser cut sample L (a) and FIB milled sample F (b). Note the different scale bar in the panels. The inset in panel (a) is the material composition near the edge of sample L.

candidate for the edge-controlled instability model that was developed for such. As for the thickness, we have chosen to work with a 15 nm thick MoSi sample. We are essentially interested in MoSi for its use in SSPDs and thus are looking for the highest possible I_C and lowest τ_ϵ for quick device recovery. From our thickness study, we saw that while τ_ϵ is getting smaller for thinner samples, I_C is also getting smaller. The mid of the range thickness of 15 nm should give us satisfying values for both I_C and τ_ϵ.

The smooth edge should, in addition to being able to fit the BS model better, lead to higher critical velocity v^* and faster heat removal. The following sections will introduce the experimental and modeled results.

5.1 Edge quality

Compared were two 15 nm thick amorphous MoSi films. The preparation methods were the same as for the MoSi in section 4.1 with the only difference in patterning. Whilst one of the films was patterned as in section 4.1 using laser beam etching (3.1.2), the other was patterned using focused-ion beam-induced milling (3.1.3). These methods lead to very different edge roughness. From here on out we will refer to the laser-patterned sample as sample L, and to the FIB milled one as sample F. SEM images for sample L (a) and for sample F (b) can be seen in figure 5.1.

The laser beam leaves behind a pattern resembling that of a pattern left behind metal welding. The beam power, focal spot size, and speed of rastering give rise to the final shape of the edge of the pattern. The parameters used can be found in section 3.1.2. The laser beam is centered to region 1 in 5.1 (a) with a focal spot size of 6 μm. The evaporation of MoSi takes place within the focal spot and also 2-3 μm beyond the focal spot (region 2). Region 3 is what we define as the edge region of the sample, and the red line outlines the edge of the sample. The edge has a sawtooth-like shape, creating an irregular variation of the edge barrier for vortex entry. About 1 μm away from the edge into the edge region 3 a

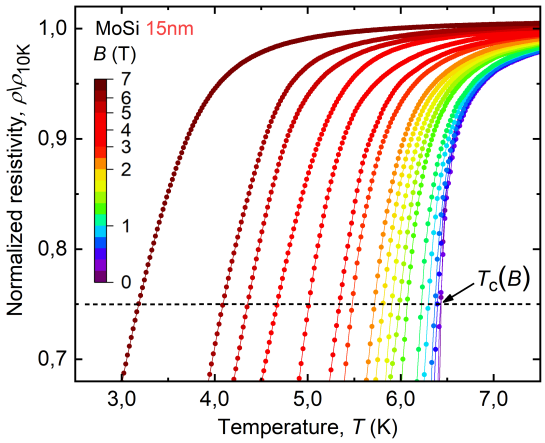

Figure 5.2: Normalized resistive curves taken at various magnetic fields for a 15 nm MoSi film. The data points are taken from measurements on sample L, but are representative for both sample L and F. The dashed line represents the 75% criterion at which values for the upper critical field were taken from.

variation of the composition is registered by EDX spectroscopy (3.2.2). The results can be found in the inset of panel 5.1 (a). The higher oxygen content leads to the degradation of the superconducting properties in the edge region.

FIB milling leaves behind a much smoother edge than the one created by laser. The setup and parameters used can be found in section 3.1.3. The FIB is centered to region 1 in 5.1 (b) with a focal spot size of 20 nm. The material is removed on impact by the electrons of the FIB hitting the surface inside the focal spot. Unlike in laser etching, there is no melting (evaporation) of the material beyond the focal spot size. Therefore, region 2 is missing from 5.1 (b). The region 3 is again the edge region of the sample. And the line separating regions 1 and 3 is the edge of the sample. Despite the much larger magnification compared to the one in the laser cut edge shown in (a), the edge in (b) is visually smooth. AFM measurements have shown a deviation of only up to 0.5 nm from a perfectly straight line along the edge, categorizing the FIB created edge as a close-to-perfect edge barrier for vortex entry. About 10 nm away from the edge into the edge region 3 a trace of implanted Ga ions can be seen as the lighter area in region 3 and calculated from simulations.

In figure 5.2 are the normalized resistive curves measured for various applied magnetic fields for sample L. The intersections with the dashed horizontal line at 0.75 give the value of T_C at the curves corresponding applied field. The result of this analysis, the upper critical field B_{C2}, is plotted in the figure of the previous chapter 4.5 (d). All the values of the parameters in table 4.1 and 4.2, can be taken as representative of both sample L and F. The parameters found in all the tables in the section 4.1.3, are only representative of sample L. The values of these parameters for sample F will be presented in the following section and

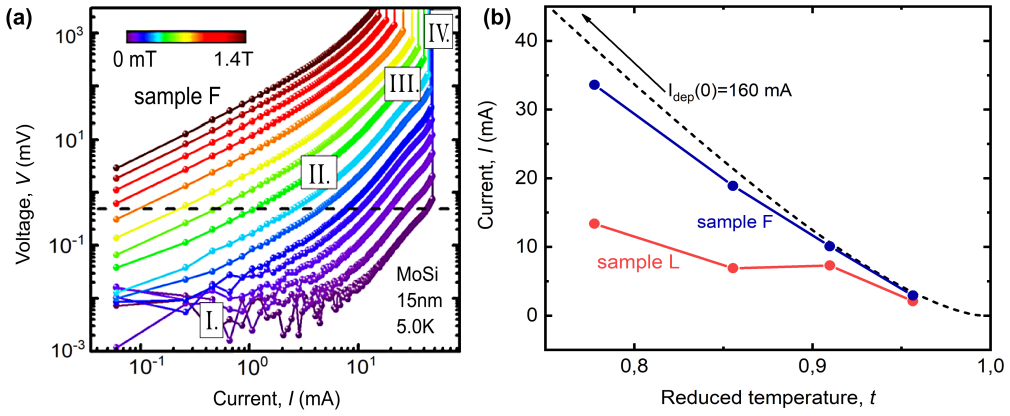

Figure 5.3: Shown are the I-V curves for sample F in 5.0K temperature in logarithmic scale (a). They are measured at external magnetic fields corresponding to the color code in the scale bar. The vertical line at 0.5mV is the criterion for the defined critical current $I_C(0)$ plotted in (b) for sample F and L. Symbols are measurement data points, the solid line is the pair-breaking current I_{dep}.

compared with those of sample L.

5.2 Sample comparison

5.2.1 Critical current and current-voltage curves

The current-voltage curves for sample F were taken, similarly to those taken for sample L, at various temperatures and a series of external magnetic fields. We can find the I-V curves of sample F taken at 5 K and presented on a logarithmic scale in figure 5.3 (a). The roman numerals are given to sections of the I-V curves as described in section 2.2.3. For the first time in this thesis we indicate the nonlinear section III. that for all previously studied samples was absent due to an FFI outbreak in the earlier, linear section of the curves. The difference in the linear and nonlinear sections can be better seen in the linear scale and will be addressed further on.

The dashed line in figure 5.3 (a) is the 0.5 mV voltage criterion chosen to define the critical current I_C. Points derived by this criterion for curves measured at close to zero magnetic field and various temperatures can be seen in 5.3 (b) for both of the samples. We compare these with the theoretically predicted depairing current I_{dep} from equation 4.11. The resulting curve is the same as in figure 4.7 (b) for the 15 nm sample. Upon comparison of the curves for sample L and sample F, we conclude that the critical current is pushed to higher values for sample F, closer to the theoretically predicted values. This means that the edge barrier and the superconducting state are broken at higher driving currents when it comes to the nice smooth edge compared to the rough edge of sample L. Already this achievement shows

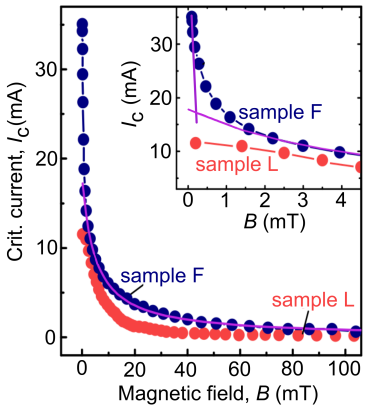

Figure 5.4: Magnetic field dependency of the critical current of sample F and L. Solid line is a fit to $1/B$. The inset is a zoomed in low field region. Here the solid lines are a fit to $1/B$ on the right and a fit to a straight line on the left.

the big importance of fabrication methods in creating superconductors that are resilient to use in higher currents.

Now deriving I_C, using the same voltage criterion as before, for all magnetic fields allows us to have a look at what might be happening inside our samples and the states the sample goes through as the field is being raised. The magnetic field dependence of I_C for both samples is presented in figure 5.4.

Theoretically, we can calculate the magnetic field B_{stop} at which a switch from the vortex-free Meissner state to the mixed state occurs. This is given in [107] by

$$B_{stop} = \frac{\Phi_0\sqrt{1 + w/(\pi\Lambda)}}{2\sqrt{3}\pi\xi(T)w}. \tag{5.1}$$

Here again the factor $\sqrt{1 + w/(\pi\Lambda)}$ must be included for wide strips, like ours, to take into account the non-uniformly distributed current throughout the width of the sample. For our samples, we obtain the value of 0.16 mT. Only for fields smaller than this value, we expect to see a linear decrease of $I_C(B)$. This linear decrease is a signature of the vortex-free state and can be written as

$$I_C(B) = I_C(0T)(1 - B/2B_{stop}). \tag{5.2}$$

For fields above B_{stop}, the decrease in $I_C(B)$ slows down and can be fitted to the dependency $1/B$, and $1/\sqrt{B}$ for very large fields. These are the regions of the mixed state.

By fitting $1/B$ to the measurement data of sample F we derive B_{stop} as the crossing point of this fitting curve with a linear fit to the data points at the smallest field values. We obtain B_{stop} around 0.2 mT. This is very close to the theoretically predicted value. The fitted curve of $1/B$ is seen as the solid line in figure 5.4. In the inset of this figure we see a zoom-in into the smallest applied magnetic fields with both of the fitting curves and their crossing point. The large $I_C(0)$ value and its steep decrease in small fields could be an indication of

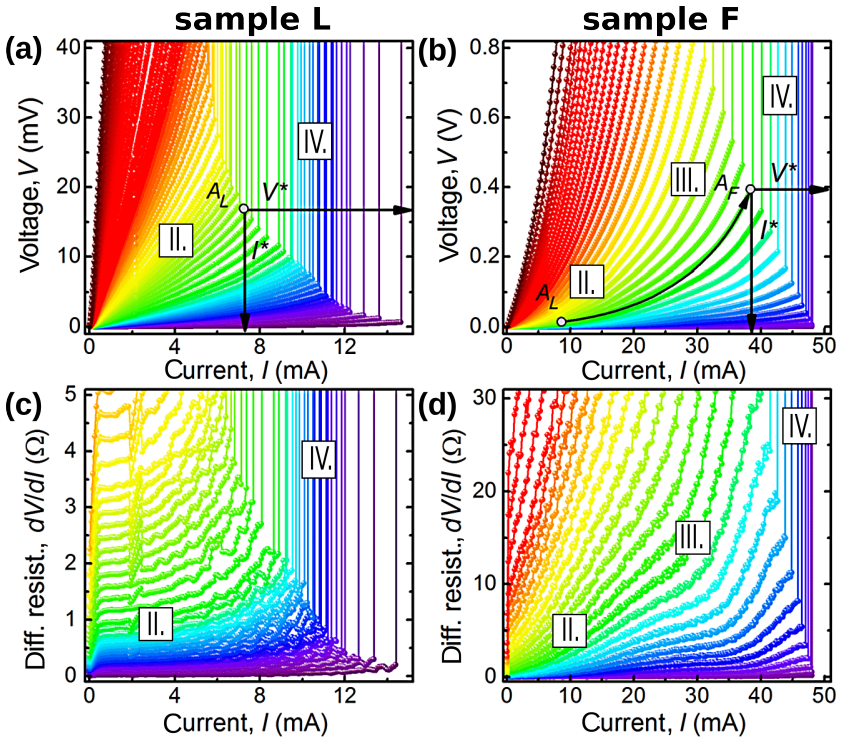

Figure 5.5: MoSi I-V curves for the 15 nm sample L (a) and sample F (b) at 5.0 K. They are measured at external magnetic fields corresponding to the color code in figure 5.3 (a). The instability voltage V^* and current I^* are indicated for the curves at B = 69 mT. Panels underneath are the current dependencies of the differential resistances for sample L (c) and sample F (d).

the vortex-free state. The higher values of I_C(B→0) compared to sample L suggest a strong edge-barrier effect. A good fit to $1/B$ indicates a dominating role of the edge barrier for vortex entry, compared to the dominating role of intrinsic (volume) pinning present when $I_C(B)$ can be better described by $1/\sqrt{B}$. The transition to $1/\sqrt{B}$ dependency occurs only in larger fields (around 300 mT) in sample F. The contribution of volume pinning in low fields is therefore negligible. This is supported by the high structural homogeneity of the MoSi films seen in the TEM images in 4.1 (a).

For sample L, we would expect a decrease in I_C(B→0) and B_{stop} due to the reduction in the edge barrier strength as a consequence of the rough edge. We observe smaller I_C(B→0) values, but it is difficult to place the correct value of B_{stop} from the measurements. The I_C(B→0) as seen in the inset of the figure is completely flattened. The data point curve starts to deviate from $1/B$ about 2 mT sooner than for sample F, followed by an almost flat region, which can not be described by a vortex-free state. We believe that this might be a consequence of the laser beam changing the composition of the sample in up to 1 μm from the edge (registered by EDX spectroscopy in the inset of figure 5.1) and hence causing some additional pinning near the edge.

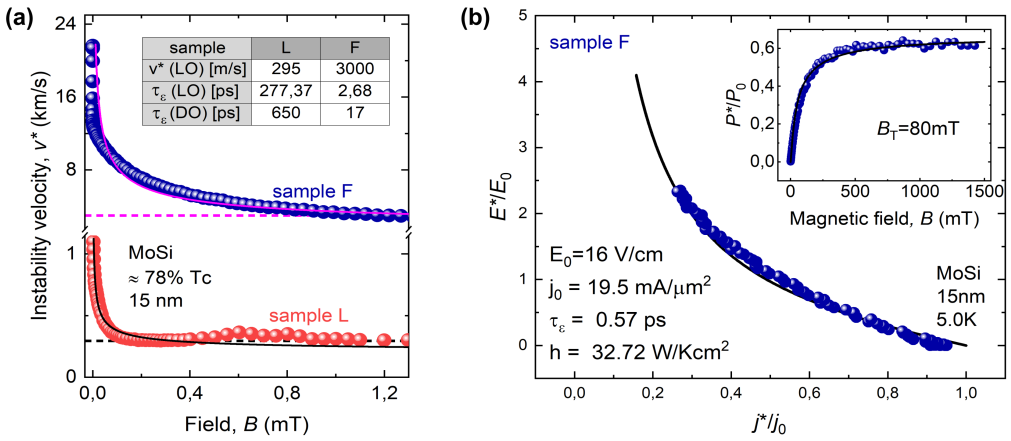

Figure 5.6: Maximal velocity v^* for sample L and F (a) at 5.0 K. Dashed lines are fits of the LO model and full lines are fits of the DO model. The resulting fitting parameters are given in the table included in the panel. In panel (b) are the data of sample F fitted to the BS model at 5.0 K. Symbols are measured data, solid lines are fitting curves. All fitted and calculated values are listed inside the panel.

The current voltage curves at 5 K for both samples in linear scale can be found in panels (a,b) of figure 5.5. Based on these panels, we want to emphasis the broader range of the nonlinear regime III. in sample F. This behavior is illustrated on the appearance of the I-V curve for sample F and sample L taken at the same external magnetic field value of 69 mT. Whilst the FFI in sample L is triggered in point A_L, in sample F the low resistive I-V curve continues beyond the A_L point in a strongly nonlinear curved dependency up to the point A_F, where FFI is triggered. This point is placed at a much higher current and voltage than the point A_L. This enhancement is most prominent for low magnetic fields. All of this suggests a mechanism connected to the edge roughness that triggers the FFI much earlier in sample L. The lack of, in sample L, and the switch to a broad one, in sample F, of the nonlinear regime is also made visible in the differential resistance dV/dI in figure 5.5 (c,d).

5.2.2 Critical velocity

After taking note of the voltage V^* and current I^* at which the FFI is triggered (see figure 5.5 (a) for an example), we can calculate the maximal vortex velocity given by the standard relation $v^* = V^*/(BL)$. The results are presented in figure 5.6 (a). Right on first glance, we observe an improvement of the maximal velocity the vortices can reach in the FIB milled sample. Whilst in high fields the velocities in sample F are about 10 times larger than in sample L, in fields up to 200 mT they are more than 20 times larger.

LO and DO models

To calculate the energy relaxation time τ_ϵ from the LO model, we are interested in the velocity value, where it is constant in the field, because LO did not consider the magnetic field dependency in their model. The chosen values can be seen in the figure as dashed lines and in the inserted table as v^*(LO). The obtained τ_ϵ is 277 ps for sample L (this is the same value as in the previous chapter in table 4.5) and 2.68 ps for sample F. The DO model is fitted using equation 2.22. The value of the slope was taken from table 4.2 for both samples as -2.8. The only fitting parameter was therefore τ_ϵ. The fitted curves correspond to the solid lines in 5.6 (a). Here, the value τ_ϵ for sample L differs from the value previously acquired in table 4.5. There we gave the greatest importance to fit the low magnetic fields, whilst here we fitted the entire magnetic field spectrum. The fits are obtained with τ_ϵ=650 ps for sample L and 17 for sample F. We note the fits are not perfect, but this is a consequence of the neglected overheating effect, which we will derive later to be of importance for all fields above 80 mT for both samples. For sample L, we attribute the poor fit also to the strong local character of the FFI. Sample F fits poorly in low magnetic fields, we assume that the number of vortices n differs from what is assumed from the relation $n\Phi_0 = BS$, where S is the area of the sample. This assumption is essential to the DO model.

A true energy relaxation time should be an intrinsic property of the material and therefore be the same for both samples. The different obtained values for sample L and F for both LO and DO model are a consequence of this technique neglecting the edge quality and with it connected localization of the non-equilibrium events. What we are essentially deducing from these models is an effective energy relaxation time.

BS model

To include overheating the curve derived from the BS model and described by the equations 2.14 was plotted and fitted to the measured data in the representation j^*/j_0 versus E^*/E_0. Whilst j_0 corresponds to the zero field j^* and can be approximated from the measurements, E_0 is the only fitting parameter. The fits can be seen as solid lines in 4.10 (b) for sample L and 5.6 (b) for sample F. Power can be calculated as a multiplication of the electric field E and the current density j. By plotting P^*/P_0 against B, we can fit to equation 2.20. The fitting parameter is the transition field B_T. Using equations 2.13 and 2.19, we obtain the value for τ_ϵ derived from the BS model. All obtained values can be found in the panels of the fits. As discussed in the previous chapter, the fit for sample L deviates a lot in the mid range to small magnetic fields. This deviation got worse for even thinner samples and somewhat better for thicker samples. Sample F has the same thickness as sample L, and we observe a very good fit. This is a huge indicator of the poor edge quality being the reason for the deviation from the BS theory. For sample L we have derived $\tau_\epsilon = 34.8$ ps and for sample F $\tau_\epsilon = 0.57$ ps. The transition field B_T of 80 mT suggests an important role of overheating for all fields above this field.

The equation 2.21 is used to determine τ_{ep} and the equation of the BS model from table

sample	E_0 [V/cm]	j_0 [mA/μm^2]	h [W/Kcm^2]	B_T [mT]	τ_{ep} [ns]	τ_{ee} [ps]
L	1.15	4.5	0.54	80	2.834	35.233
F	16	19.5	32.73	80	0.046	0.582

Table 5.1: Table contains results for the fitted electric field E_0, current density j_0, the heat transfer coefficient h, the transition field B_T, the electron-phonon relaxation time and the electron-electron relaxation time from the BS model for the 15 nm MoSi sample F and sample L.

2.1 to determine τ_{ee}. These estimates are made under the consideration that we are in the overheating regime described in the BS theory. The results of the BS model fitting can be found in table 5.1 and the results for τ_ϵ for all models to be compared with each other in the section summary table 5.2.

sample	τ_ϵ (LO) [ps]	τ_ϵ (DO) [ps]	τ_ϵ (BS) [ps]
L	277	650	35
F	2.68	17	0.57

Table 5.2: Table contains results for the fitted energy relaxation times τ_ϵ as found using the LO, DO and BS model for 15 nm MoSi films patterned with laser for sample L and with FIB for sample F.

Let us now look at the values obtained for τ_ϵ. At present it is not possible to deduce relaxation times from single-photon detection experiments directly, but a method deemed to produce successful results for the electron-phonon relaxation time τ_{ep} is measuring and analyzing magnetoconductance. We are not aware of any measurements on MoSi films, but we can compare our results to similar amorphous WSi films [108] and highly disordered polycrystalline granular NbN and NbTiN films [109, 110]. Here, τ_{ep} is listed with sub-100 ps values. Hence, we expect MoSi to also have τ_{ep} on the sub-100 ps time scale.

Looking back at table 2.1, we note that, while in the LO and DO models the obtained value of τ_ϵ is essentially the same as τ_{ep}. In the BS model, we must refer to the calculated τ_{ep} from table 5.1. τ_{ep} for sample L takes values of 277, 650 and 2834 ps in the LO, DO, and BS models, respectively. All of these values are highly overestimated compared to the expected value. We should also not forget how the experimental data were poorly described by these models, especially by the BS model. It is clear that the true intrinsic τ_{ep} is hidden by events not taken into account in the FFI derivation of τ_{ep}.

Meanwhile, τ_{ep} for sample F takes values of 2.68, 17 and 46 ps in the LO, DO, and BS models, respectively. Despite the large dispersion of the obtained values, they all fall into

the expected time scale. Since the BS model fits the data very well and takes into account both the dependency of v^* on B and overheating, we suspect the obtained value of 46 ps to be closest to the intrinsic τ_{ep}. It is important to stress that none of these models takes into account the local character of the FFI, but by fabricating a close-to-perfect edge, we have minimized the contribution of the otherwise strong symmetry breaking at the edge, which causes the FFI to nucleate sooner. According to the edge-controlled instability theory (2.3.2) even in sample F the FFI nucleates at the edge, but only once vortices with relatively high velocities move in the films interior. Nucleation due to high vortex velocity is also how the LO theory describes this nucleation. Hence, this explains why we obtain relatively accurate results using theories based on LO for sample F despite the lack of a local character description in these theories.

Lastly, we would like to add that the values of the BS model were calculated in the overheating regime. This regime takes place only when $l_{ep} \gg d_{eff}$, where $d_{eff} = d/\alpha$ and α is the mean probability of transmission of phonons from the superconducting film into the substrate. To ensure the overheating regime, the MoSi film was grown on top of a Si buffer layer. Their lattice matching should ensure a high enough α to justify an overheating regime for the thin films.

5.2.3 Numerical modeling

Further insights into the different processes occurring in the two samples is provided by solving the TDGL in conjunction with the heat balance equation. The modeling takes into account vortex-surface interactions. The simulation provides a spatial representation of the superconducting order parameter $|\Delta|$, as well as current voltage curves. Because exact modeling of the complicated edge structure of sample L was not possible, we have instead considered a sample with smooth edges with a single edge defect on one side of the sample. See figure 5.7 (a). A defect is simulated as a region in the simulation grid where the critical temperature is suppressed. Simply by switching the magnetic field direction, one can trigger vortex entry through the edge with the defect (panel A) or the smooth edge (panel A'). The panels are snippets in simulation time just before the FFI takes place, when current I^* flows through the sample. The value of I^* is different depending on the edge through which the vortices enter. In panel A the circulating currents avoid the defect by flowing around it. This causes current crowding just in front of it and lowers the vortex entry edge barrier. The defect becomes a preferred vortex entry point with larger Joule dissipation. Vortex rivers of self-organized Josephson-like junctions formed by fast-moving vortices appear. These junctions can evolve to normal domains and spread throughout the sample, changing the sample to the normal state, once the current density of the normal domain reaches values higher than J_P from section 2.3.2. The current crowding increases the normal domain current density and thus the switching to normal state happens at lower driving currents compared to the smooth edge. The simulated I-V curves can be seen in figure 5.7 (b). Apart from the shift of FFI to lower driving currents in the edge with defect, we also observe a shift to lower voltage.

Now this shift can be understood based on the considerations of pinning described in section 2.3.2. There, it was explained how a disordered motion resulting from randomly distributed defects leads to a lower mean velocity, and hence to a lower voltage. Similarly, here, we observe how the vortex rivers branch outward, causing a disordered motion. The branching occurs as a consequence of the circulating current being deflected from its direction along the straight edge and influencing the direction of the Lorentz force on the entering vortices. The disordered motion leads to the lower mean velocity.

In comparison in panel A' the circulating currents lower the edge barrier, but there is no preferred entrance site, as the height of the barriers will be the same throughout the edge. Vortex rivers are formed along the entire hot edge equally and allow vortices to flow in an ordered motion. The ordered motion allows us to measure a higher mean velocity (voltage) and due to the lack of current crowding at the entrance points, J_P (FFI) is reached only at a higher driving current. It should be noted that in the simulated sample A' the defect on the other side of the edge causes a faster development of the vortex river, but only for the rivers directly across the defect.

Figures 5.7 (c) and (d) show the branching of the vortex rivers for a triangle and a slit-shaped defect. Each case leads to a unique I-V coordinate of the FFI.

To take into account not only the change in edge shape, but also the observed change in composition along the edge after laser etching, a simulation was performed with randomly distributed defects of the size of $2\xi_c \times 2\xi_c$) in the close-to-edge region of width 25 ξ_c for the strip width of 100 ξ_c. Here $\xi_c = 7.8$ nm. We conclude that the results of this system are very similar to those without random defects, with suppression of V^* and I^* for the sample with a defect at the edge.

In the end, we would like to draw attention to the fact that although the simulations did predict lower V^* and I^* in the edge with defect, the difference is much smaller compared to what was found in the experiment. Our suspicion is that the spatial spread of the FFI in experiment differs from how it spreads in the simulations. Perhaps an adjustment of phonon escape times and of the so-called healing length (the length it takes hot electrons to diffuse to neighboring regions) in simulation might get us closer to what we see in experiments. The simulation also only works with a single defect, whilst in experiment we have defects across the entire length of the edge. More investigations should follow.

5.3 Conclusion

In conclusion we have seen that the smooth edges left after FIB patterning lead to (i) at least twice as high zero-field critical current, (ii) a factor of 20 enhancement of the maximal vortex velocity up to about 20 km/s, and (iii) at least a factor of 40 smaller estimate for the electron-phonon relaxation time on the sub-50 ps time scale. Systems with high zero-field critical currents and low electron-phonon relaxation times are very relevant for use in SSPDs. The difference in the properties caused by the fabrication is especially important for

SMSPDs, where the detection voltage is raised because of fast moving vortices around a hot spot. The found increase in velocity can be exploited for studies of otherwise inaccessible regimes, where fast-moving vortices can generate sound and/or spin waves, with rich physics of fluxon-phonon and fluxon-magnon interactions. Our study showed the lack of a model for analyzing thin-film FFI data to gain information about the intrinsic energy relaxation times. Instead, if no care for the edge quality is taken, we can only talk about some 'indicative' relaxation time that exceeds the intrinsic τ_ϵ in the material. All findings are summarized in the bibliography entry [111].

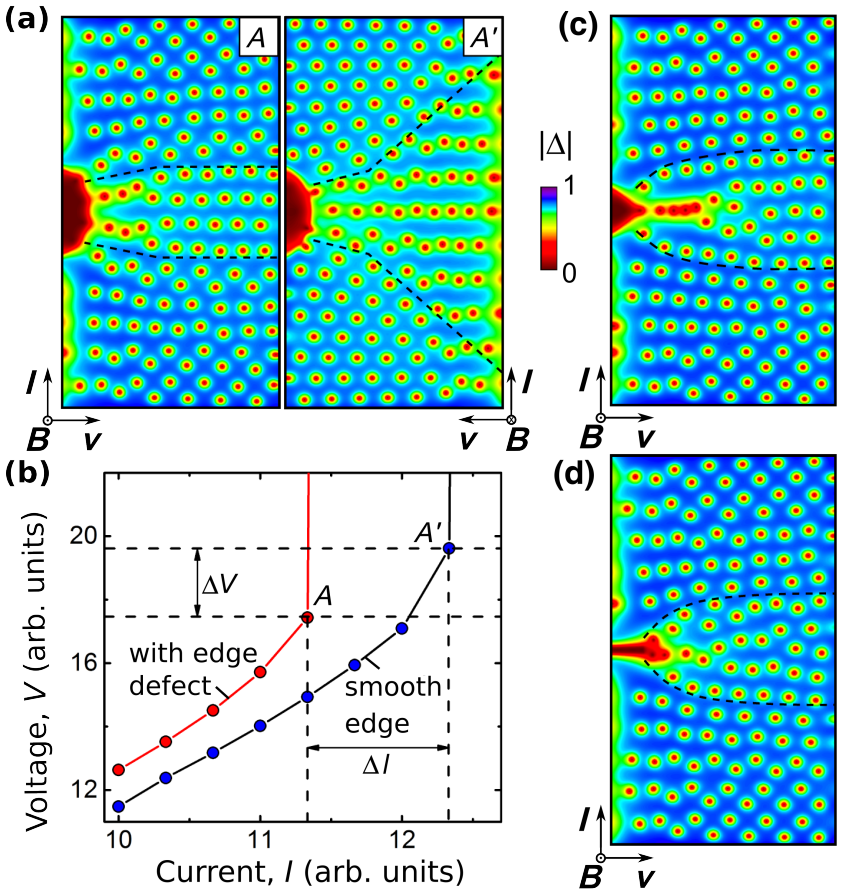

Figure 5.7: Snapshots of the superconducting order parameter $|\Delta|$ in a strip with a half-circle defect on one side are shown for two magnetic field orientations and at two different current values at $T = 0.8\ T_C$. Entrance through side with edge defect, I /I_{dep} = 0.34 and B = 245mT is shown in panel A. Entrance through smooth edge, I /I_{dep} = 0.37 and B = -245mT in panel A'. The current values in A and A' correspond to the current values in the points A and A' in the simulated I-V curve in (b) for entrance through side with defect and entrance through smooth side. Dashed lines demarcate the regions of nucleation and evolution of vortex rivers. Further are shown examples of nucleation of vortex jets upon vortex entry through a triangular shaped defect (c) and a narrow slit (d).

Chapter 6

Vortex jets and vortex counting

This last chapter is devoted to two more observed phenomena connected to vortex dynamics. The author of this thesis was not the main researcher and contributor to these works but rather contributed with discussions and some additional simulations supporting the found phenomena. Therefore, here we will only provide a brief summary of these works, as the main attention of this thesis is given to the previous chapters.

6.1 Vortex jets

6.1.1 Qualitative consideration and analytical theory

When describing the figure 5.7 we have commented on how the vortex rivers fanned out around the defect due to the deflection of the circulating current around the defect that changes the Lorentz force direction in this area. Further away from the defect at this magnetic field value, however, the vortex-vortex repulsion acting from all sides, due to the large number of vortices, is recovering the Abrikosov ordering. Now, if we observe very narrow defects (slits), the current crowding effect is strongly located at the tip of the defect, where the Lorentz forces direction is unchanged. At a magnetic field of very low values, or even zero, we obtain a state where all existing vortices are entering strictly through the tip of the defect and their movement direction gives us access to observe one-on-one vortex-vortex repulsion unaffected by the fanning out due to circulating currents. The repulsion opens up a jet of vortices, which is narrow at the defect and expands as the vortices travel to the opposite side. This leads to a measurable transverse voltage $V_\perp$. The geometry of such an experiment can be seen in figure 6.1. By patterning voltage pairs, with one on the edge of where the defect is and one on the edge across the defect, at different distances l from the defect line (y=0), we can gain information about the opening width of the jet. In the figure, the transverse voltage can be measured using the voltage pair $V_1 - V_2$, whilst for regular voltage the pair $V_3 - V_4$ can be used.

If the width of the defect is larger than ξ, several vortex chains can form and open a jet due to vortex chain repulsion. In the case where the width of the defect is approximately the

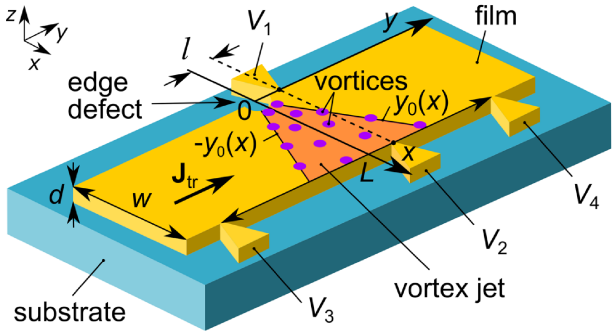

Figure 6.1: Geometry of the bridge for vortex jet and transverse voltage measurements. Origin of the coordinates is at the edge defect. The outer edge of the vortex jet lays at $\pm y_0(x)$. Transverse voltage is measured by the $V_1 - V_2$ voltage pair, whilst for regular voltage is used the $V_3 - V_4$ pair.

size of ξ, the vortices will enter the strip consequentially. A vortex should follow the wake (left behind track with suppressed superconductivity) of the vortex in front of it, but due to fluctuations and inhomogeneities the vortex can escape the wake, and the vortex-vortex repulsion will push it away from the vortex infront of it creating a jet. The width of the jet depends on the distance from the defect in the x direction and is equal to $2y_0$(x). $y_0(x)$ describes the outer edge of the jet (see the description in figure 6.1). $y_0(x)$ and the defect line form the angle α_0, the maximum deflection angle.

The trajectory of vortices results from the competing vortex-vortex, transport-current-vortex, and edge barrier interaction. For vortices to enter in the first place, the transport current I_{tr} must be larger than I_B, a current at which the edge barrier is broken. For I_{tr} close to I_B, the edge barrier is also locally recovered when a vortex enters the sample. The supercurrent circulating around the vortex is directed oppositely to I_{tr} and thus prevents an immediate penetration of another vortex.

Bezuglyj and Shklovskij solved equations of motion similar to the Langevin equation 2.8. As a result they found the analytical expression for the vortex jet outer shape in a narrow strip ($\xi \ll w \lesssim 2\Lambda$):

$$y_0(x) = \frac{f_V w^2 c^2 \eta}{4\pi\Lambda(I_{tr} - I_B)^2}\, x. \tag{6.1}$$

Here, f_V is the frequency of penetration into the strip through the defect. For details of the calculation and also results for a wide strip, please refer to the bibliography entry [112].

To give the analytical expression for the transverse voltage, let us first explain where the voltage comes from. When a vortex crosses the superconductor stretched between a voltage pair, it acts as a weak link. The voltage in that moment can therefore be calculated using the second Josephson equation: $V = \hbar/2e\ d\varphi/dt$. φ is here defined as the difference in the superconducting phase ϕ before and after the vortex. A single vortex changes the phase by 2π. The phase difference in time is thus $2\pi f$, where f is the frequency with witch a

vortex crosses the line connecting the voltage leads. Putting all the expressions together and substituting in for the magnetic quantum (2.2) gives:

$$V = \Phi_0 f. \tag{6.2}$$

To calculate the transverse voltage specifically we substitute the frequency f in the equation with the frequency with which a vortex crosses the line connecting the voltage leads V_1 and V_2. Considering that consecutive vortices entering the sample are deflected in opposite directions, only half of all entered vortices will be deflected in the direction of the $V_1 - V_2$ line, and from these only the vortices deflected under an angle larger than $\alpha = \arctan(l/w)$ will actually cross the $V_1 - V_2$ line. We can therefore calculate the frequency of entry through the $V_1 - V_2$ line with

$$f_\perp = \frac{f_V}{2} \frac{(\alpha_0 - \alpha)}{\alpha_0}. \tag{6.3}$$

Lastly, we obtain the transverse voltage as follows:

$$V_\perp = \frac{\Phi_0 f_V}{2} \frac{(\alpha_0 - \alpha)}{\alpha_0} \tag{6.4}$$

and for a narrow strip, using equation 6.1 and $y_0(x) = \alpha_0 x$ to define α_0, we obtain:

$$V_\perp(I_{tr}) = \frac{\Phi_0 f_V}{2} \left(1 - \frac{4\pi\Lambda l (I_{tr} - I_B)^2}{c^2 w^3 \eta_0 f_V}\right). \tag{6.5}$$

The found transverse voltage expression is dependent on the penetration frequency f_V. It was previously experimentally observed that for an edge defect in form of a narrowing of the film this frequency is proportional to $(I_{tr} - I_B)$ [24]. The exact proportionality factor is though not yet found.

6.1.2 Experiment

The measured samples were 15-nm thick MoSi samples of 1 μ m width. This width categorizes the samples as narrow strips (refer to the values in table 4.2). The film preparation method is the same as in 4.1. The samples were patterned using FIB milling to produce smooth edges and a pair of voltage leads (V_1 and V_2) for transverse voltage measurements. On one side of all films an artificially created edge defect of length about 20 nm was milled out. The samples differentiate in distance l. The samples produced were samples with l = 16, 32, 48, 80 nm. The samples are labeled accordingly by their l value. A control sample without a notch was also produced and is labeled as sample A.

The transverse voltage I-V curves for all samples are presented in figure 6.3 (a). In all samples with a notch, the transverse voltage starts to increase once $I_B = 153$ μ A is reached. Afterwards, the shape of the dependency on I_{tr} is generally the same for all samples. We see dome-shaped dependencies. The maximum of the dome and its width is lower for larger l. This is because the farther away from the defect line we measure, the smaller

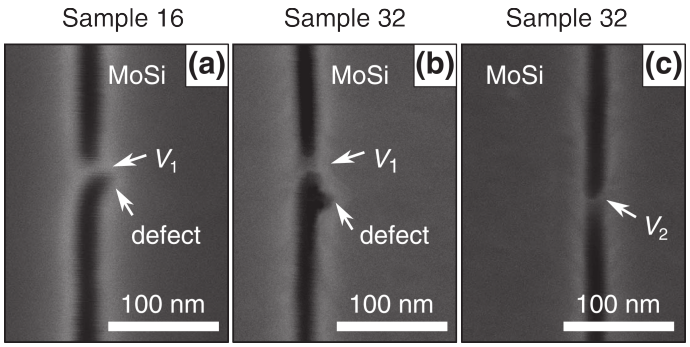

Figure 6.2: SEM images of the artificially created notch (defect) for sample 16 (a) and sample 32 (b). Panel (c) is a SEM image of the opposite edge of sample 32. Transverse voltage was measured using voltage leads V_1 and V_2.

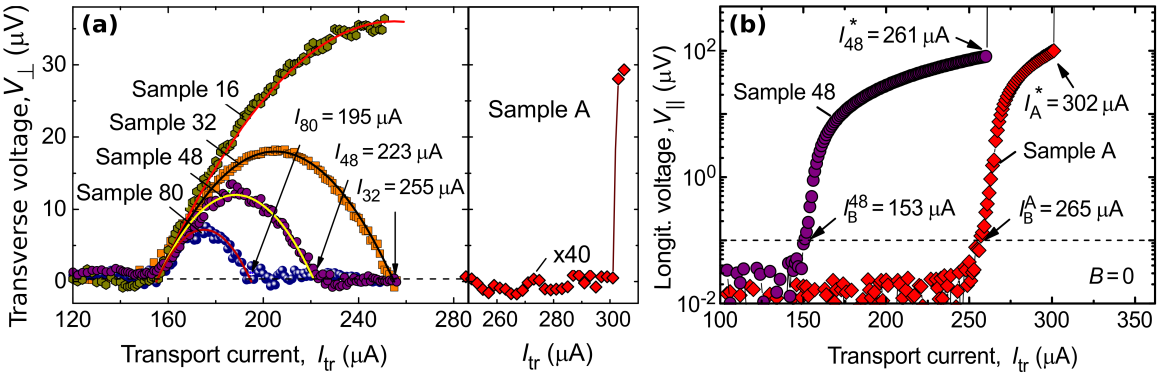

Figure 6.3: Transverse I-V curves for all samples with and without an edge defect (a). Symbols are experimental data points and solid lines are fits to equation 6.5. The voltage of sample A is multiplied with a factor of 40. In panel (b) are longitudinal I-V curves for sample 48 and sample A. Dashed line indicates the 0.1-μV voltage criterion used for the determination of the critical current I_B. In all panels T = 5 K and B = 0.

will be the number of vortices deflected all the way to this region. The dome shape also suggests that the jet angle is opening at the beginning and then closing again as I_{tr} is raised. In sample 16, which is in direct proximity to the notch, we observe a transverse voltage maximum at about 261 μA followed by a jump to 55 μV. 261 μA is where the sample undergoes an FFI. The domes can be fitted by the equation 6.5 written in compact form as $V_\perp(I_{tr}) = A_1(I_{tr} - I_B) - \alpha B_1(I_{tr} - I_B)^2$. The best fits were obtained for $A_1 = (0.75 \pm 0.03)$ V/A and $B_1 = (225 \pm 5)$ mV/mA^2. The fits are seen as solid lines in panel (a).

To compare these results, we have a look at sample A, where we measure transverse voltage below 100 nV, and that even after crossing I_B (observed in figure 6.3 (b)). Without the notch, vortices can enter further apart from each other on the entire length of the edge and will not strongly influence each others trajectory. At 302 μA, where the sample undergoes a FFI, a jump to a higher resistive state occurs.

The longitudinal voltage I-V curves for sample 48 and sample A can be found in 6.3 (b). Here, we observe the same I_B and I^* values as seen in the transverse measurements. The dashed line indicates the 0.1-μV voltage criterion used for the determination of the critical current I_B.

6.1.3 Numerical modeling

The TDGL in conjunction with the heat balance equation provided us with snapshots of the spatial distribution of the superconducting order parameter. This allows us to analyze the vortex patterns, and the results explain the measured transverse voltage. Modeled was a sample with an edge defect placed in a very weak magnetic field. The defect in the simulation is a slit with locally suppressed T_C. The size of the defect is $15\xi_c \times 2\xi_c$ and the width of the strip is 100 ξ_c. Here $\xi_c = 7.8$ nm. The figure 6.4 depicts snapshots of the order parameter for a current increase in the units of the depairing current I_{dep}. The dashed line corresponds to the place where the transverse voltage could be measured (the $V_1 - V_2$ line). As the current increases above I_B, vortices start to enter and form a divergent jet with two arms because of the vortex-vortex repulsion. The increasing current increases not only the frequency with which the vortices enter the sample but also the angle between the two arms of the jet. At some point though, the current-vortex interaction overpowers the vortex-vortex interaction, and the two arms of the jet start to collapse and form a vortex line and later a vortex river.

A non-zero transverse voltage is only registered when a vortex crosses the dashed line. Its value depends on the frequency with which vortices cross it. Hence, the transverse voltage dependency on transport current observed from the snapshots agrees well with the dome-shaped dependence of transverse voltage from the experiment.

Simulations at various weak external magnetic fields lead to similar results with only a difference in the number of vortices in the vortex jet arms. However, simulations in zero magnetic field failed to reproduce vortex jets. As mentioned above, a vortex jet is formed only in the presence of some fluctuations and inhomogeneities. Whilst these are unavoidable in experiment, in simulation, these have to be introduced manually. In weak external magnetic field, the vortices already present in the sample will play the role of fluctuations.

6.1.4 Conclusion

Combining theory, experiment, and numerical modeling we have shown the appearance of transverse voltage for narrow strips with a narrow slit edge defect in weak magnetic fields. The transverse voltage is attributed to opening of a vortex jet as a result of the one-on-one vortex-vortex interaction.

6.2 Vortex counting

Throughout this thesis, we have used the relation $v^* = V^*/Bl$ to calculate the maximal vortex velocity. Often we were forced to omit data points for very low magnetic fields, as these lead

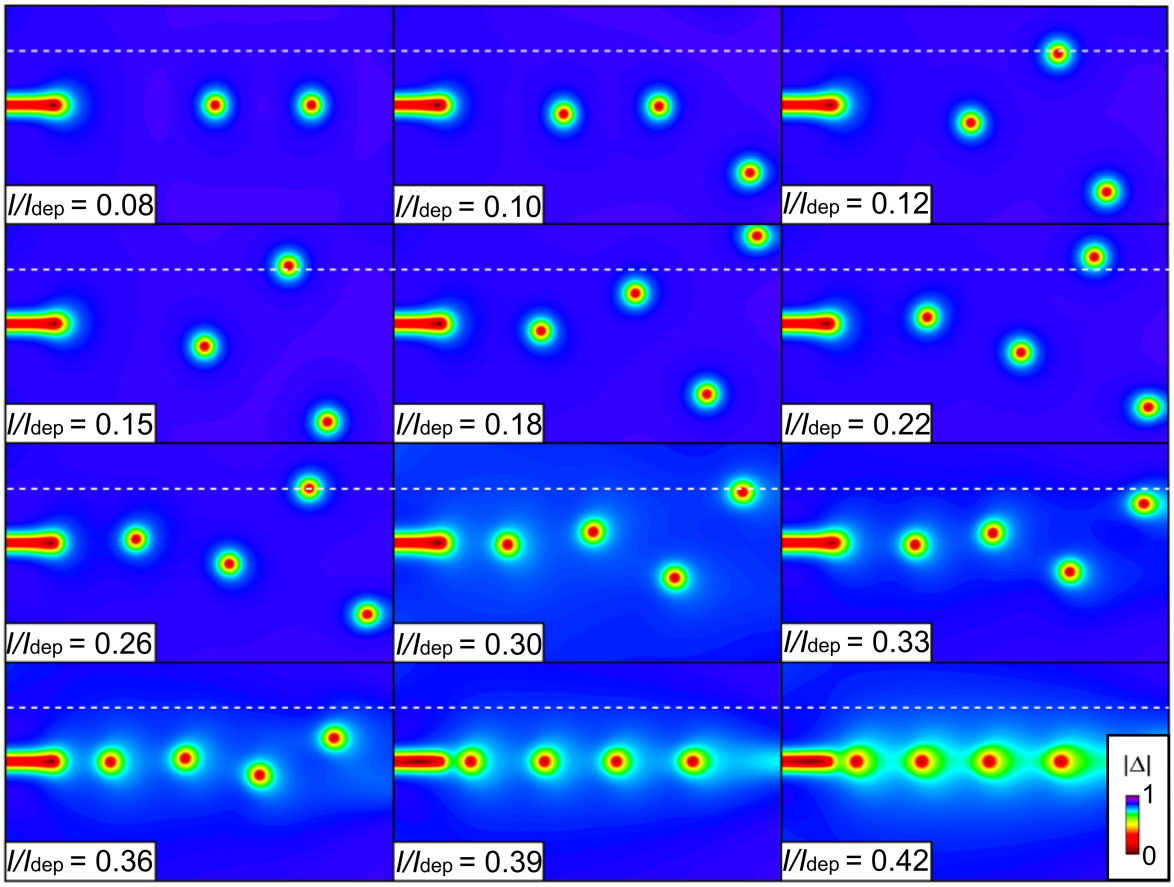

Figure 6.4: Snapshots of the superconducting order parameter $|\Delta|$ for a series of current values, as indicated. Observed is the vortex trajectory evolving from straight line to jet and lastly just before the FFI to a vortex river. The horizontal dashed lines indicate the location of the transverse voltage leads.

to unphysically large values. An explanation of these values comes from the assumption that has been taken in equation 2.9. There, the in-sample induced magnetic field B is considered to be the same as the external applied magnetic field B_{ext}. The induced magnetic field in a sample is equal to

$$B = N\Phi_0/S, \tag{6.6}$$

where N is the number of vortices in the sample and S is the sample area ($=wl$). If we set $B = B_{ext}$, the number of vortices N is equal to the number of vortices induced by external magnetic field. Although this might be acceptable for larger magnetic fields, in small magnetic fields, where the number of vortices in the sample induced by the flowing current as opposed to the external magnetic field is dominant, this assumption can no longer be taken into account. We could try to calculate the self-field for geometry-dependent non-uniform current distributions, but this is a very complex problem. Instead, setting equation 6.6 into equation

2.9, we obtain a new expression to calculate the velocity without the need for B:

$$v = \frac{Vw}{N\Phi_0}. \tag{6.7}$$

The obvious problem with this equation is the unknown number of vortices N present in the sample.

The idea of a method for counting the number of vortices in a sample without the need for direct observation came from the work of Aslamazov and Larkin (AL) [34]. They predicted the appearance of kinks in I-V curves of wide and short constrictions whenever the number of vortices crossing the construction is increased by one. These kinks appear as a result of the vortex-vortex interaction. As mentioned above, a vortex that has entered the sample prevents an immediate penetration of another vortex due to a local recovery of the edge barrier. If we have only one vortex moving in the sample, a second vortex at this transport current value can enter only once the first vortex has crossed the bridge. The number of vortices at all times in the sample is thus only one. If we now raise the transport current, it comes to a point that the edge barrier is overcome, and a vortex can enter the sample even before the first disappears on the other end of the bridge. At this point, we have two vortices present in the sample at the same time, but also a stronger recovery of the edge barrier now mediated by two vortices. This causes sharp bends in the I-V curve whenever N is increased. By counting the number of discontinuities, we obtain N.

6.2.1 Experiment

In the experiment, the conditions for such observation were realized in two 15-nm thick MoSi samples of 2 μm width. The preparation method is the same as in 4.1. The samples were patterned again using FIB milling. FIB milling was also used to make long narrow slits of length l_S. Because the slits are now long compared to the sample width, the w from equation 6.7 is the isthmus length ($=w - l_S$).

We can see the I-V curve of a sample with a slit of $l_S = 0.2$ μm in figure 6.5 (a) at a zero applied magnetic field. Indeed, observed were predicted kinks. The first kink voltage is at V_1 = 9.8 μV, and then five more voltage kinks can be recognized in the I-V curve and even more so in the differential resistance curve shown in 6.5 (b).The curves end with an FFI jump to the highly resistive state at $V^* = 69.2$ μV. An important difference from what was described in the AL paper [34] is found in the voltage spacing of the kink discontinuities. Whilst in the AL paper the kinks appear with a constant voltage spacing, we have observed the voltage spacing to grow with each kink. We assume that this difference is caused by a formation of a diverging jet in the experiment, whilst in theory the vortices are predicted to move on a straight line. We have simulated that a straight line movement at all transport currents is expected for a double-sided slit, which is similar to the constrictions considered in the AL paper. In figure 6.6 we add a comparison of the trajectories of vortices for a single slit (a) and a double-sided slit (b). A more detailed description of the increase voltage spacing, as

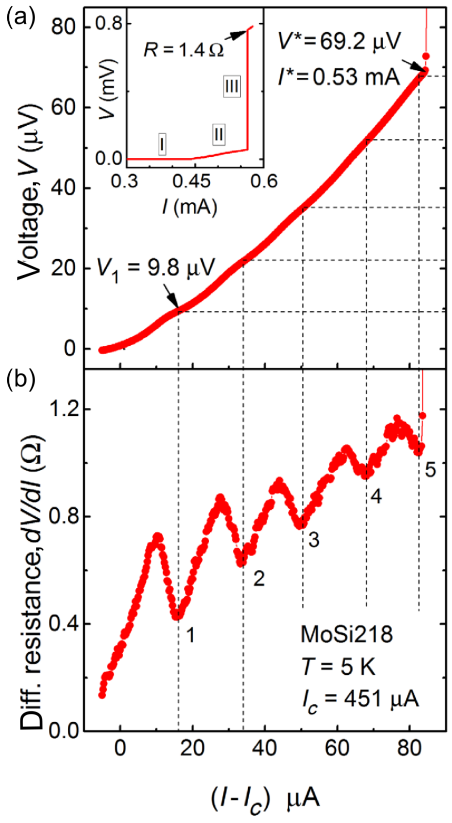

Figure 6.5: AL predicted kinks in the I-V curves of a strip with a slit of $l_S = 0.2$ μm at $T = 5$ K (a). The inset is of the same curve in a broader range of currents. (b) is the current dependence of the differential resistance for the same sample.

well as the TDGL simulation of this geometry that predicts these not constantly separated voltage kinks, can be found in [113].

6.2.2 Conclusion

In conclusion, we have described and proved a method to count vortices in order to calculate the velocities of vortices in low and zero magnetic fields with equation 6.7. It should be noted that we obtain the same equation by deriving it from the Josephson equation 6.2 that we used in the previous section. In this equation, the frequency with which a vortex crosses the voltage pair line is equal to the number of vortices that cross it per a certain time value, or N_V/t. In the time a single vortex crosses from one side to the other, the number of vortices crossing through the voltage pair line is the same as the number of vortices present in the sample when our vortex arrives to the other end. In other words $N_V = N$ when t is the time a vortex needs to cross the distance w with speed $v(= w/t)$. The Jospehson equation is then $V = \Phi_0 N v/(w)$, which is the same as equation 6.7 obtained by electric field generation consideration. Lastly, counting the number of discontinuities in the I-V curves of slitted bridges provides us with the otherwise unknown number N.

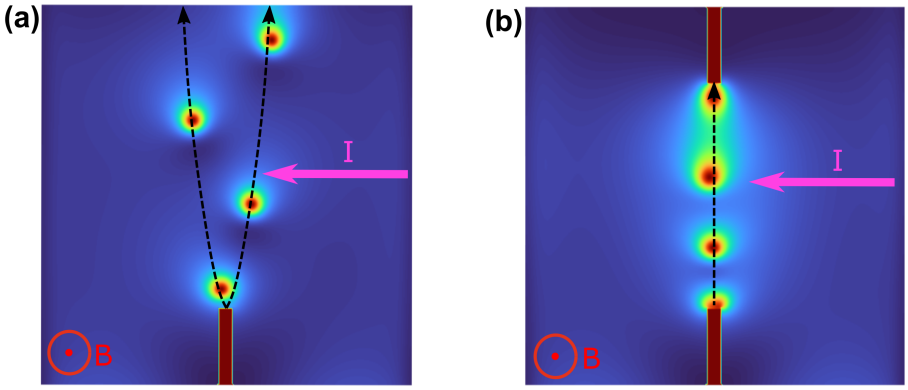

Figure 6.6: Snapshot of the superconducting order parameter $|\Delta|$ for a single slit (a) and a double sided slit (b) for the same transport current and field values.

Chapter 7

Conclusions and outlook

In this thesis we have observed and described non-equilibrium phenomena, namely the FFI, to learn more about the vortex dynamics and the energy relaxation processes. Studied were amorphous MoSi and polycrystalline Nb thin films of various thicknesses. We have observed that although most of the superconducting parameters showed the same thickness dependence in both crystallization systems, the transition width and critical field did not. Especially, the critical field dependence upon thickness for different crystallization remains rather unclear and requires further studies on a larger batch of samples. For application in SSPDs we are interested in materials with low values of τ_ϵ and D, but large values of critical parameters. As the film thickness goes down, in both crystallization systems, superconducting critical parameters degrade, but the energy relaxation time and the diffusion constant improve. Hence, from FFI studies, middle range thicknesses look promising for detectors. The energy relaxation time τ_ϵ for MoSi and Nb is very similar, but the energy diffusion constant D in MoSi is at least half of the one found for Nb, which makes MoSi a superior candidate for use in SSPDs.

In the same thickness study, we have seen the lack of FFI models that would properly replicate thin film experimental I-V data. These models did not fit the thinnest of samples completely, but showed a bit of improvement in fitting the thicker films. This is a sign of the existence of an effect that causes the deviation from the known models, and this effect to be more prominent in thinner samples. Triggered by the work of Vodolazov on the edge-controlled instability model, we have assumed that the effect we are encountering is a local FFI at the edge of the sample. A local FFI is not taken into account in any of the fitted models (LO, DO or BS), but the edge-controlled instability model, which assumes a local FFI, does not provide us with a tool to extract the energy relaxation time. In order to test if our assumption that the fitting models deviate from experimental data due to the lack of consideration of a local FFI, we have created a system where we assume the local FFI to be suppressed and checked if now the models show an improvement in fitting. We have fabricated two MoSi samples with rough and smooth edges. The rough edge was fabricated using laser beam etching, whilst the smooth edge was milled by a FIB. A smooth edge should

reduce the occurrence of local FFI at the edge of the sample. As a result, films with smooth edges lead to between 10 to 20 times larger v^*, a factor of 3 larger critical currents, and a factor of couple tenths shorter relaxation times. All these changes are remarkable for the SSPD industry as it shows that the fabrication method alone can improve their detection capabilities. The improvements are a direct consequence of the suppression of the local FFI in the smooth-edged sample that otherwise triggers an instability at lower currents and voltages. The sample with the smooth edge further showed an improvement in fitting the non-local FFI models. This means that non-local FFI models can only provide us with some indicative relaxation times that exceed the intrinsic relaxation time. We consider as the most reliably extracted, and closest to an intrinsic value, electron-phonon relaxation time for the 15 nm MoSi, the result obtained by fitting the BS model to data from the smooth-edged sample, with $\tau_\epsilon = 46$ ps. This result is also in line with the results of the electron-phonon relaxation times obtained from magnetoconductance measurements that suggest sub-100-ps values.

Further, we have observed unphysically large v^* at low magnetic fields that cannot be explained by local phenomena. This was explained by a falsely assumed number of vortices in the samples at these low fields. A technique based on the work of Aslamazov and Larkin to count vortices in slitted superconductors was shown. By simply counting the number of appeared kinks in their I-V curves, one obtains the number of vortices. The velocity can then be calculated with the newly defined equation 6.7.

In slitted superconductors the votex dynamics was also of interest. Analytical expressions and experimental data for transverse voltage confirmed numerically predicted trajectories. The trajectories start as a 1D-line and turn into vortex jets. At high currents they collapse back to a vortex river.

The results described and analyzed in this thesis have provided us with new information about how to analyze I-V measurements and have shown us some new interesting vortex dynamics. The future of vortex dynamics lies in exploring the third dimension as a result of the growing advancements in the fabrication techniques. In order to successfully understand and analyze these complex structures, it is important to understand and solve the one-dimensional problems.

Bibliography

[1] Kamerlingh Onnes, H. *Leiden Comm. 122b Proc.* **14,** 113–115 (1911).

[2] Wilson, M. N. Superconducting Magnets. *Oxford University Press* (1983).

[3] Liu, J. *et al.* World record 32.35 tesla direct-current magnetic field generated with an all-superconducting magnet. *Supercond. Sci. Technol.* **33,** 03LT01 (2020).

[4] Bernstein, P. & Noudem, J. Superconducting magnetic levitation: principle, materials, physics and models. *Supercond. Sci. Technol.* **33,** 033001 (2020).

[5] Josephson, B. D. Possible new effects in superconductive tunnelling. *Phys. Lett.* **1,** 251–253 (1962).

[6] Taylor, B. N., Parker, W. H., Langenberg, D. N. & Denenstein, A. On the use of the AC Josephson effect to maintain standards of electromotive force. *Metrologia* **3** (1967).

[7] Field, B. F., Finnegan, T. F. & Toots, J. Volt maintenance at NBS via 2e/h: A new definition of the NBS Volt. *Metrologia* **9** (1973).

[8] Doll, R. & Näbauer, M. Experimental proof of magnetic flux quantization in a superconducting ring. *Phys. Rev. Lett.* **7** (1961).

[9] B. S. Deaver, J. & Fairbank, W. M. Experimental evidence for quantized flux in superconducting cylinders. *Phys. Rev. Lett.* **7** (1961).

[10] Gallop, J. C. & Petley, B. W. Squids and their applications. *J. Phys. E: Sci. Instrum.* **9** (1976).

[11] Kadin, A. M. & Johnson, M. W. Nonequilibrium photon-induced hotspot: A new mechanism for photodetection in ultrathin metallic films. *Appl. Phys. Lett.* **69,** 3938–3940 (1996).

[12] Shubnikov, L. V., Khotkevich, V. I., Shepelev, Y. D. & Ryabinin, Y. N. Magnetic properties of superconductors and alloys. *Zh. Eksper. Teor. Fiz.* **7,** 221–237 (1937).

[13] Abrikosov, A. A. On the magnetic properties of superconductors of the second group. *Sov. Phys. JETP.* **5,** 1174–1182 (1957).

[14] Kim, Y. B., Hempstead, C. F. & Strnad, A. R. Flux-flow resistance in type-II superconductors. *Phys. Rev.* **139,** A1163–A1172 (4A 1965).

[15] Anderson, P. W. & Kim, Y. B. Hard superconductivity: Theory of the motion of Abrikosov flux lines. *Rev. Mod. Phys.* **36,** 39–43 (1964).

[16] Larkin, A. I. & Ovchinnikov, Y. N. Nonlinear conductivity of superconductors in the mixed state. *J. Exp. Theor. Phys.* **41,** 960 (1975).

[17] Jin, B. B. *et al.* High-frequency vortex ratchet effect in a superconducting film with a nanoengineered array of asymmetric pinning sites. *Phys. Rev. B* **81,** 174505–1–7 (2010).

[18] Silhanek, A. V., Van de Vondel, J. & Moshchalkov, V. V. Guided vortex motion and vortex ratchets in nanostructured superconductors. *Nanoscience and Engineering in Superconductivity,* 1–24 (2010).

[19] Wördenweber, R., Hollmann, E., Schubert, J., Kutzner, R. & Ghosh, A. K. Pattern induced phase transition of vortex motion in high-Tc films. *Appl. Phys. Lett.* **94** (2009).

[20] Dobrovolskiy, O. V. & Huth, M. Dual cut-off direct current-tunable microwave low-pass filter on superconducting Nb microstrips with asymmetric nanogrooves. *Appl. Phys. Lett.* **106,** 142601–1-5 (2015).

[21] A. M. Troyanovski J. Aarts, P. H. K. Collective and plastic vortex motion in superconductors at high flux densities. *Nature* **399,** 665–668 (1999).

[22] Keay, J. C. *et al.* Sequential vortex hopping in an array of artificial pinning centers. *Physical Review B* **80,** 165421 (2009).

[23] Goa, P. E. *et al.* Real-time magneto-optical imaging of vortices in superconducting $NbSe_2$. *Supercond. Sci. Technol.* **14,** 729 (2001).

[24] Embon, L. *et al.* Imaging of super-fast dynamics and flow instabilities of superconducting vortices. *Nat. Commun.* **8,** 85 (2017).

[25] Ivlev, B. I., Mejía-Rosales, S. & Kunchur, M. N. Cherenkov resonances in vortex dissipation in superconductors. *Phys. Rev. B* **60,** 12419–12423 (1999).

[26] Bulaevskii, L. N. & Chudnovsky, E. M. Sound generation by the vortex flow in type-II superconductors. *Phys. Rev. B* **72,** 094518 (2005).

[27] Shekhter, A., Bulaevskii, L. N. & Batista, C. D. Vortex viscosity in magnetic superconductors due to radiation of spin waves. *Phys. Rev. Lett.* **106,** 037001 (2011).

[28] Bespalov, A. A., Mel'nikov, A. S. & Buzdin, A. I. Magnon radiation by moving Abrikosov vortices in ferromagnetic superconductors and superconductor-ferromagnet multilayers. *Phys. Rev. B* **89,** 054516 (2014).

[29] Vodolazov, D. Y. Single-photon detection by a dirty current-carrying superconducting strip based on the kinetic-equation approach. *Phys. Rev. Appl.* **7,** 034014 (2017).

[30] Korneeva, Y. *et al.* Different single photon response of wide and narrow superconducting MoSi strips. *Phys. Rev. Appl., accepted for publication* (2020).

[31] Klapwijk, T. M. & Semenov, A. V. Engineering physics of superconducting hot-electron bolometer mixers. *IEEE Transactions on Terahertz Science and Technology* **7,** 627–648 (2017).

[32] Semenov, A. D. & Hübers, H.-W. Bandwidth of a hot-electron bolometer mixer according to the hot-spot model. *IEEE Transaction on Applied Superconductivity* **11,** 196–199 (2001).

[33] Vodolazov, D. Y. Flux-flow instability in a strongly disordered superconducting strip with an edge barrier for vortex entry. *Supercond. Sci. Technol.* **32,** 115013 (2019).

[34] Aslamazov, L. G. & Larkin, A. I. Josephson effect in wide superconducting bridges. *Zh. Eksp. Teor. Fiz.* **68,** 766–775 (1975).

[35] Kamerlingh Onnes, H. Leiden Comm. 120b. *Proc.* **13,** 1274–1276 (1911).

[36] Bardeen, J., Cooper, L. N. & Schrieffer, J. R. Microscopic theory of superconductivity. *Phys. Rev.* **106,** 162–164 (1957).

[37] Meissner, W. & Ochsenfeld, R. Ein neuer Effekt bei Eintritt der Supraleitfähigkeit. *Die Naturwissenschaften* **21,** 787–788 (1933).

[38] London, F. & London, H. The electromagnetic equations of the supraconductor. *Proc. Roy. Soc. A* **149,** 71–88 (1935).

[39] Ginzburg, V. L. & Landau, L. D. On the theory of superconductivity. *Zh. Eksper. Teor. Fiz.* **20,** 1064–1982 (1950).

[40] Romijn, J., Klapwijk, T. M., Renne, M. J. & Mooij, J. E. Critical pair-breaking current in superconducting aluminum strips far below T_c. *Phys. Rev. B* **26,** 3648–3655 (1982).

[41] Anderson, P. W. Theory of flux creep in hard superconductors. *Phys. Rev. Lett.* **9,** 309–311 (1962).

[42] Castro, J. I. & Lopez, A. Comments on the force on pinned vortices in superconductors. *Journal of Low Temperature Physics* **135** (2004).

[43] Bardeen, J. & Stephen, M. J. Theory of the motion of vortices in superconductors. *Phys. Rev.* **140,** A1197–A1207 (4A 1965).

[44] Larkin, A. I. & Ovchinnikov, Y. N. Pinning in type II superconductors. English. *J. Low Temp. Phys.* **34,** 409–428 (3-4 1979).

[45] Bean, C. P. & Livingston, J. D. Surface barrier in type II superconductors. *Phys. Rev. Letters* **12** (1964).

[46] Tinkham, M. Viscous flow of flux in type-II superconductors. *Phys. Rev. Lett.* **13,** 804–807 (1964).

[47] Gorkov, L. & Eliashberg, G. M. Generalization of the Ginzburg-Landau equations for non-stationary problems in the case of alloys with paramagnetic impurities. *Soviet Phys. JETP* **27,** 328 (1968).

[48] Kramer, L. & Watts-Tobin, R. J. Theory of dissipative current-carrying states in superconducting filaments. *Phys. Rev. Lett.* **40,** 1041–1044 (1978).

[49] Vodolazov, D. Y. & Peeters, F. M. Rearrangement of the vortex lattice due to instabilities of vortex flow. *Phys. Rev. B* **76,** 014521–1–9 (2007).

[50] Grimaldi, G. *et al.* Speed limit to the Abrikosov lattice in mesoscopic superconductors. *Phys. Rev. B* **92,** 024513 (2015).

[51] Glazman, L. I., Dmitrenko, I. M., Tovazhnyanskii, V. L., Fogel, N. Y. & Cherkasova, V. G. Critical fields of V/Si superlattices. *Sov. Phys. JETP.* **65,** 821 (1987).

[52] Larkin, A. I. & Ovchinnikov, Y. N. Nonequilibrium superconductivity. *Elsevier,* 493 (1986).

[53] Gurevich, A. & Ciovati, G. Dynamics of vortex penetration, jumpwise instabilities, and nonlinear surface resistance of type-II superconductors in strong rf fields. *Phys. Rev. B* **77,** 104501 (2008).

[54] Klein, W., Huebener, R. P., Gauss, S. & Parisi, J. Nonlinearity in the flux-flow behavior of thin-film superconductors. *J. Low Temp. Phys.* **61,** 413–432 (1985).

[55] Bezuglyj, A. & Shklovskij, V. Effect of self-heating on flux flow instability in a superconductor near T_c. *Physica C* **202,** 234 (1992).

[56] Shklovskij, V. A. Hot electrons in metals at low temperatures. *J. Low Temp. Phys.* **41,** 375–396 (1980).

[57] Doettinger, S., Huebener, R. & Kühle, A. Electronic instability during vortex motion in cuprate superconductors Regime of low and high magnetic fields. *Physica C* **251,** 285–289 (1995).

[58] Grimaldi, G. *et al.* Evidence for low-field crossover in the vortex critical velocity of type-II superconducting thin films. *Phys. Rev. B* **82,** 024512 (2010).

[59] Silhanek, A. V. *et al.* Influence of artificial pinning on vortex lattice instability in superconducting films. *New J. Phys.* **14,** 053006 (2012).

[60] Shklovskij, V. A., Nazipova, A. P. & Dobrovolskiy, O. V. Pinning effects on self-heating and flux-flow instability in superconducting films near T_c. *Phys. Rev. B* **95,** 184517 (2017).

[61] Bezuglyj, A. I. *et al.* Local flux-flow instability in superconducting films near T_c. *Phys. Rev. B* **99,** 174518 (2019).

[62] Gurevich, A. V. & Mints, R. G. Localized waves in inhomogeneous media. *Sov. Phys. Usp.* **27,** 19 (1984).

[63] Dobrovolskiy, O. V. *et al.* Ultra-fast vortex motion in a direct-write Nb-C superconductor. *Nat. Commun.* (2020).

[64] Koshelev, A. E. & Vinokur, V. M. Dynamic melting of the vortex lattice. *Phys. Rev. Lett.* **73,** 3580–3583 (1994).

[65] Xiao, Z. L. & Ziemann, P. Vortex dynamics in $YBa_2Cu_3O_{7-\delta}$ superconducting films: Experimental evidence for an instability in the vortex system at high current densities. *Phys. Rev. B* **53,** 15265–15271 (1996).

[66] Kunchur, M. N. Unstable flux flow due to heated electrons in superconducting films. *Phys. Rev. Lett.* **89,** 137005 (2002).

[67] Sivakov, A. G. *et al.* Josephson behavior of phase-slip lines in wide superconducting strips. *Phys. Rev. Lett.* **91,** 267001–1-4 (2003).

[68] Xiao, Z. L. *et al.* Flux-flow instability and its anisotropy in $Bi_2Sr_2CaCu_2O_{8+\delta}$ superconducting films. *Phys. Rev. B* **59,** 1481–1490 (1999).

[69] Goltsman, G. N. *et al.* Picosecond superconducting single-photon optical detector. *Appl. Phys. Lett.* **79,** 705–707 (2001).

[70] Vodolazov, D. Y., Korneeva, Y. P., Semenov, A. V., Korneev, A. A. & Goltsman, G. N. Vortex-assisted mechanism of photon counting in a superconducting nanowire single-photon detector revealed by external magnetic field. *Phys. Rev. B* **92,** 104503 (2015).

[71] Korneeva, Y. P. *et al.* Different single-photon response of wide and narrow superconducting Mo_xSi_{1-x} strips. *Phys. Rev. Appl.* **13,** 024011 (2020).

[72] Gropp, W. D. *et al.* Numerical simulation of vortex dynamics in type-II superconductors. *J. Comput. Phys.* **123,** 254–266 (1996).

[73] Peroz, C. & Villard, C. Flux flow properties of niobium thin films in clean and dirty superconducting limits. *Phys. Rev. B* **72,** 014515–1–6 (2005).

[74] Fournier, P. *et al.* Anomalous saturation of the phase coherence length in underdoped $Pr_{2-x}Ce_xCuO_4$ thin films. *Phys. Rev. B* **62,** 11993 (2000).

[75] Jang, H., Lim, J. & Yang, C. Film-thickness-driven superconductor to insulator transition in cuprate superconductors. *Sci Rep* **10,** 3236 (2020).

[76] Galitski, V. M. & Larkin, A. I. Superconducting fluctuations at low temperature. *Phys. Rev. B* **63,** 174506 (2001).

[77] Glatz, A., Varlamov, A. A. & Vinokur, V. M. Fluctuation spectroscopy of disordered two-dimensional superconductors. *Phys. Rev. B* **84,** 104510 (2011).

[78] Varlamov, A. A., Galda, A. & Glatz, A. Fluctuation spectroscopy: : from Rayleigh-Jeans waves to Abrikosov vortex clusters. *Rev. Mod. Phys.* **90,** 015009 (2018).

[79] Finkel'stein, A. M. Suppression of superconductivity in homogeneously disordered systems. *Physica B* **197,** 636 (1994).

[80] Fuchs, K. The conductivity of thin metallic films according to the electron theory of metals. *Cambridge Philosophical Society,* 100 (1938).

[81] Sondheimer, E. The mean free path of electrons in metals. *Phys. Rev.* **80,** 401 (1950).

[82] Zheng, J. Q., Ketterson, J. B., Falco, C. M. & Schuller, I. K. Superconducting and transport properties of Nb/Ti layered metals. *Physica B* **107,** 945 (1981).

[83] Werner, T. R., Banerjee, I., Yang, Q. S., Falco, C. M. & Schuller, I. K. Localization in a three-dimensional metal. *Phys. Rev. B* **26,** 2224–2226 (1982).

[84] loffe, A. & Regel, A. Non-crystalline, amorphous and liquid electronic semiconductors. *Progress in semiconductors* **4,** 237 (1960).

[85] Bett, R. The effects of neutron irradiation induced atomic disorder on H_{C2} of Nb_3Sn. *Cryogenics* **14,** 7 (1974).

[86] Hahn, P. A., Guinan, M. W., Summers, L. T., Okada, T. & Smathers, D. B. Fusion neutron irradiation effects in commercial Nb_3Sn superconductors. *Journal of nuclear materials,* 179–181 (1991).

[87] Pande, C. S. Mechanism for the degradation of superconducting transition temperatures on highenergy neutron irradiation in A-15 compounds. *Journal of Nuclear materials* (1978).

[88] Karkin, A. E., Arkhipov, V. E., Goshchitskii, B. N., Romanov, E. P. & Sidorov, S. K. Radiation effects in the superconductor Nb_3Sn. *Original Papers phys. stat. sol. (a)* **38,** 433 (1976).

[89] Dubi, Y., Meir, Y. & Avishai, Y. Nature of the superconductor–insulator transition in disordered superconductors. *Nature* **449,** 613 (2007).

[90] Sacepe, B. *et al.* Disorder induced inhomogeneities of the superconducting state close to the superconductor insulator transition. *PRL* **101,** 157006 (2008).

[91] Zaytseva, I., Abaloszew, A., Camargo, B. C., Syryanyy, Y. & Cieplak, M. Z. Upper critical field and superconductor-metal transition in ultrathin niobium films. *Scientific reports* **10,** 19062 (2020).

[92] loffe, L. B. & Larkin, A. I. Properties of superconductors with a smeared transition temperature. *Zh. Eksp. Teor. Fiz.* **81,** 707 (1981).

[93] Skvortsov, M. A. & Feigel'man, M. V. Superconductivity in disordered thin films: Giant mesoscopic fluctuations. *PRL* **95,** 057002 (2005).

[94] Simonin, J. Surface term in the superconductive Ginzburg Landau free energy: application to thin films. *Phys. Rev. B* **33,** 7830–2 (1986).

[95] Kubo, S. Superconducting properties of amorphous MoX (X=Si, Ge) alloy films for Abrikosov vortex memory. *J. Appl. Phys.* **63,** 2033–2045 (1988).

[96] Banerjee, A. *et al.* Characterisation of amorphous molybdenumsilicide (MoSi) superconducting thin filmsand nanowires. *Supercond. Sci. Technol.* **30,** 084010 (2017).

[97] Graybeal, J. M. & Beasley, M. R. Localization andinteraction effects in ultrathin amorphous superconducting films. *Phys. Rev. B* **29,** 4167 (1986).

[98] Ivry, Y. *et al.* Universal scaling of the critical temperature for thin films near the superconducting to insulating transition. *Phys. Rev. B* **90,** 214515 (2014).

[99] Werthamer, N. R., Helfand, K. & Hohenberg, P. C. Temperature and purity dependence of the superconducting critical field. III. Electron spin and spin-orbit effects. *Phys. Rev.* **147,** 295 (1966).

[100] De Gennes, P. G. Behavior of dirty superconductors in high magnetic fields. *Phys. kondens. Materie* **3,** 79–90 (1964).

[101] Maki, K. The magnetic properties of superconducting alloys. *Physics Physique Fizika* **1,** 127–143 (1964).

[102] Lynton, E. A. *Superconductivity* (Methuen and Co. LTD, 1964).

[103] Gorkov, L. P. Theory of superconducting alloys in a strong magnetic eld near the critical temperature. *Soviet physics JETP* **37** (1960).

[104] Clem, J. R. & Kogan, V. G. Kinetic impedance and depairing in thin and narrow superconducting films. *Phys. Rev. B* **86,** 174521 (2012).

[105] Dobrovolskiy, O. V. & Huth, M. Crossover from dirty to clean superconducting limit in dc magnetron-sputtered thin Nb films. *Thin Solid Films* **520,** 5985–5990 (2012).

[106] Krishnan, M. *et al.* Very high residual resistivity ratios of heteroepitaxial superconducting niobium films on MgO substrates. *Supercond. Sci. Technol.* **24,** 115002 (2011).

[107] Maksimova, G. M., Zhelezina, N. V. & Maksimov, I. L. Critical current and negative magnetoresistance of superconducting film with edge barrier. *Europhys. Lett.* **53,** 639–645 (2001).

[108] Zhang, X. *et al.* Characteristics of superconducting tungsten silicide W_xSi_{1-x} for single photon detection. *Phys. Rev. B* (2016).

[109] Sidorova, M. *et al.* Electron energy relaxation in disordered superconducting NbN films. *Phys. Rev. B* **102,** 054501 (2020).

[110] Sidorova, M. *et al.* Magnetoconductance and photoresponse properties of disordered NbTiN films. *Phys. Rev. B* **104,** 184514 (2021).

[111] Budinská, B. *et al.* Rising speed limits for fluxons via edge-quality improvement in wide MoSi thin films. *Phys. Rev. Applied* **17,** 034072 (2022).

[112] A. I. Bezuglyj and V. A. Shklovskij and B. Budinská *et al.* Vortex jets generated by edge defects in current-carrying superconductor thin strips. *Phys. Rev. B* **105,** 214507 (2022).

[113] V. M. Bevz and M. Yu. Mikhailov and B. Budinská *et al.* Vortex counting and velocimetry for slitted superconducting thin strips. *Phys. Rev. Applied* **19,** 034098 (2023).